Università degli Studi di Napoli Federico II
Ph.D. Program in
Information Technology and Electrical Engineering
XXXV Cycle

THESIS FOR THE DEGREE OF DOCTOR OF PHILOSOPHY

Detection and Measurement of inter-area oscillations for power system stability

by

SALVATORE TESSITORE

Advisor: Prof. Leopoldo Angrisani
Company Advisor: Ing. Giorgio Maria Giannuzzi (Terna Rete Italia)
Co-advisor: Prof.ssa Annalisa Liccardo

SCUOLA POLITECNICA E DELLE SCIENZE DI BASE
DIPARTIMENTO DI INGEGNERIA ELETTRICA E DELLE TECNOLOGIE DELL'INFORMAZIONE

Time is relative

its only value is given by what

we do while it is spending

A. Einstein

Detection and Measurement of inter-area oscillations for power system stability

Ph.D. Thesis presented
for the fulfillment of the Degree of Doctor of
Philosophy in Information Technology and Electrical
Engineering by

Salvatore Tessitore

October 2022

Approved as to style and content by

Advisor: Prof. Leopoldo Angrisani

Company Advisor: Ing. Giorgio Maria Giannuzzi (Terna Rete Italia)

Co-advisor: Prof.ssa Annalisa Liccardo

Università degli Studi di Napoli Federico II
Ph.D. Program in Information Technology and Electrical Engineering
XXXV cycle - Chairman: Prof. Stefano Russo

http://itee.dieti.unina.it

Candidate's declaration

I hereby declare that this thesis submitted to obtain the academic degree of Philosophiæ Doctor (Ph.D.) in Information Technology and Electrical Engineering is my own unaided work, that I have not used other than the sources indicated, and that all direct and indirect sources are acknowledged as references.
Parts of this dissertation have been published in international journals and/or conference articles (see list of the author's publications at the end of the thesis).

Napoli, October 15, 2022

____

Salvatore Tessitore

Contents

Abstract

Interconnected electrical system stability is the ability of the system to find a new equilibrium condition following a disturbance. The phenomena of stability of the electrical system can be classified into three categories: rotor angle stability, frequency stability and voltage stability. In this doctoral research activity, the focus is on low-frequency oscillations (LFO), which are phenomena related to the stability of the rotor angle. This is a crucial aspect to be carefully monitored in the Italian and European electricity system, to ensure its safety and reliability.

Undamped frequency oscillations can compromise the system integrity on a large scale: in the past, several accidents have been recorded caused by the establishment of high-intensity oscillations around the world.

Thanks to new technologies, in recent years measurement and instrumentation structures based on Wide Area Measurement Systems (WAMS) technology have become widespread, which is essential to monitor and characterize this type of phenomenology. The possibility of synchronous and other frequency sampling, the possibility of a communication protocol capable of transmitting high sampling data with low latencies guarantees a large amount of data from the phasor units of measurement (PMUs) installed throughout the European electricity system, increasing its observability by transmission system operators (TSOs).

A description of the WAMS currently used by the Italian TSO (Terna) confirms that the detection of frequency oscillations is one of the main functionalities/applications planned by these architectures. The real-time detection of dangerous frequency oscillations and then the estimation of the relative parameters (frequency, damping, amplitude and phase) is fundamental in the framework described above. When potential divergent oscillations are detected, all necessary countermeasures must be implemented to restore safe and stable operating conditions (e.g., re-dispatching of generators, regulation of connecting line flows, load reduction, modification of network topology, etc.). For this purpose, the major problems concern the complexity in the search for robust identification techniques and accurate

characterizations of frequency oscillations. In this regard, several fundamental approaches for tracking electromechanical modes in an electrical system are reported in the literature. Some approaches use a linearized electrical system model around a certain equilibrium point to identify the characteristics of electromechanical modes through eigenvalue analysis. Others are based on the estimated measurements of an updated model of the electricity system from direct measurements of the system, coming from measuring devices installed on the electricity grids.

From the experience gained working for a long time on the subject, I can now say that there is no optimal algorithm applicable in all operating conditions but rather each one has advantages. This means that, for example, one method might show good performance in phase and frequency estimation, another might show very good performance in estimating damping and amplitude. In addition, one method might work better than another for signals sampled without noise, while it could worsen its efficiency when the signal-to-noise ratio (SNR) decreases. However, there are estimation techniques that are generally characterized by good performance compared to others. In the present thesis, first different estimation techniques have been analyzed both on simulated data and on real data. Subsequently, improvement solutions have been proposed compared to that reported in the literature and finally in relation to the monitoring or defense objective set with the Italian TSO, the most appropriate method for real-time application has been chosen.

The goal of this research was therefore to create highly accurate and resilient estimation algorithms for real-time monitoring and defense of electromechanical oscillations, particularly inter-area, in such a large interconnected system. Although the PhD course ends by achieving the established goals, my research is still ongoing as an employee of the Italian TSO (Terna).

Keywords: WAMS, Inter-area oscillations, Transmission grid stability, low-frequency oscillations (LFO), online damping estimation.

Sintesi in lingua italiana

La stabilità del sistema elettrico interconnesso è la capacità del sistema di trovare una nuova condizione di equilibrio in seguito a un disturbo. I fenomeni di stabilità del sistema elettrico possono essere classificati in tre categorie: stabilità dell'angolo di rotore, stabilità della frequenza e stabilità della tensione. In questo dottorato di ricerca, l'attenzione si concentra sulle oscillazioni a bassa frequenza (LFO), fenomeni legati alla stabilità dell'angolo del rotore. Si tratta di un aspetto cruciale da monitorare attentamente nel sistema elettrico italiano ed europeo, per garantirne la sicurezza e l'affidabilità.

Le oscillazioni di frequenza non smorzate possono compromettere l'integrità del sistema su larga scala: in passato sono stati registrati diversi incidenti in tutto il mondo causati dall'instaurarsi di oscillazioni di elevata intensità.

Grazie alle nuove tecnologie, negli ultimi anni si sono diffuse strutture di misura e strumentazione basate sulla tecnologia Wide Area Measurement Systems (WAMS), essenziale per monitorare e caratterizzare questo tipo di fenomenologia. La possibilità di campionamento sincrono e ad altra frequenza, la possibilità di un protocollo di comunicazione in grado di trasmettere dati ad alto campionamento con basse latenze garantisce una grande quantità di dati dalle Phasor Measurement Unit (PMU) installate in tutto il sistema elettrico europeo, aumentandone l'osservabilità da parte degli operatori del sistema di trasmissione (TSO).

Una descrizione dei WAMS attualmente utilizzati dal TSO italiano (Terna) conferma che il rilevamento delle oscillazioni di frequenza è una delle principali funzionalità/applicazioni previste da queste architetture. Il rilevamento in tempo reale di oscillazioni di frequenza pericolose e la successiva stima dei relativi parametri (frequenza, smorzamento, ampiezza e fase) è fondamentale nel quadro descritto sopra. Quando vengono rilevate potenziali oscillazioni divergenti, devono essere attuate tutte le contromisure necessarie per ripristinare condizioni operative sicure e stabili (ad esempio, ridispacciamento dei generatori, regolazione dei flussi delle linee di collegamento, riduzione del carico, modifica della topologia della rete, ecc. A questo proposito, in letteratura sono riportati diversi approcci fondamentali per il tracciamento dei modi elettromeccanici in un sistema elettrico. Alcuni approcci utilizzano un modello di sistema elettrico linearizzato attorno a un certo punto di equilibrio per identificare le caratteristiche dei modi elettromeccanici attraverso l'analisi degli autovalori. Altri si basano sulle misure stimate di un modello aggiornato del sistema elettrico a partire da misure dirette del sistema, provenienti da dispositivi di misura installati sulle reti elettriche.

Dall'esperienza acquisita lavorando a lungo sull'argomento, posso affermare che non esiste un algoritmo ottimale applicabile in tutte le condizioni operative, ma piuttosto ognuno di essi presenta dei vantaggi. Ciò significa che, ad esempio, un metodo potrebbe mostrare buone prestazioni nella stima della fase e della frequenza, mentre un altro potrebbe mostrare ottime prestazioni nella stima dello smorzamento e dell'ampiezza. Inoltre, un metodo potrebbe funzionare meglio di un altro per segnali campionati senza rumore, mentre potrebbe peggiorare la sua efficienza quando il rapporto segnale/rumore (SNR) diminuisce. Tuttavia, esistono tecniche di stima che sono generalmente caratterizzate da buone prestazioni rispetto ad altre. Nel presente lavoro, sono state innanzitutto analizzate diverse tecniche di stima sia su dati simulati che su dati reali. Successivamente, sono state proposte soluzioni migliorative rispetto a quelle riportate in letteratura e infine, in relazione all'obiettivo di monitoraggio o difesa fissato con il TSO italiano, è stato scelto il metodo più appropriato per l'applicazione in tempo reale.

L'obiettivo di questa ricerca consisteva nel creare algoritmi di stima altamente accurati e resilienti per il monitoraggio e la difesa in tempo reale delle oscillazioni elettromeccaniche, in particolare inter-area, in un sistema interconnesso di così grandi dimensioni. Sebbene il corso di dottorato si concluda con il raggiungimento degli obiettivi stabiliti, la mia ricerca è ancora in corso come dipendente del TSO italiano (Terna).

Parole chiave: WAMS, Oscillazioni inter-area, Stabilità della rete di trasmissione, Oscillazioni a basse frequenze, stima online dello smorzamento.

List of Figures

List of Tables

Chapter 1

1 Interconnected System and Inter-Area Oscillations

1.1 Electricity Grid and Interconnection

The term 'network' means in the Italian language, an interweaving of threads of various material, crossed with each other regularly. In the same way, what we know today as the electricity grid is a system with a complex, strongly interconnected configuration that cannot be traced to a simplified 'isolated' scheme with a single point of connection, between producer and end customer. In a document drawn up by ARERA (Regulatory Authority for Energy, Networks and Environment) in 2019, the electricity grid is distinguished from the Simple Production and Consumption Systems (SSPC) which, on the other hand, are attributable to configurations characterized by a single producer and a single end customer, electrical configurations with a one-to-one ratio [1].

Divided into its subsystems, generation, transmission, distribution and use, the national electricity system (SEN) is therefore necessarily interconnected and supportive. Cooperation between the various parts of the network is an essential prerogative for its operation, to increase its reliability, to compensate for the production deficits of specific areas, but also and above all because what happens in one point of the network influences the correct functioning at another point of the same. Just consider that frequency and voltage adjustments are managed with wide-ranging plans, which provide for the participation of several generation groups, a control center, a monitoring at national level.

1.2 National and European Development Plans

To these concepts, which are already sufficient to lean towards an increasingly interconnected and cooperative electricity grid, is now added the need to move towards an energy transition and towards the

achievement of European targets regarding climate and environment through the integration of renewable energies. In this regard, the association of European Network of Transmission System Operators for Electricity (ENTSO-E), which represents 42 electricity transmission system operators (TSOs) from 35 countries across Europe, updates every two years non-binding ten-year grid development plans that provide guiding principles for the coordination of research and development activities. The ENTSO-E, in collaboration with other European institutions and organizations, aims to develop an efficient electricity system and energy market, capable of combining sustainability and innovation, ensuring a safe and reliable supply to users. In the "Publications" section of the official website of ENTSO-E it is possible to consult the documents and have more information on the aforementioned ten-year development plan, indicated by the acronym TYNDP [2].
The TYNDP is the result of a process involving hundreds of experts, who starting from scenarios of what the European energy system could look like in 2030 and 2040, have evaluated the electricity grid strengthening projects presented through European calls. As for Italy, the TSO is represented by TERNA, and is involved in 18 TYNDP projects, some ongoing, others planned but awaiting permits. For example, the national HVDC connection Peninsula – Sicily – Sardinia [3] (Figure 1.1), or the international connection Tunisia-Italy (Figure 1.2) in addition to the strengthening of those with Austria. Without going into the details of the projects, this general vision of the development plans highlights the importance of electricity interconnection, both at national level to cover the demands of regional users, sometimes not self-sufficient, and at European and non-European level to achieve the so-called *"electricity interconnection objective"*. Already in 2014, the European Council called on all Member States to increase the interconnection by at least 10% of their production capacity by 2020 [4].

Figure 1.1 Representation Simulink network test

Figure 1.2 Tunisia–Italy connection [5]

From a strictly national point of view, on Terna's website it is possible to find some information on the 2021 Development Plan with which the company's objectives and lines of action have been outlined on the basis of European guidelines (Figure 1.3).

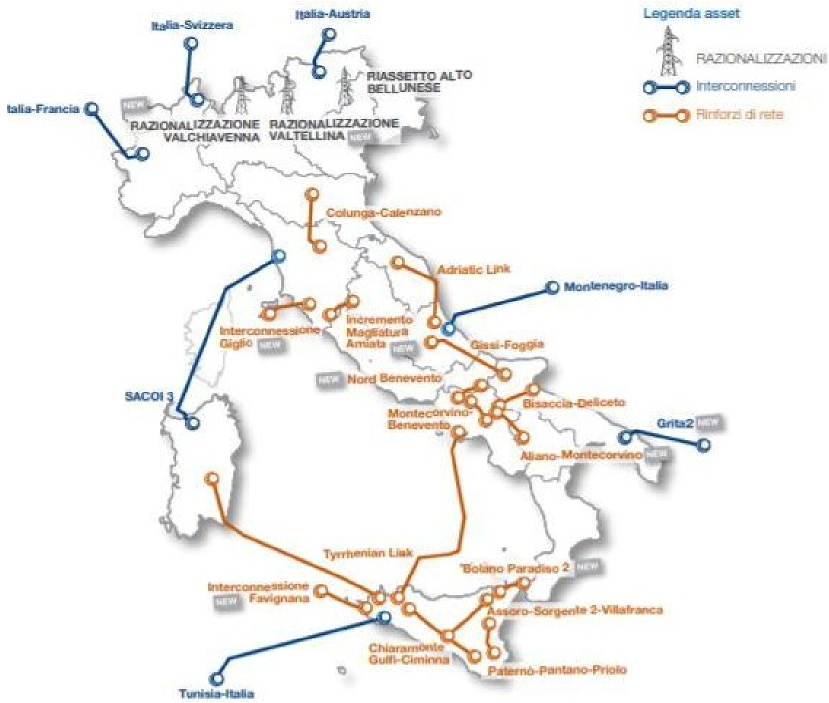

Figure 1.3 2021 Development Plan [6]

"The national electricity system is in fact transforming from a centralized model to an integrated and distributed one: until 2000 we dispatched energy from just over 800 power plants; now we have 800000 active generation plants in Italy that will become one million in the near future". These are the words found on Terna's website in relation to the topic. The same article highlights how fundamental, to manage this transformation, the new digital technologies that allow to collect and transfer large flows of data, in order to analyze them effectively and promptly. [7]

1.3 Frequency Oscillations

Despite the increase in production from photovoltaic and wind power plants in recent years, the national energy needs are still covered for the majority by thermoelectric and hydroelectric power plants that exploit the turbine-alternator group to produce electricity. A synchronous generator or alternator is an electrical machine that transforms a primary mechanical source into electrical energy. The adjective synchronous immediately clarifies that this machine works only at its point of synchronism or when the pulsation of the rotating electromagnetic fields of the stator and the rotor and the speed of the rotor itself, coincide. The mechanical angular velocity, i.e. the number of rotations per minute of the rotating masses of the machine, is related to the frequency of the alternative forms of voltage and current fed into the electricity grid, according to the equation:

$$f = \frac{N_s \cdot p}{60} \quad (1.1)$$

- N_s [rpm] is the number of rotations per minute;
- f [Hz] is the electrical frequency;
- p is the number of polar pairs.

Theoretically, any frequency can be a point of operation of the alternator, as long as the synchronism condition occurs. To this technical requirement is added another regulatory one as the nominal frequency is fixed and standardized throughout Europe at the value of 50 Hz. Synchronous generators must therefore keep their speeds constant and be synchronized with each other whatever the load they supply. It is therefore necessary to regulate them appropriately through regulation and control systems throughout the electricity grid, so as to avoid instability in operation [8]. Adjusting the frequency and therefore the speed, is translated into an active power regulation through the D'Alembert equation:

$$M_e - M_r = J \frac{d\omega_r}{dt} \quad (1.2)$$

- M_e [Nm] is the electromagnetic torque;
- M_r [Nm] is the durable torque;

- J [kgm²] is the moment of inertia;
- $\frac{d\omega_r}{dt}$ is the angular acceleration.

Being the driving torque is closely linked to the electrical power ($P_e = M_e \cdot \omega_r$ $[W]$) we obtain:

$$P_e - P_r = J\,\omega_r \frac{d\omega_r}{dt} \qquad (1.3)$$

To maintain the equilibrium condition, it is necessary to guarantee a condition of parity between output power and absorbed power ($\Delta P = 0$). Due to sudden changes in the load, the detachment of an interconnection line or as a result of a short circuit, this condition is continuously disturbed, resulting in an angular acceleration.
When this happens, the rotating magnetic field generated by rotor excitation, whose rotational speed is synchronous with that of the rotor, begins to rotate at a different speed than the stator rotating magnetic field. The interaction between the two fields gives rise to an alternative electromagnetic torque that causes accelerations and decelerations of the rotor, and therefore a pendulum oscillation of the same. When the amplitude of such oscillations brings the machine into conditions of instability, the generator loses its pitch, that is, rotor and stator magnetic field permanently lose synchronism and the generator will have to be stopped and then restarted. The blackout of a generator induces oscillations of the electrical parameters in the electrical system, the amplitude of which will be maximum near the generator involved and will propagate along the entire transmission network with reduced amplitude, also affecting groups belonging to interconnected areas.
Avoiding the loss of the pitch is possible by monitoring the network and intervening in a short time whenever an abnormal condition arises, compensating for the imbalance between the output powers and absorbed powers through the participation of the other generation groups present in the network, which provide a sort of reserve to make up for the deficit. The whole thing is regulated by the TSO itself and is part of a large area of study that goes by the name of frequency and active power regulation.

1.4 Classification of the Oscillations

Going into detail, the oscillations of the electrical system manifest themselves as oscillations of the network parameters (voltage, current, active and reactive power), which overlap the nominal frequency of 50 Hz with variable amplitudes and damping.
Mathematically, an electrical quantity is presented as a superposition of modes, one fundamental at the frequency of 50 Hz and the others at various frequencies. Each i-th mode of evolution is represented

through the following expression [9]:

$$y_i\ (t) = A_i \cdot e^{-\sigma_i \cdot t} \cdot \sin(2\pi f_i \cdot t + \varphi_i) \qquad (1.4)$$

- $y_i\ (t)$ is the i-th oscillation;
- A_i is the amplitude of oscillation;
- f_i is the frequency of oscillation;
- σ_i is the damping coefficient;
- φ_i is the initial phase of oscillation.

From a technical point of view, the oscillations are tolerable if they decay over time, and tend to become smaller and smaller as they dampen, while they are dangerous if they have high amplitudes and are increasing over time. In the presence of divergent modes, in fact, a synchronous generator could be brought into conditions of instability with consequent loss of pitch. The divergence or convergence of a mode of evolution is characterized by the damping or the damping coefficient (σ_i). With positive values of damping the oscillation is convergent, that is, it tends to dampen and extinguish, while with negative values of damping, the oscillations are not attenuated over time but amplified and can reach dangerous amplitudes that trigger the intervention of protections.
According to the value of damping, the modes of evolution are classified into:

- damped → $\sigma_i \in (0.05, +\infty)\ [s^{-1}]$
- weakly damped → $\sigma_i \in (0, 0.05)\ [s^{-1}]$
- divergent → $\sigma_i \in (-\infty, -0.05)\ [s^{-1}]$

The oscillations, according to the frequency range, are divided into:

- local oscillations;
- inter-area oscillations;
- intra-implant oscillations;
- control oscillations;
- torsional oscillations.

Local oscillations are electromechanical oscillations that occur between groups of synchronous generators installed in a given area (same power plant), compared to the rest of the power system. They are characterized by a frequency range of 0.8 – 2.0 Hz.
Inter-area oscillations, on the other hand, include lower-frequency oscillations that propagate over long distances along the transmission grid. They are the cause of the interconnection of the various generation groups and that is why they are defined with the name of inter-area, because they depend on the interfacing of different areas. They usually occur when two parts of an electrical system with significant generation groups are connected by a weak connecting line.

The typical frequency range is 0.1 – 0.8 Hz.

Intra-plant oscillations, on the other hand, occur precisely in the same plant due to the oscillations of the installed machines compared to the rest of the system. They have a frequency range typically between 2.0 and 3.0 Hz, to be evaluated, however, depending on the installed power.

Control oscillations are so called because they result from errors in control systems, from a wrong tuning during electricity grid monitoring. They are located in the frequency range from 3.0 to 10 Hz.

Torsional oscillations are associated with the shaft systems of turbine generators and fall into a typical frequency range of 10 – 46 Hz.

The phenomenon taken into account in this Ph.D. research program is the inter-area oscillations.

1.4.1 Inter-Area Oscillations

As defined above, inter-area oscillations [10] are a consequence of the interconnection of large areas of electrical systems. For this reason, their analysis is the subject of study at European level and requires collaboration and cooperation between the various TSOs that must provide the associative body (ENTSO-E) with the measures detected [11]. When special events occur, such as blackouts or openings of connecting lines, or losses of generation groups, oscillations of the relevant electrical parameters propagate in the electricity grid. Each control center is called upon to identify and report such anomalies. These values are used first to start load shedding procedures and other adjustment maneuvers, and then they are collected by the ENTSO-E which uses them to publish reports on the events that have occurred. The available documentation obviously contributes to the research and allows to understand practically what happens. Here are two examples:

In 2016, following the opening of a French line, fluctuations were detected in other European countries. In the relative document it is reported as follows: "the system shows two main modes of oscillation: a North - South mode with a frequency of about 0.28 Hz and an East - West mode with a frequency of 0.15 Hz. Before the connection of Turkey, the East - West mode was in the range of 0.2 – 0.3 Hz due to the small size of the system" [12].

In a report of December 3, 2017, instead, it can be read: "an interzonal oscillation has been detected in the European continental system. The frequency of the oscillatory mode under examination was identified at 0.29 Hz with significant contributions from power plants in Southern Italy. The oscillation observed in Southern Italy is in phase with the oscillation observed in the countries of the South-Eastern European Community and in part of the south of France and Switzerland, but it is in the opposite phase to the oscillation recorded in Northern Europe (Germany, Denmark and France)" [13].

It has already been said that the interesting frequency range of inter-area oscillations is 0.1 – 0.8 Hz, but within this range it is possible to make a further distinction. Among the inter-area oscillations, the most characteristic modes (Figure 1.4) are divided as follows:

East-West mode: appeared following the connection with Turkey, which took place in 2010, concerns the movement of generators in Portugal and Spain compared to those in Turkey. It has a typical frequency of 0.13 – 0.15 Hz;

East-Center-West mode: it concerns the movement of generation groups in Portugal and Spain compared to those of Greece. The typical frequency falls in the range of 0.17 – 0.2 Hz;

North-South mode: it provides for the relative movement between the generators located in southern Italy compared to those installed in the North of Germany and Denmark. The typical frequency falls in the range of 0.23 – 0.3 Hz

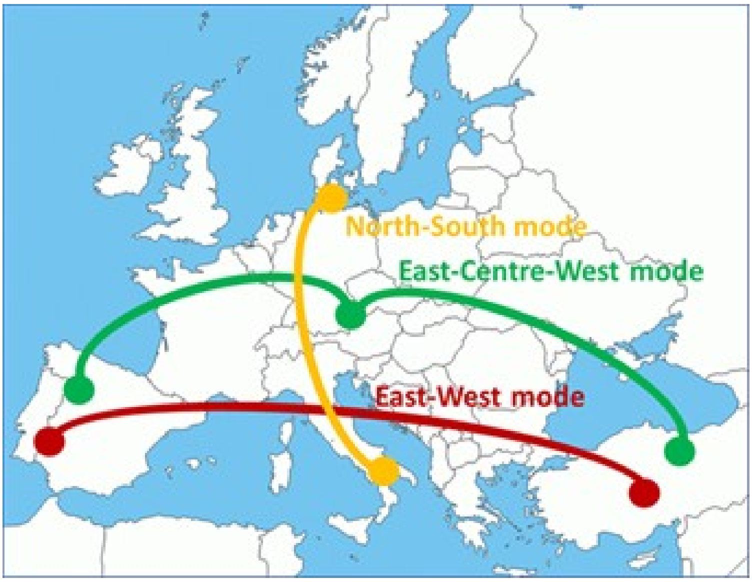

Figure 1.4 Inter-area modes

Chapter 2

2 Wide Area Measurement System

2.1 Overview

Nowadays, maintaining high network security is one of the fundamental requirements for the TSO. Therefore, the acquisition of an increasing amount of information on the system is essential to predict the dynamic evolution of power systems, in all operating conditions, and to identify the most appropriate and effective countermeasures that guarantee safe and stable operating conditions. The main obstacles in this regard are represented by the inability of the TSO to predict with high precision the behavior of the system, but also by the technological limitations of traditional supervision, control and data acquisition systems. In recent decades a number of factors have led to the reduction of the safety margins in which the transmission network operates, among them are:

- the continuous development of interconnections that increase the complexity of electricity grid dynamics;
- the increasingly high energy demand from users, therefore an increase in the load for the electricity grid, which leads to an increase in power transits without the electricity grid being adequately enhanced;
- the increase in power flows associated with renewable sources, which are not controllable as the availability of these sources is random and non-programmable.

A pragmatic solution to the highlighted problems is represented by the development of WAMS (Wide Area Measurement System) which represents one of the latest technologies for upgrading the traditional electricity grid [14]. This improvement has become a necessity after the occurrence of major blackouts in power systems around the world, among all we remember the one that happened on September 28, 2003 in Italy, in which a series of events led to the separation of Italy from the interconnected European electricity system. In fact, in the final report of the UCTE investigative commission, which investigated this

blackout, the development of WAMS for the monitoring and real-time study of the dynamics of the electricity grid as a useful technology for the prevention of heavy events was strongly recommended.
WAMS is a system of real-time monitoring of a large area based on the measurement of synchrophasors through sophisticated devices called PMUs (Phasor Measurement Unit) [15]. It is a functional system mainly for three purposes:

- obtain data from different strategic points of the national transmission grid;
- evaluate the parameters of interest for the analysis, both dynamic and static, offline and online;
- possibility to compare data from different areas of the network on the basis of a common time reference, as the acquisitions are synchronized by means of the GPS.

As it can be seen from Figure 2.1, the WAMS consists mainly of two elements:

- PMU, Phasor Measurement Unit;
- PDC, Phasor Data Concentrator.

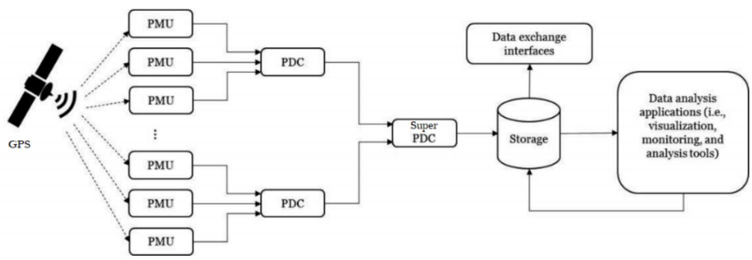

Figure 2.1 Architecture of a Wide Area Measurement System

A PMU is a device that performs measurements of synchrophasors from the voltage and current waveforms sampled at defined sampling instants. The measurements made by the PMU are normally timestamped and synchronized on the basis of a common time, provided by a highly reliable time source, among all the GPS system.
A PDC is a device that plays the role of collector for data coming from groups of PMUs. Its main function is to synchronize all the different data flows coming from the PMUs by creating a single stream of synchronized data to be sent to the central server.
Thus, in a transmission network to be monitored, there are numerous PMUs, positioned at strategic points, properly chosen after an in-depth study, which carry out the measurements. If the number of PMUs is high, there is a division into groups, based on geographical location. Each group is headed by a local PDC. The various local PDCs, in turn, send the respective synchronized data stream to a "global" PDC, usually called "Super PDC" which realizes a single data stream that

will be stored and used for the appropriate monitoring and protection of the transmission network.
The development of WAMS technology combined with PMU devices allows network operators to monitor the dynamics of the electrical system in real time with a degree of precision and detail that was not possible with conventional SCADA (Supervisory Control And Data Acquisition) systems [16]. This allows a deeper and simpler understanding of the conditions of the system, and considerable support in deciding the execution of control actions and maneuvers. In fact, since PMUs are characterized by a high data acquisition speed, the dynamics of the system can be accurately captured when it is subjected to disturbances. Figure 2.2 shows the phase shift between voltages of two substations acquired with a PMU compared with that acquired using a classic EMS (Energy Management System) network for state estimation. This comparison clearly demonstrates that a real-time monitoring system consisting of PMUs provides much more accurate and dynamic trends and information than traditional state estimate, allowing the electricity grid operator to apply countermeasures in a more timely and correct manner downstream of disturbances that may compromise the stability of the national power system.

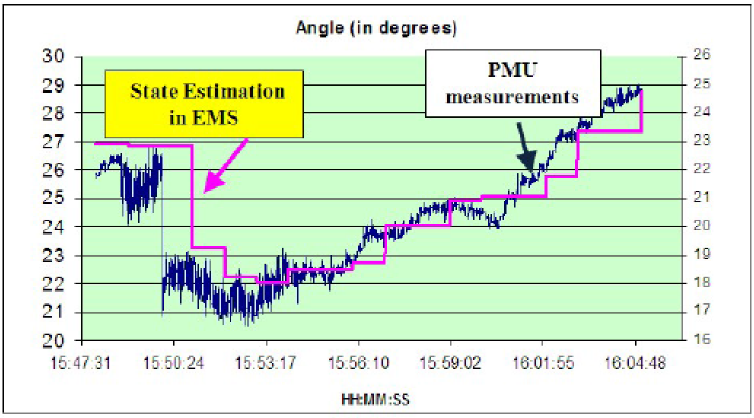

Figure 2.2 Comparison between PMUs and a classic status estimation system (EMS)

2.2 Applications

The main applications of WAMS are aimed at monitoring, while talking about WAMPAC system (Wide Area Monitoring Protection and Control) when protection and control of the electricity grid are carried out in addition to monitoring [17].
Applications are generally divided into two categories:

- offline applications, used to improve and validate the mathematical model of the electrical system, to make studies on offline electricity grid stability and to plan actions for increasing the reliability.

- online applications, i.e. support activities for the network operator for monitoring, managing and protecting the electricity grid itself in real time.

Figure 2.3 shows the main applications divided into the two categories listed above.

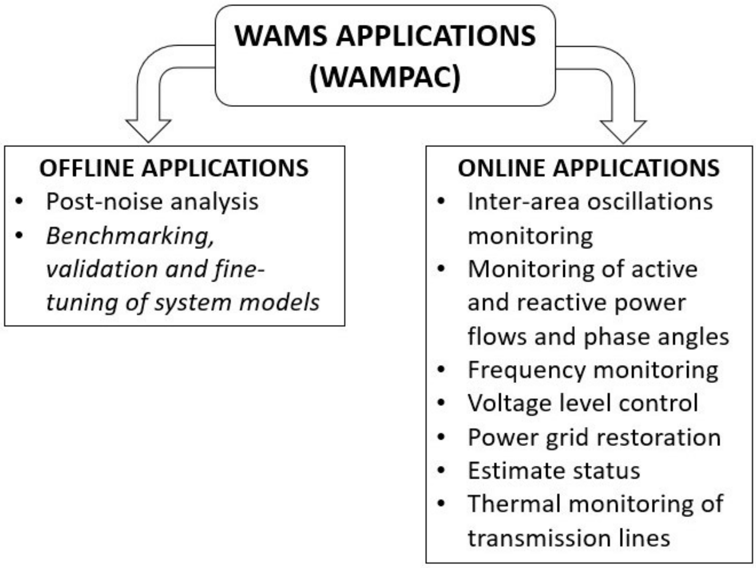

Figure 2.3 WAMS applications

2.2.1 Offline Applications

Post-noise analysis

The main objective of post-disturbance analysis is to study the dynamics of the system during large disturbances and analyze the sequential events of the system caused by such disturbances. Thanks to the use of PMUs, the data collected are synchronized on the time reference signal provided by the GPS, therefore the procedure for reconstructing the sequence of events following the disturbance has been facilitated.

Benchmarking, validation and fine-tuning of system models

The main tasks of benchmarking and validation activities are the testing and identification of potential errors present in the mathematical model of the power system and in the analytical procedures implemented on it. Accurate and reliable system models are essential for the operation of the system itself, its proper management planning and for efficient and robust control. Inaccurate system models can cause the transmission system operator to make decisions that are too conservative or incorrect.

2.2.2 Online Applications

Inter-area oscillation monitoring

With WAMS technology it is possible to monitor the dynamic behavior of the system and identify the modes of inter-area oscillation and if alarming conditions occur it will be necessary to intervene suddenly to avoid the loss of stability of the transmission network. Figure 2.4 illustrates an inter-area oscillation identified by the PMU.

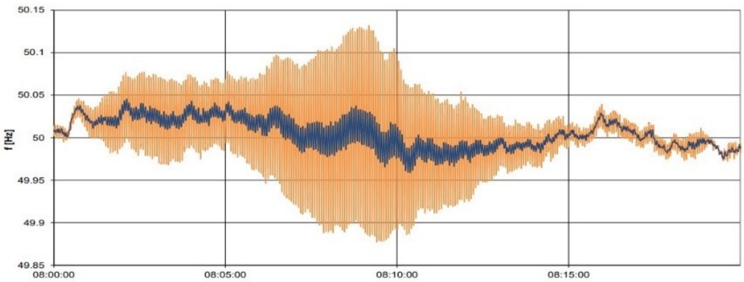

Figure 2.4 Inter-area oscillation identified with PMU

Monitoring of active and reactive power flows and phase angles

PMUs make it possible to detect the phase shift between the nodes of the electricity grid through the power flows that affect the transmission lines. This is advantageous for the network operator when it comes to monitoring in real time the stress, from the point of view of power transits, to which the network is subjected. This real-time monitoring results in a greater degree of confidence in the management of critical power transmission corridors.

Frequency monitoring

The frequency of the power system is one of the most valuable information for real-time assessment of grid stability since the variation over time in the frequency of the system is the direct measure of the balance between power generation and demand. During large disturbances the frequency is rapidly variable and very different in several areas of the transmission system. The high data reporting rate offered by PMUs provided a great opportunity for the system operator to obtain accurate measurements of the frequency of the dynamic system. If the entire power grid is monitored by a synchronized measurement of frequency and its evolution over time, the overall dynamic behavior of the network can be considered accurately detected.

Voltage level control

Through the estimation of the synchrophasors offered by the PMUs it is possible to keep under observation the amplitudes of the voltages in the main nodes of the transmission network, in particular, in those of generation. This application falls within the scope of grid voltage regulation.

Power grid restoration

Given the complex nature of the transmission system, it must be accepted that in some cases blackout is inevitable, then it becomes necessary to undertake strategies to minimize the duration of these interruptions. When a portion of the network is restored, there may be negative repercussions on other portions of the electricity grid not affected by the outage. The PMUs, used during the re-ignition, allow to detect in real time information on the phase angles in the portions of the electricity grid interconnected with the portion that needs to be restored, this gives the grid operator the ability to assess whether or not the restoration of this portion can compromise the stability of the electricity grid.

Figure 2.5, taken from a report by the UCTE Committee of 4 November 2006, shows the measurements of PMUs recorded during attempts to reclose interconnection power lines between two European areas, followed by the reclosing of interconnection lines between these two areas and a third European area.

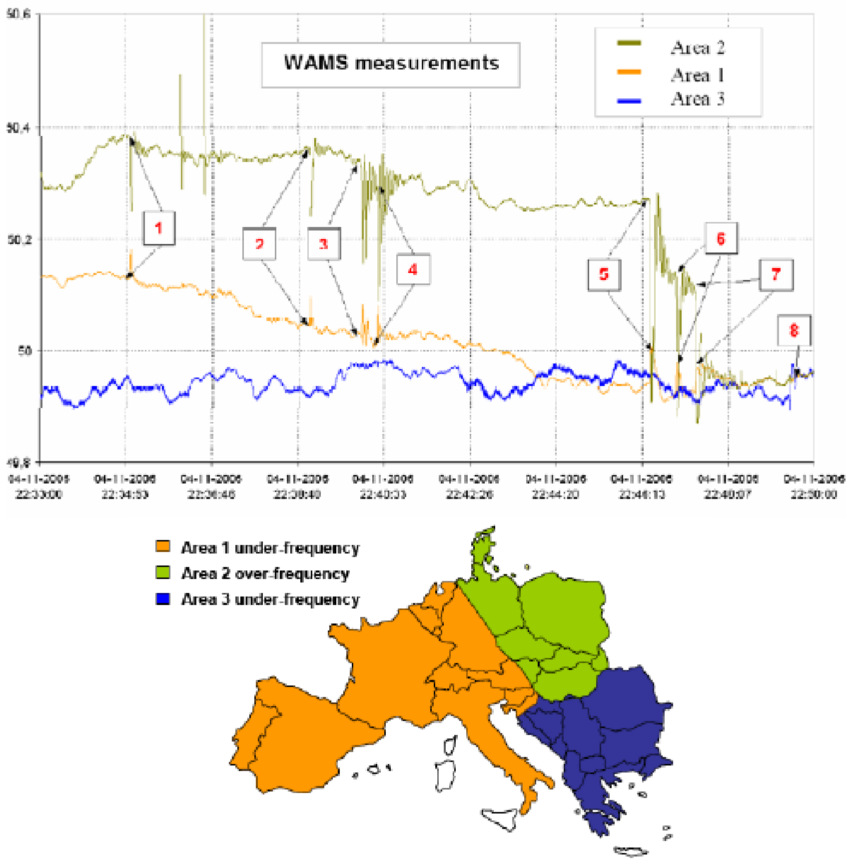

Figure 2.5 PMU measurements belonging to three areas during reclosing attempts

Status Estimation

Estimating the status of the power electrical system is one of the most important online applications, necessary for the energy management system and for operational safety assessments. State estimation means knowledge of the modules and voltage angles in all nodes of the network. Synchronized measurements and synchrophasors allow a better quality in the estimation of the state. As the number of PMUs increases, the observability of the network increases until it reaches a number of PMUs such as to consider the network completely observable, in this way it is possible to use a linear estimation method, thus reducing the computational load obtaining greater precision in the solution compared to classic nonlinear methods. Thanks to the PMUs it is possible to create a real-time parameter identification network (real-time estimation of line impedances and transverse admissions).

Thermal monitoring of transmission lines

It is well known that the power transport capacity of an overhead transmission line is limited by the temperature of the conductors. With PMUs installed on both terminals of an overhead line, with synchronized phasor estimates it is possible to calculate the actual line impedance and derive the value of the line resistance. Known the characteristics of the conductor, it is possible to estimate in real time the temperature of the conductor of the overhead line.

2.3 WAMS in Terna

The Transmission System Operator in Italy is *Terna*, which, as TSO, has the task of ensuring the correct operation of the transmission grid with appropriate control and monitoring activities synchronized in real time, and is responsible for the dispatching of electricity in Italy. Terna's national transmission grid consists of 66000 km of lines and about 870 power stations; it is characterized by five voltage levels 400 kV, 230 kV, 150 kV, 132 kV and 60 kV. Figure 2.6 shows the distribution of the 400 kV lines along the Italian peninsula and the three HVDC (High Voltage Direct Current) connections: Sardinia – Italian Peninsula, Greece – Italy and Montenegro – Italy.

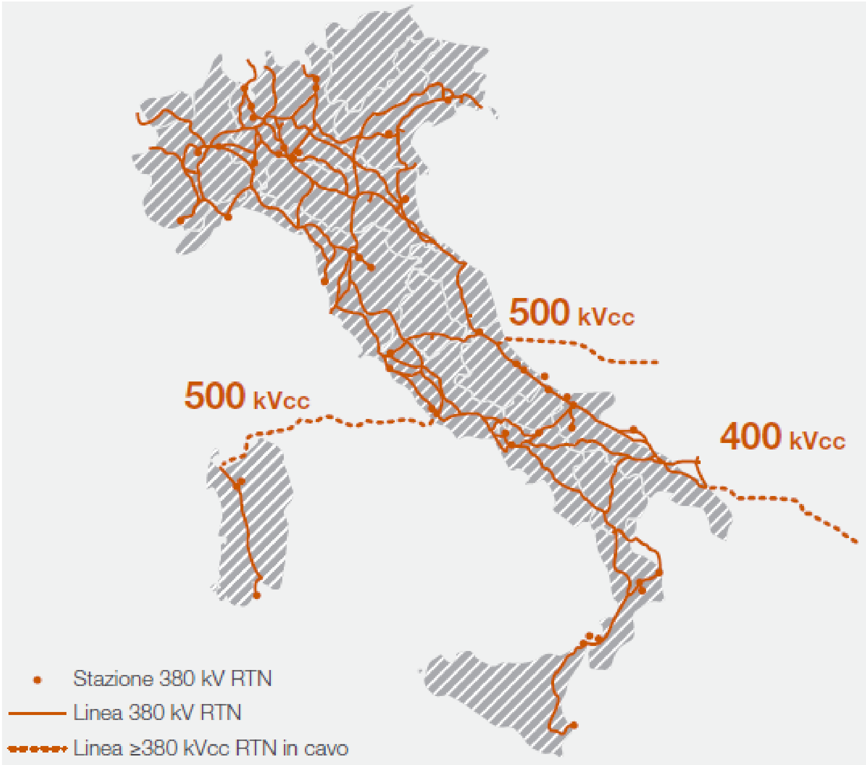

Figure 2.6 Italian 380 kV transmission grid and HVDC connections

Given the particular geographical configuration of the country, the Italian Electricity System has some peculiarities: almost all the interconnection capacity with foreign countries insists on the northern border, while the elongated shape of the peninsula determines the presence of "bottlenecks" between the different areas of the country, which cause difficulties in optimizing energy flows, especially between Northern and Southern Italy and towards the islands.
The WAMS system developed by Terna consists of a set of PMUs, a dedicated data network and computer systems for data processing and management, including monitoring and intelligent visualization applications [18].
Currently about 220 PMUs are installed at the main stations of the Italian transmission network, in projection it will reach about 330 PMU installed. For the selection of PMU locations, combined heuristic-analytical criteria have been adopted. Each criterion covers local or system aspects, such as proximity to large production units, bottlenecks, system boundaries, etc. Figure 2.7 shows a georeferenced representation of PMUs on the national territory.

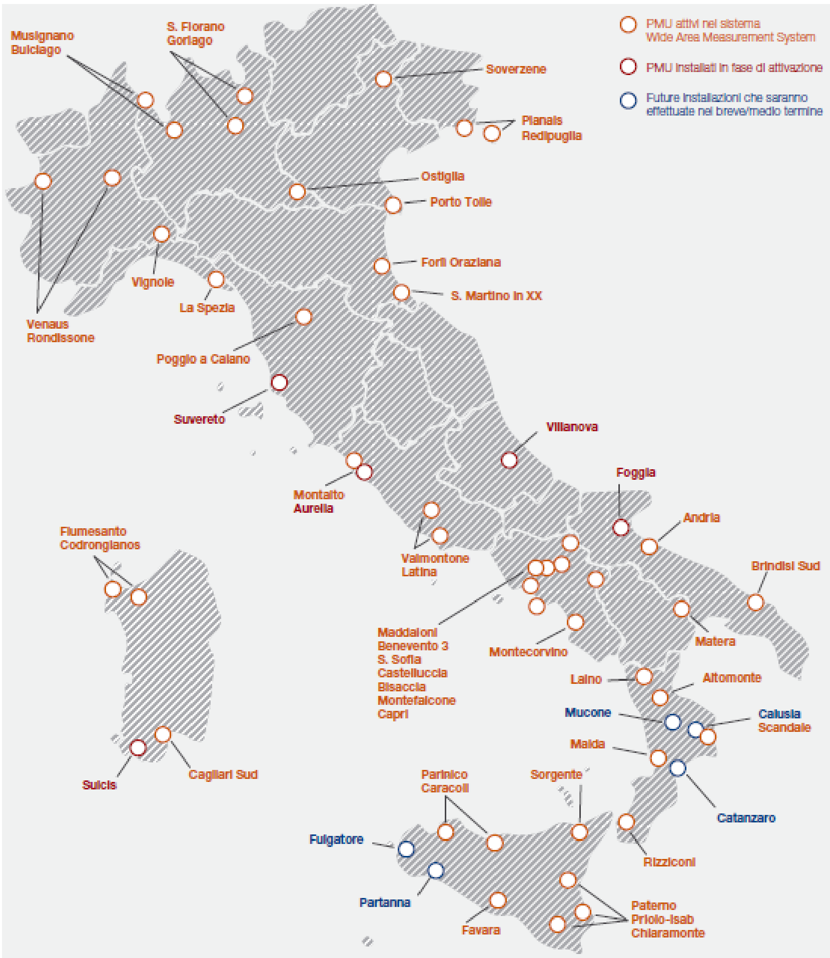

Figure 2.7 Georeferenced representation of PMUs on the Italian territory

The PMUs of Terna's monitoring system, currently among the largest in the world, work with a speed of 50 fps, that is, a block of measurements of electrical quantities (voltage amplitude and phase, frequency, etc.) is sent every 20 ms. Terna also acquires measurements in real time from PMUs installed in neighbor countries that are covered by the ENTSO-E, i.e. the European network of transmission system operators. It is essential that the network operator has tools capable of processing in real time the enormous amount of data available, to evaluate the stability of the network and to promptly implement corrective actions in case of criticality. For the monitoring of the SEN in support of the National Control Centre, Terna uses an integrated tool called WEBWAMS.

Figure 2.8 represents the graphical interface of WEBWAMS, where three main sections can be appreciated:

- Geographical representation: this section shows a geographical map (Italian and European) in which the nodes of the electricity grid equipped with PMU are indicated by a colored dot, selecting one or more dots you can access the action panel for the control of the data transmitted by the selected PMUs.

- Action panels: this section allows the operator to perform the main actions, such as selecting the measured quantities to be displayed and performing simple calculations in real time, such as detecting the phase shift between two points of the electricity grid. Any alarms activated in case of violations of pre-established thresholds are also reported, including high/low voltage modulus, high/low frequency, negative dumping in case of oscillations, intervention conditions for load shedding, going to the island, voltage collapse.
- Temporal trends: this section reports the temporal trends of the quantities recorded with temporal resolution up to 20 ms, this allows you to appreciate very fast dynamics.

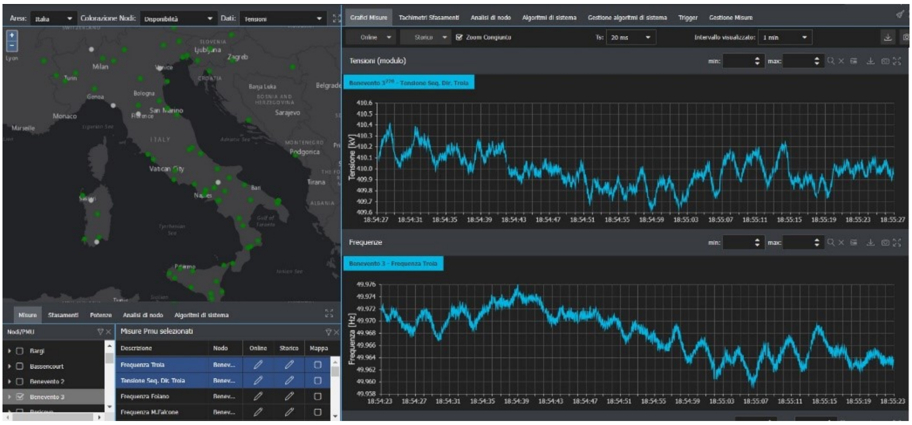

Figure 2.8 Graphical interface of WEBWAMS

2.4 PMU – Phasor Measurement Unit

The PMU (Phasor Measurement Unit) is the technology used today by Terna that allows to measure amplitude and phase of voltage and current, frequency and its derivative taken in certain nodes of the transmission network, at time instants synchronized through an absolute time signal, the Coordinated Universal Time (UTC). Therefore, the PMU is a data acquisition device that produces an estimate of synchronized phasors, called synchrophasors, and of the parameters mentioned above starting from the voltage and current measurements acquired in a synchronized manner using the GPS (Global Positioning System) satellite system. The use of GPS receivers guarantees a maximum uncertainty of the input data of 1 μs, in any geographical area of the planet. In a synchronized measurement platform, there can be two types of PMUs:

- Standalone PMU is a device in which synchronized measurement, time stamp and high-precision measurement activities are carried out in an independent device;

- Integrated PMU is a smart electronic device (IED), in which the activities carried out by an independent PMU are integrated within a multifunction device.

The reference documents for the characterization of PMUs are:
- IEC/IEEE 60255-118-1:2018 standard [19], which defines the quantities of interest, the requirements and the methods for assessing the conformity of the device, with its limits, in both dynamic and steady state conditions;
- IEEE C37.118.2-2011 standard [20], which defines the communication protocol between PMUs and PDCs for the real-time exchange of synchronized data.

2.4.1 Synchrophasors

The IEC/IEEE 60255-118-1:2018 standard provides the following definition of a synchrophasor: "a phasor calculated from data samples using a standard synchronization signal as a reference for measurement". From a quantitative point of view, a synchrophasor is nothing more than a phasor of an alternative electrical quantity at a specific frequency, calculated with reference to absolute time.
In practice, given a sinusoidal signal:

$$x(t) = X_m \cos(2\pi f t + \varphi) \tag{2.1}$$

Where X_m, f and φ are the signal amplitude, frequency and phase respectively. It is possible to express its phasorial representation X, as well known from the literature, by a complex number:

$$X = \frac{X_m}{\sqrt{2}} e^{j\,\phi} = \frac{X_m}{\sqrt{2}} (\cos\phi + j\ \sin\phi) = X_r + jX_i \tag{2.2}$$

The representative synchrophasor of the $x(t)$ signal is the X phasor defined by equation (2.2) in which ϕ is the instantaneous phase relative to a cosine function at the nominal frequency of the system synchronized to UTC. Thus, in this definition ϕ is the offset from a cosine function at the nominal frequency of the system synchronized to UTC, at the instant of time t = 0. Figure 2.9 illustrates the convention that works for the angle of the synchrophasor, showing the relationship between this and UTC time.

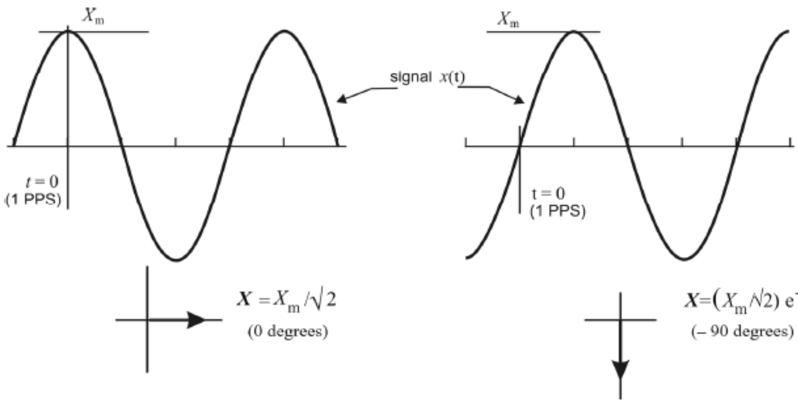

Figure 2.9 Convention for the representation of the synchrophasor and its phase angle

Synchrophasors are functions of time in modulus and phase; in fact, these will change in value unless the acquired signal is a pure sinusoid at the nominal frequency of the system (50 or 60 Hz). In the more general case the amplitude of the signal $x(t)$ is a function of time $X_m(t)$, as well as the frequency $f(t)$, then it is possible to define a function $g(t)$, also a function of time and expressed by (2.3), which represents the difference between the instantaneous frequency of the signal, f, and the nominal frequency, f_n.

$$g(t) = f(t) - f_n \tag{2.3}$$

Introduced this function then it is possible to express the sinusoid $x(t)$ as follows:

$$\begin{aligned} x(t) &= X_m(t)cos\left(2\pi\int f dt + \phi\right) \\ &= X_m(t)cos\left(2\pi\int (f_n + g)dt + \phi\right) = \\ &= X_m(t)cos\left(2\pi f_n t + \left(2\pi\int g dt + \phi\right)\right) \end{aligned} \tag{2.4}$$

For this sinusoid the representative synchrophasor turns out to be:

$$X(t) = \frac{X_m(t)}{\sqrt{2}}\, e^{j(2\pi\int g dt + \phi)} \tag{2.5}$$

In the particular case where the maximum value is constant, $X_m(t) = X_m$, and the difference between the instantaneous and nominal frequency is constant, $g(t) = g = \Delta f$, the expression of the synchrophasor is simplified, with respect to (2.4), and turns out to be a synchronized phasor rotating at the uniform speed Δf, as shown by the relation (2.6).

$$X(t) = \frac{X_m}{\sqrt{2}}\, e^{j(2\pi\Delta f t + \phi)} \qquad (2.6)$$

If a sinusoid at a nominal frequency is considered, a reference time interval equal to the period of the signal is chosen, $T_n = 1/f_n$, and observed it in the time intervals 0, T_n, $2T_n$, $3T_n$, ..., nT_0 , it is possible to derive the corresponding synchrophasors $\{X_0, X_1, X_2, X_3,.. , X_n\}$. If the frequency is different from the nominal one, $f \neq f_n$, and $f < 2f_n$ it can be observed that the synchrophasor has a constant modulus but the phase of the sequence of synchrophasors changes uniformly with step $2\pi(f - f_n)\, T_n$. In Figure 2.10 is shown a sinusoid with a frequency $f > f_n$, evaluating the synchrophasors in the integer multiple moments of the period T_n, it can be noted that the angle ϕ of the synchrophasor increases evenly with the frequency deviation. All measurements refer to a common time base and a common frequency, so that the phase angle measurements are directly comparable between the various synchronized phasors. The synchrophasor estimate also includes the effects associated with local frequency phenomena.

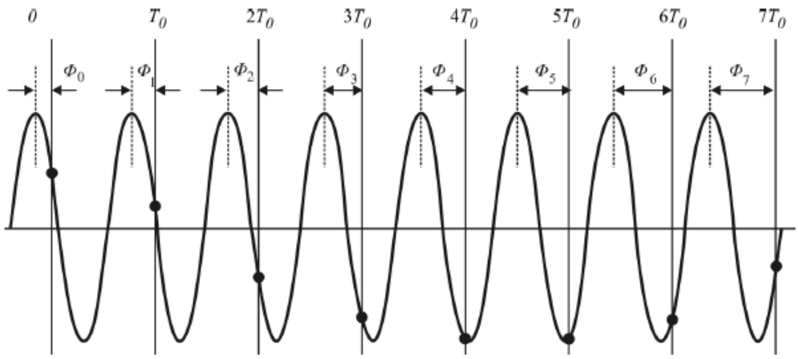

Figure 2.10 Uniform increase in the synchrophasor phase

2.4.2 Features

Figure 2.11 shows the basic architecture of a block schematized PMU.

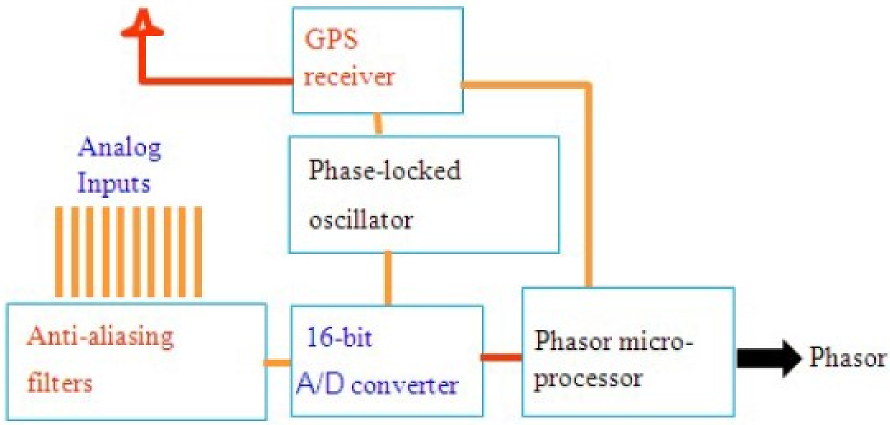

Figure 2.11 Functional block diagram of a typical PMU

At the input to the PMU there are analog signals, i.e. the alternating waveforms of voltage and current, taken from the electricity grid, with frequencies around 50 or 60 Hz (remember that the PMUs are built ad hoc to work around the electricity grid frequencies). The acquired waveforms, before being converted to digital, by means of an appropriate analog-to-digital ADC converter, are filtered through an anti-aliasing filter (64 samples for power cycle). At the input of the ADC also comes a signal from a phase-locked oscillator that allows the sampling of incoming waveforms and the synchronization of measurements, thanks to the reference time signal from the GPS receiver, which provides a Pulse Per Second (PPS). This impulse is also sent to the microprocessor, which at the output provides the estimation of the synchrophasor, frequency and other parameters of interest, with the help of algorithms that can be more or less complex. The results obtained are then transmitted to the PDC.
The synchronization signal must have suitable levels of reliability and accuracy to meet the measurement requirements of electrical systems. For each measurement, the PMU assigns a time tag (timestamp) that includes the instant of time and the "quality of time" at the time of measurement. The timestamp shall accurately determine the measurement time at least 1 μs within a specified period of 100 years. The time and quality of time for communication and recording are derived from the PMU's time tag and converted to the required format and content.
The time reference signal to which the standard refers for the evaluation of synchrophasors is the UTC (Universal Time

Coordinated), which is the time zone chosen as a global reference, from which all the time zones of the world are calculated. The UTC synchronization source can be supplied directly from a global transmission system (e.g. GPS system) or through the use of a local, external or internal clock to the same measuring device. If an internal clock is used, the standard sets the maximum timing error. Considering the levels of availability, reliability and accuracy required for applications in power grids, the only usable synchronization system is the global GPS system, thanks to which a maximum uncertainty of 1 μs is obtained on the synchronized data.
Theoretically, synchronization could also be achieved using terrestrial systems, particularly radio transmissions, achieving a significant reduction in system implementation costs. However, the accuracy of the synchronization signals achievable through the use of such systems is limited; moreover, the level of reliability and availability is currently modest, not suitable for applications in electrical systems. The reliability aspect is particularly felt by the standard, which, in order to ensure the consistency of the measurements performed, requires measurement systems to report, by means of an appropriate display system, any loss of synchronization of the system itself.
Despite a relatively simple architecture, PMUs are instruments that must provide very high performance, in terms of accuracy. In the standard, PMUs are divided into two classes:

- P-class PMUs, intended for protection applications where short response times are required, without the need for special filtering;
- M-class PMUs, employed where accuracy is more important than response speed; therefore, filtering techniques become significant.

The IEC/IEEE 60255-118-1:2018 standard states that the accuracy levels of the synchronization signal must be such as to ensure that the Total Vector Error (TVE) parameter, defined by the relation (2.7), is maintained within appropriate limits.

$$TVE = \sqrt{\frac{\left(\hat{X}_r(n) - X_r(n)\right)^2 + \left(\hat{X}_i(n) - X_i(n)\right)^2}{X_r(n)^2 + X_i(n)^2}} \tag{2.7}$$

Where $\hat{X}_r(n)$ and $\hat{X}_i(n)$ represent respectively the real and imaginary component estimated, that is, provided by the measuring device, in association with an input signal evaluated at a certain moment of time (n); while $X_r(n)$ and $X_i(n)$ indicate the corresponding theorical components, real and imaginary, of the same signal. The PMU must receive the time signal from a reliable and accurate source that can provide UTC times with sufficient accuracy to maintain the Total

Vector Error (TVE), Frequency Error (FE) and the Rate of change of Frequency Error (RFE or ROCOF error) within the limits prescribed by the standard.
If, for example, the frequency evaluated by the PMU coincides with the theorical one, the phasorial representation will be stationary (invariant time) and the phasor coordinates will remain constant over time. In this case, the TVE parameter is zero ($TVE = 0$). In practical cases, which are characterized by a deviation between the theoretical value of the signal frequency and the measured value, it will be possible to observe continuous oscillations of the phasor in the complex plane, as shown above by relation (2.6). The TVE parameter represents a characteristic index of these oscillations and its value is proportional to the magnitude of the frequency offsets.
For complete details, the definitions of the other two measurement errors in the standard are given: relation (2.8) expresses the Frequency Error (FE), and relation (2.9) and the Rate of change of Frequency Error (RFE or ROCOF error).

$$FE = |f_{reale} - f_{misurata}| = |\Delta f_{reale} - \Delta f_{misurata}| \tag{2.8}$$

$$RFE = \left|\left(\frac{df}{dt}\right)_{reale} - \left(\frac{df}{dt}\right)_{misurata}\right| \tag{2.9}$$

Obviously, the real value and the measured value refer to the same instant of time, which is provided by the timestamp of the estimated values.
The standard specifies the requirements that the PMU must meet, through its own estimates, to be considered uniform to the standard itself: the PMU must provide the measurement of synchrophasors, frequency and ROCOF in accordance with the requirements of the standard. These requirements must be met at all times and in all configurations, whether the PMU function is an independent physical unit or included as part of a multifunction unit; also for both steady state operating conditions and dynamic conditions.
Steady-state conformity must be confirmed by comparing evaluations of the synchrophasor, frequency and ROCOF, obtained under steady-state conditions at the corresponding theoretical values of the real (X_r) and imaginary (X_i) synchrophasor components, frequency and ROCOF.
Stationary conditions occur in the case when the amplitude of the test signal, its pulsation (ω) and its phase (φ), and all other influence quantities are constant for the measurement period.
Table 2.1, extracted from the IEC/IEEE 60255-118-1:2018 standard, shows the maximum values of the TVE that must guarantee the PMU in stationary conditions for the estimation of the synchrophasor.

Table 2.1 Maximum values of the TVE under stationary conditions for the estimation of synchrophasors

Influence quantity	Reference condition	Minimum range of influence quantity over which PMU shall be within given TVE limit			
		Performance – P class		Performance – M class	
		Range	Max. TVE %	Range	Max. TVE %
Signal frequency	Frequency $= f_0$ ($f_{nominal}$)	± 2,0 Hz	1	± 2,0 Hz for $F_s < 10$ $\pm F_s/5$ for $10 \le F_s < 25$ ± 5,0 Hz for $F_s \ge 25$	1
Voltage signal magnitude	100 % rated	80 % to 120 % rated	1	10 % to 120 % rated	1
Current signal magnitude	100 % rated	10 % to 200 % rated	1	10 % to 200 % rated	1
Harmonic distortion (single harmonic)	< 0,2% (THD)	1 %, each harmonic up to 50th	1	10 %, each harmonic up to 50th	1
Out-of-band interference as described below	< 0,2% of input signal magnitude		None	10 % of input signal magnitude for $F_s \ge 10$. No requirement for $F_s < 10$.	1,3

Out-of-band interference testing:

The input test signal frequency f_{in} is varied between f_0 and ± 10 % of $F_s/2$ with the maximum variation limited to ± 5 Hz.

These limits are: $f_0 - 0{,}1\,(F_s/2) \le f_{in} \le f_0 + 0{,}1\,(F_s/2)$ for $F_s \le 100$ and $f_0 - 5 \le f_{in} \le f_0 + 5$ for $F_s > 100$

where

F_s is the phasor reporting rate (in Hz);

f_0 is the nominal system frequency (in Hz);

f_{in} is the fundamental frequency of the input test signal (in Hz).

The passband at each reporting rate is defined as $|f - f_0| < F_s/2$. An interfering signal outside the filter passband is a signal at frequency f where: $|f - f_0| \ge F_s/2$

Compliance with out-of-band rejection can be confirmed by using a single frequency sinusoid added to the fundamental power signal at the required magnitude level. The minimum sinusoid frequency range shall be 10 Hz to the second harmonic ($2 \times f_0$), excluding the passband. These frequencies shall include the frequencies $f_0 \pm F_s/2$, 10 Hz, the second harmonic ($2 \times f_0$), and enough frequency points to clearly determine the response. This should include frequencies with exponentially narrower intervals near the passband limit frequencies as follows:

– frequency points below the passband using frequencies $f = f_0 - F_s/2 - (0{,}1\text{ Hz} \times 2^n)$ for n = 0, 1, 2 ... until $f \le 10$ Hz; and

– frequency points above the passband using frequencies $f = f_0 + F_s/2 + (0{,}1\text{ Hz} \times 2^n)$ for n = 0, 1, 2 ... until $f \ge 2 \times f_0$ Hz.

For the special case where $F_s = 2 \times f_0$, all frequencies from 0 to $2 \times f_0$ are in-band, so OOB testing will be done from the 2nd to 3rd harmonic; that is $2 \times f_0 \le f \le 3 \times f_0$.

With regard to the requirements to be met for frequency and ROCOF in terms of errors, Table 2.2 shows the requirements extracted from the IEC/IEEE 60255-118-1:2018 standard.

Table 2.2 Requirements for frequency and ROCOF estimation under stationary conditions

<table>
<tr><th rowspan="2">Influence quantity</th><th rowspan="2">Reference condition</th><th colspan="4">Error requirements for compliance</th></tr>
<tr><th colspan="2">P class</th><th colspan="2">M class</th></tr>
<tr><td rowspan="3">Signal frequency</td><td rowspan="3">Frequency = f_0 ($f_{nominal}$)
Phase angle constant</td><td colspan="2">Range: f_0 ± 2,0 Hz</td><td colspan="2">Range:
f_0 ± 2,0 Hz for $F_s \le 10$
± $F_s/5$ for $10 \le F_s < 25$
± 5,0 Hz for $F_s \ge 25$</td></tr>
<tr><td>Max. |FE|</td><td>Max. |RFE|</td><td>Max. |FE|</td><td>Max. |RFE|</td></tr>
<tr><td>0,005 Hz</td><td>0,4 Hz/s</td><td>0,005 Hz</td><td>0,1 Hz/s</td></tr>
<tr><td rowspan="4">Harmonic distortion (same as Table 2)
(single harmonic)</td><td rowspan="2">< 0,2 % THD</td><td colspan="2">1 % each harmonic up to 50th</td><td colspan="2">10 % each harmonic up to 50th</td></tr>
<tr><td>Max. |FE|</td><td>Max. |RFE|</td><td>Max. |FE|</td><td>Max. |RFE|</td></tr>
<tr><td>F_s > 20</td><td>0,005 Hz</td><td>0,4 Hz/s</td><td>0,025 Hz</td><td>No requirements</td></tr>
<tr><td>$F_s \le 20$</td><td>0,005 Hz</td><td>0,4 Hz/s</td><td>0,005 Hz</td><td>No requirements</td></tr>
<tr><td rowspan="3">Out-of-band interference (same as Table 2)</td><td rowspan="3">< 0,2 % of input signal magnitude</td><td colspan="2">No requirements</td><td colspan="2">Interfering signal 10 % of signal magnitude</td></tr>
<tr><td></td><td></td><td>Max. |FE|</td><td>Max. |RFE|</td></tr>
<tr><td>None</td><td>None</td><td>0,01 Hz</td><td>No requirements</td></tr>
</table>

With regard to dynamic operating conditions, the requirements must be verified in several scenarios:

- linear ramp variation of the frequency;
- step variation of the amplitude of voltage tern;
- step variation of the phase of the voltage tern;
- step variation in both amplitude and phase of the voltage tern;
- latency test.

With regard to the evaluation of synchrophasors, the standard does not recommend a specific algorithm to be implemented in PMUs, but leaves freedom to individual manufacturers as long as they meet the compliance requirements of the measures in the standard. However, the standard provides guidelines regarding the management and transmission of data, thus ensuring correlation of large amounts of data from different measurement units, typically present in a monitoring system of the transmission network.

One parameter that is set by the standard is the rate of phasor evaluations per second (Fs) that the PMU must support. This speed is called frames per second (fps), where frame means a set of measures of synchrophasors, frequencies and/or ROCOF characterized by the same timestamp (this term is used to differentiate a data frame from a sample, which means a point of an analog waveform).

The transmission rates can be chosen by the user among the values dictated by the standard, these are submultiples of the nominal frequency of the electricity grid and are shown in Table 2.3.

Table 2.3 Allowable values of the observation rate of PMUs

System frequency	50 Hz			60 Hz					
Reporting rates (F_s—frames per second)	10	25	50	10	12	15	20	30	60

This type of choice is made so that the measurements are equally spaced over the second of observation. The choice of higher speeds, multiples of the network frequency, such as 100 fps or 120 fps is also allowed; a speed of 1 fps is also permitted.

Having fixed Fs then the number N of observations to be made in one second is established, after that, it is necessary to associate each data output from the measurement units with a specific time tag in order to uniquely characterize the measured quantity. The time tags associated with each synchrophasor are identified by a number (frame number) ranging from 0 up to N-1.

The standard gives an example of estimating synchrophasors for the waveforms in Figure 2.9. These values are shown for the angles of 0° and -90° at the time marker of 1 PPS provided by the GPS.

Table 2.4 shows the example of a phasorial representation, in terms of amplitude and phase, of a sinusoidal quantity with effective value $X_m/\sqrt{2}$ observed at a speed of 10 fps, so ten synchrophasors (N = 10) per second. The results reported are related to the case of signals characterized by a frequency value (respectively 50, 60, 51 and 61 Hz) that remains constant throughout the observation range.

Table 2.4 Synchrophasor values captured at 10 fps speed

Time	Fractional time		Synchrophasor values for: 50 Hz frequency—50 Hz system 60 Hz frequency—60 Hz system		Synchrophasor values for: 51 Hz frequency—50 Hz system 61 Hz frequency—60 Hz system	
Second	Frame number	Fractional second	Synchrophasor (0 degrees)	Synchrophasor (–90 degrees)	Synchrophasor (0 degrees)	Synchrophasor (–90 degrees)
k–1	9	0.900000	$X_m/\sqrt{2}, \angle 0°$	$X_m/\sqrt{2}, \angle -90°$	$X_m/\sqrt{2}, \angle -36°$	$X_m/\sqrt{2}, \angle -126°$
k	0	0.000000	$X_m/\sqrt{2}, \angle 0°$	$X_m/\sqrt{2}, \angle -90°$	$X_m/\sqrt{2}, \angle 0°$	$X_m/\sqrt{2}, \angle -90°$
k	1	0.100000	$X_m/\sqrt{2}, \angle 0°$	$X_m/\sqrt{2}, \angle -90°$	$X_m/\sqrt{2}, \angle 36°$	$X_m/\sqrt{2}, \angle -54°$
k	2	0.200000	$X_m/\sqrt{2}, \angle 0°$	$X_m/\sqrt{2}, \angle -90°$	$X_m/\sqrt{2}, \angle 72°$	$X_m/\sqrt{2}, \angle -18°$
k	3	0.300000	$X_m/\sqrt{2}, \angle 0°$	$X_m/\sqrt{2}, \angle -90°$	$X_m/\sqrt{2}, \angle 108°$	$X_m/\sqrt{2}, \angle 18°$
k	4	0.400000	$X_m/\sqrt{2}, \angle 0°$	$X_m/\sqrt{2}, \angle -90°$	$X_m/\sqrt{2}, \angle 144°$	$X_m/\sqrt{2}, \angle 54°$
k	5	0.500000	$X_m/\sqrt{2}, \angle 0°$	$X_m/\sqrt{2}, \angle -90°$	$X_m/\sqrt{2}, \angle 180°$	$X_m/\sqrt{2}, \angle 90°$
k	6	0.600000	$X_m/\sqrt{2}, \angle 0°$	$X_m/\sqrt{2}, \angle -90°$	$X_m/\sqrt{2}, \angle -144°$	$X_m/\sqrt{2}, \angle 126°$
k	7	0.700000	$X_m/\sqrt{2}, \angle 0°$	$X_m/\sqrt{2}, \angle -90°$	$X_m/\sqrt{2}, \angle -108°$	$X_m/\sqrt{2}, \angle 162°$
k	8	0.800000	$X_m/\sqrt{2}, \angle 0°$	$X_m/\sqrt{2}, \angle -90°$	$X_m/\sqrt{2}, \angle -72°$	$X_m/\sqrt{2}, \angle -162°$
k	9	0.900000	$X_m/\sqrt{2}, \angle 0°$	$X_m/\sqrt{2}, \angle -90°$	$X_m/\sqrt{2}, \angle -36°$	$X_m/\sqrt{2}, \angle -126°$
k+1	0	0.000000	$X_m/\sqrt{2}, \angle 0°$	$X_m/\sqrt{2}, \angle -90°$	$X_m/\sqrt{2}, \angle 0°$	$X_m/\sqrt{2}, \angle -90°$

The measurement time instant must consist of three numbers: a second of century count (SOC), a fraction of a second count (FRACSEC), and a

message time quality indicator.
The SOC count is a count of seconds from midnight (00:00:00) on January 1, 1970 to the second in which the measurement took place. This count must be represented as a 32-bit unsigned integer. From this count, intercalary seconds must be added or deleted as needed to keep it synchronized with UTC. The time count can always be determined by the current time by multiplying the number of days from 01/01/1970 by the number of seconds per day (86400 s). The second must be divided by an integer number of subdivisions defined as TIME_BASE. The term FRACSEC is an integer and must be zero when it coincides with the flipping of one second.
The transmission of data in real time from the PMU to the PDC takes place according to a precise communication protocol, below are the main reference standards that have been developed over the years:

- IEEE 1344-1995;
- IEC 61850-90-5;
- IEEE C37.118-2005;
- IEEE C37.118.2-2011;
- IEC/IEEE 60255-118-1:2018.

During my research activity the IEEE C37.118.2-2011 standard was used for the real-time transmission of data from PMUs; therefore, in the next paragraph an overview of this standard is made.

2.5 STANDARD IEEE C37.118

The IEEE C37.118.2-2011 standard, called "*IEEE Standard for Synchrophasor Data Transfer for Power Systems",* defines a method for exchanging synchronized data between equipment in the electrical power system, namely measuring devices (PMUs) and data concentrators (PDCs). Defines messaging framework requirements for synchronized measurements, including message types, usage, content, and data formats. It does not place any restrictions on the means of communication used and the communication protocol, since these are typically dependent on the application. This method was established by the IEEE C37.118-2005 standard.
Mainly, the standard was designed for RS-232 serial communication, but past implementations show great success of fiber optic IP telecommunications, using TCP/IP (*Transmission Control Protocol*) and/or UDP (User Datagram Protocol).
The standard is divided into six paragraphs, of particular interest is the sixth paragraph in which the real time communication protocol and the format of the messages are defined; the first five paragraphs, on the other hand, recall concepts on synchrophasors, already present in the first part of the IEEE C37.118-2011 (now replaced with the standard IEC/IEEE 60255-118-1:2018).
A simple structure of a synchronized phasor network consists of PMUs

and PDCs, as shown in Figure 2.12, an example shown in the first part of the standard. If, for example, there are multiple Intelligent Electronic Devices (IEDs) in a substation that provide synchrophasor measurements (PMUs), a local PDC can be installed in the substation. Typically, many PMUs located in various key substations collect and send real-time data to a PDC located at a station, where the data is aggregated.

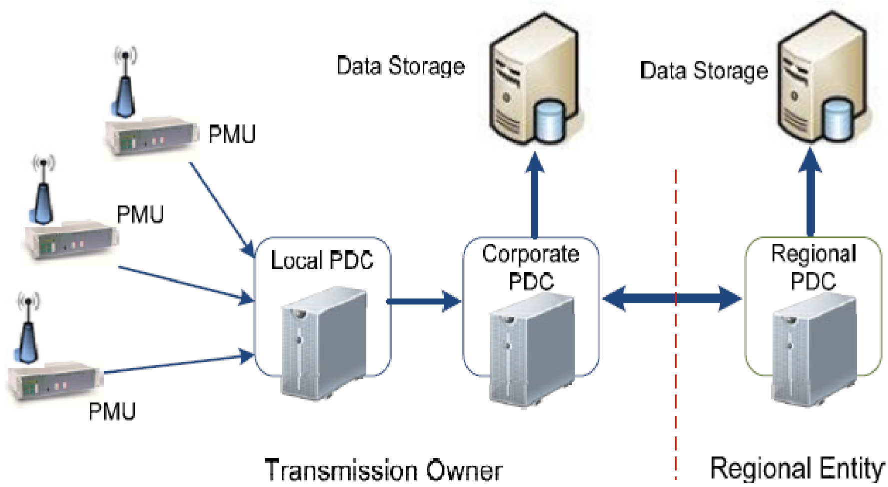

Figure 2.12 Example of a simple synchronized data collection network

The data collected by the PDC can be used to support many applications, ranging from displaying information and alarms to monitor the situation, to those that provide sophisticated analytical, control or protection capabilities. Applications, such as monitoring network dynamics, use full-resolution real-time data along with network models to support both operational and planning functions. The application shows locally measured frequency, primary voltages, currents, real and reactive power flows and other quantities for system operators. Local PDCs can be connected to a central PDC (Super PDC) to aggregate data between the various measuring stations, in order to provide a snapshot of the measurements of the electricity grid at the interconnection level.
Real-time data transmission takes place in conjunction with the measurement process. If the PMU device is to be used with other systems where phasor information is to be transmitted in real time, implementation of this protocol is required for compliance with this standard. If the PMU device is used only for data storage or recording, then this protocol is not mandatory. Any communication system, or medium, can be used for data transmission. Message frames are transmitted in their entirety. This messaging protocol can be used to communicate with a single PMU or with a secondary system that receives data from multiple PMUs. The secondary system, a PDC, must be assigned its own identification code, IDCODE, assigned by the user.

The protocol allows the use of the necessary identifying information, such as PMU IDCODE and system state, to be incorporated into the data structure, for a correct interpretation of the measured data.

2.6 Developed Benchmark

The progress achieved in the field of simulation, together with the technological innovations introduced with the fourth industrial revolution, have led to an important turning point: today it is no longer necessary to create expensive physical prototypes to test the performance of an object, of a system, but it can be done through the use of a Digital Twin, now considered an indispensable tool in innovation projects in the field of IoT (Internet of Things). By Digital Twin, therefore, we mean the virtual copy of a physical system, a fictitious representation that allows you to virtually analyze new scenarios and strategies before implementing them in the real physical system. The purposes for which it can be used are manifold, including:

- perform simulations without affecting the physical system;
- observe the response of the system in different scenarios, with particular attention to situations of high stress, allowing the identification of any discrepancies in operation;
- perform predictive analysis;
- tuning of estimation algorithms.

The Digital Twin is used, in particular, in the engineering phase. In fact, during the development of a new product, many questions emerge, for example what to modify from a structural and morphological point of view to have an optimization of a certain objective function. It provides well-defined answers, reproducing the operating conditions of the system whenever a change in its configuration is made.
In the Italian transmission grid managed by Terna there are about 220 PMUs that acquire the measurements of the quantities to be observed (module and phase of the voltage, frequency, etc.), these are sent to a PDC; therefore, in the benchmark to be realized it is necessary to create a PMU emulator.
As previously described, the data sent by the individual PMUs have their own timestamp, so before they can be sent to the openECA software that it allows projects to be created in different programming languages (i.e. Matlab), used in the benchmark as a frame reception software from the PDC and conversion into data format that can be processed by computers (i.e. Matlab), a synchronization and alignment operation in a single frame. For this purpose, openPDC is used. Both of the software mentioned are open source and made available by the GPA (Grid Protection Alliance). This description concerns the structure of the benchmark for WAMS in the most generic case, Figure 2.14 illustrates a schematization.

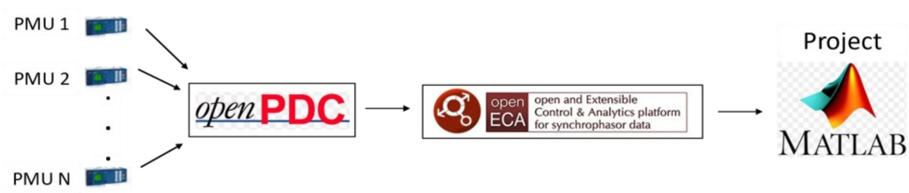

Figure 2.13 Benchmark structure for WAMS simulation in the most generic case

Chapter 3

3 Analyzed Methodologies

In this chapter all the methodologies analyzed in the doctoral course are described; in Chap. 4 the results obtained for each methodology on both simulated and real signals are reported.
The choice of methodologies was made both considering what was used by Terna at the beginning of the doctoral work and after a deep analysis of what was already available in the literature.
The methodologies analyzed can be divided into:

- Single channel methods
- Multi channel methods

In particular, the single channel methods analyzed are:

- Hilbert Transform
- Kalman Filter
- Genetic Algorithm
- Particle Swarm Optimization
- Tuft Kumaresan

While the multi channel method analyzed is:

- Dynamic Mode Decomposition (DMD)

As can be seen in the results obtained and reported in Chapter 4, the DMD method has many advantages in view of the possibility on the part of the TSO to acquire from different points the synchronized measurements along the entire European electrical system.

3.1 Hilbert Transform

The Hilbert transform is a particular representation that, unlike other transforms (Fourier, Laplace, Z) does not realize a change in the domain of definition. In other words, starting from a function of time, the Hilbert transform is still a function of time. The Hilbert transform of a real signal $a(t)$ is defined as the following convolution integral:

$$H[a(t)] = \frac{1}{\pi} V.P. \int_{-\infty}^{+\infty} \frac{a(\tau)}{t-\tau} d\tau = \frac{1}{\pi} V.P. \int_{-\infty}^{+\infty} \frac{a(t-\tau)}{\tau} d\tau \quad (3.1)$$

where it is necessary **to consider the Cauchy main value integral** (V.P.) because of the possible singularity of the integrand at values $\tau = t$ and $\tau = 0$. The usefulness of employing this operator lies in the property of the Hilbert transform to phase shift the real signal with positive pulsation of $-\frac{\pi}{2}$ radians. Thanks to this feature it is possible to obtain the analytical signal [21]:

$$\begin{gathered} g(t) = a(t) + j \cdot a_H(t) = A(t) \cdot e^{j\vartheta(t)} \\ A(t) = \sqrt{a(t)^2 + a_H(t)^2} \\ \vartheta(t) = arctan\left(\frac{a_H(t)}{a(t)}\right) \end{gathered} \quad (3.2)$$

- $a_H(t) = H[a(t)]$;
- $A(t)$ = instantaneous amplitude of the analytical signal;
- $\vartheta(t)$ = instantaneous phase of the analytical signal.

In 1948 Ville introduced the notion of instantaneous frequency (IF) in the field of signal processing as the derivative of the "analytical signal" phase:

$$\begin{gathered} f(t) = \frac{1}{2\pi} \frac{d\vartheta_u(t)}{dt} \quad with \quad \vartheta_u(t) = \vartheta(t) + \Lambda(t) \\ \zeta(t) \; = \; -\frac{d}{dt}[ln\,(A(t)] \end{gathered} \quad (3.3)$$

Where $\vartheta(t)$ is the phase of the analytical signal $g(t)$ and the term $\Lambda(t)$ is an integer multiple of π, function placed to ensure phase continuity. The **first property** of the Hilbert transform concerns the continuity and differentiability of the amplitude:

$$H[a(t) + \delta a(t)] \rightarrow H[a(t)] \;\; se \; \|\delta a(t)\| \rightarrow 0 \quad (3.4)$$

The **second property** of the Hilbert transform concerns the homogeneity and independence of the phase from scaling operations. If the signal $a(t)$ is replaced with $k \cdot a(t)$, using the linearity of the transformation it is shown that:

$$\frac{H[k \cdot a(t)]}{k \cdot a(t)} = \frac{H[a(t)]}{a(t)} \rightarrow H[k \cdot a(t)] = k \cdot H[a(t)] \tag{3.5}$$

The **third property** of the Hilbert transform concerns the harmonic correspondence. Assuming constant and positive the amplitude and frequency of a sinusoidal signal, for every A, f and φ it is shown that:

$$H[A \cdot cos(\omega t + \varphi)] = A \cdot sin(\omega t + \varphi) \tag{3.6}$$

3.1.1 Bedrosian's Theorem

Statement

According to Bedrosian's theorem [22], it is possible to establish a fundamental result for the Hilbert transform, i.e. in the case of a product transform, if the functions meet the following conditions:

- the spectrum of $f(x)$ shows frequencies lower than those included in $g(x)$;
- the spectrum of $g(x)$ shows frequencies higher than those included in $f(x)$;
- the spectra of $f(x)$ and $g(x)$ are not overlapping at any point;

then:

$$H[f(x) \cdot g(x)] = f(x) \cdot H[g(x)] \tag{3.7}$$

where $f(x)$ and $g(x)$ are two generic complex functions of the x variable in $L^2(R)$ [23,24]. The term $H[g(x)]$ corresponds to the Hilbert transform of $g(x)$, which can be represented equivalently as follows:

$$H[g(x)] = \frac{1}{\pi} V.P. \int_R \frac{g(y)}{x-y} dy \tag{3.8}$$

Demonstration

The Bedrosian's identity can be proved through the following steps. Consider the Fourier transform of the product $f(x)g(x)$:

$$H[f(x) \cdot g(x)] = H\left[\frac{1}{(2\pi)^2} \int_{-\infty}^{+\infty} ds \int_{-\infty}^{+\infty} F(s)G(t)e^{j(s+t)x} dt\right] \tag{3.9}$$

using a well-known result of the Hilbert transform, i.e. $H\left[e^{jkx}\right] = j\ sgn(k)\ e^{jkx}$, the equation can be rewritten as follows:

$$H[f(x) \cdot g(x)] = \frac{1}{(2\pi)^2} \int_{-\infty}^{+\infty} ds \int_{-\infty}^{+\infty} F(s)G(t) \cdot \mathrm{jsgn(s+t)} \cdot e^{j\mathrm{(s+t)}x} dt \quad (3.10)$$

Now, since the value of sgn(s + t) coincides globally with sgn(t) in the integration region (where the integrating $F(s)G(t)$ is non-zero), the above equation becomes:

$$H[f(x) \cdot g(x)] = f(x) \cdot \frac{1}{2\pi} \int_{-\infty}^{+\infty} G(t) \cdot \mathrm{jsgn(t)} \cdot e^{j\mathrm{tx}} dt \quad (3.11)$$

The term that multiplies $f(x)$ is exactly the Hilbert transform of the function $g(x)$ in fact:

$$H[g(x)] = \frac{1}{2\pi} \int_{-\infty}^{+\infty} G(t) \cdot \mathrm{H}[\, e^{j\mathrm{tx}}]\, dt = \frac{1}{2\pi} \int_{-\infty}^{+\infty} G(t) \cdot \mathrm{jsgn(t)} \cdot e^{j\mathrm{tx}} dt \quad (3.12)$$

so, as it was intended to prove:

$$H[f(x) \cdot g(x)] = f(x) \cdot H[g(x)] \quad (3.13)$$

The result found corresponds to the Hilbert transform of the product of a low-frequency $f(x)$ function and a high-frequency $g(x)$ function whose spectra are therefore not overlapping. The conditions described above are fundamental for the validity of the result of Bedrosian's theorem and therefore to obtain a correct formulation of the analytical signal.

Some critical issues

In order to clarify this aspect, an example available in the literature is reported, where, the signal, whose analytical representation is to be obtained, does not meet the conditions of Bedrosian's theorem. Consider then the signal $x(t)$:

$$x(t) = \sin(2\pi f t) + \sin(2\pi 2 f t) \quad (3.14)$$

which can be represented equivalently, using prostapheresis formulas, as follows:

$$x(t) = 2\sin\left(2\pi \frac{3}{2} f t\right) \cos\left(2\pi \frac{1}{2} f t\right) = A(t) \cdot \cos(\vartheta(t)) \quad (3.15)$$

- $A(t) = 2\sin\left(2\pi \frac{3}{2} f t\right)$;

- $\vartheta(t) = 2\sin\left(2\pi\frac{1}{2}ft\right)$.

As it is clearly visible from their expression, the amplitude $A(t)$ changes with a speed that is three times higher than that of the phase $\vartheta(t)$. It is clear that the proposed signal does not comply with the conditions of Bedrosian's theorem.
Consider the following terms:

$$y_B = A(t)\cdot H\big[\cos(\vartheta(t))\big] = 2\sin\left(2\pi\frac{3}{2}ft\right)\sin\left(2\pi\frac{1}{2}ft\right)$$
$$y_H = H\big[A(t)\cdot\cos(\vartheta(t))\big] = H\left[2\sin\left(2\pi\frac{3}{2}ft\right)\cos\left(2\pi\frac{1}{2}ft\right)\right] \tag{3.16}$$

- y_B = quadrature signal at $x(t)$ calculated with the Bedrosian identity;
- y_H = quadrature signal at $x(t)$ calculated with Hilbert applied to the whole signal.

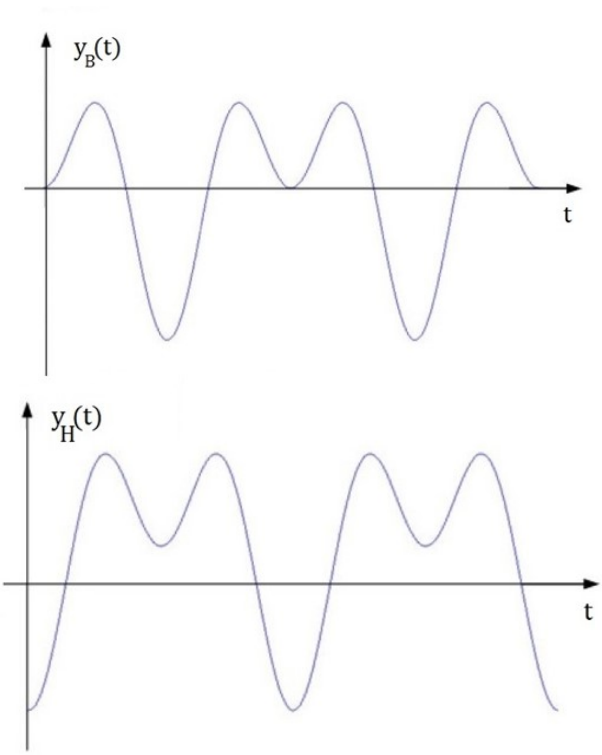

Figure 3.1 Graphical representation of the two signals

From Figure 3.1 it is directly clear that in this case the result obtained

with the Bedrosian identity does not apply, as the two quadrature signals differ [25].
In the case of **inter-area oscillations**, the function that typically describes the trend of the i-th mode is:

$$A_i \cdot e^{\sigma_i t} \cdot \cos(\omega t) \tag{3.17}$$

In this case compliance with the conditions of Bedrosian is ensured if the relationship $\frac{\boldsymbol{\sigma}}{\boldsymbol{\omega}} \ll \mathbf{1}$.

3.1.2 Methods of Eliminating the Gibbs Effect

The Hilbert transform of a signal is characterized by the Gibbs effect (edge effect), because of the signal discontinuity [26]. The effect is manifested by visible discrepancies between the initial and final values of the original mono-component signals and those calculated by the proposed decomposition method, which uses H.T. The $Matlab^{®}$ standard algorithm for calculating H.T. is not exempt from this, as can be clearly seen in Figure 3.2.

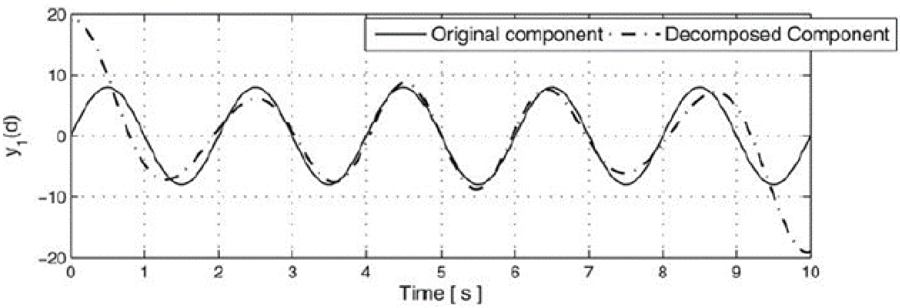

Figure 3.2 Gibbs effect on $Matlab^{®}$ standard algorithm

In order to improve the result of the transform, the Hilbert-Boche method is proposed.

Hilbert-Boche Method

Boche's algorithm uses equations that originate from the Nyquist–Shannon sampling theorem [27]. Given an analog signal $y(t)$ in $L^2(R)$, of limited band and such that the sampling rate, F_s, is greater than 2 times the maximum frequency, F_{max}, of the signal, $F_s > 2F_{max}$, (therefore belonging to the class W_π), sampled in n values y_i at discrete and equispaced instants t_i, there will be a function $g \in W_\pi$ such that:

$$g(t_i) = y_i$$
$$g\,(t) = \sum_{k=1}^{n} b_{k,n} \cdot \frac{\sin\,(\pi(t-t_k))}{\pi(t-t_k)} \tag{3.18}$$
$$g_n\,(t_i) = \sum_{k=1}^{n} b_{k,n} \cdot \frac{\sin\,(\pi(t_i-t_k))}{\pi(t_i-t_k)}$$

For the calculation of coefficients $b_{k,n}$ it is enough to solve the following system of n linear equations:

$$\begin{bmatrix} g_n\,(t_1) \\ \vdots \\ g_n\,(t_n) \end{bmatrix} = \begin{bmatrix} a_{11} & \cdots & a_{1n} \\ \vdots & a_{ik} & \vdots \\ a_{n1} & \cdots & a_{nn} \end{bmatrix} x \begin{bmatrix} b_{1n} \\ \vdots \\ b_{nn} \end{bmatrix} \tag{3.19}$$

where the terms $a_{ik} = \frac{\sin\,(\pi(t_i-t_k))}{\pi(t_i-t_k)} = \text{sinc}\,(t_i - t_k)$.

Thanks to the particular properties of the class W_π, the punctual convergence of the series g_n is guaranteed. Once the coefficients $b_{k,n}$ have been determined, the H.T. of $g_n(t)$ is considered:

$$H\{g\}(t) = \sum_{k=1}^{n} b_{k,n} \cdot \frac{1-\cos\,(\pi(t-t_k))}{\pi(t-t_k)} \tag{3.20}$$

Since the coefficients $b_{k,n}$ are already known, this equation gives the numerical approximation of the Hilbert transform.

The great advantage of this method lies in the significant **reduction of the Gibbs effect**.

Figure 3.3 shows the differences between the mono-component signals calculated using the $Matlab^{®}$ standard H.T. and the Hilbert-Boche method. The original signal is characterized as follows:

$$y(t) = 20e^{-0.3t}\sin(\pi t) + 8e^{-0.1t}\sin(\pi t)$$
$$with\; T_s = 0.02\; s\; and\; T_{acq.} = 10s \tag{3.21}$$

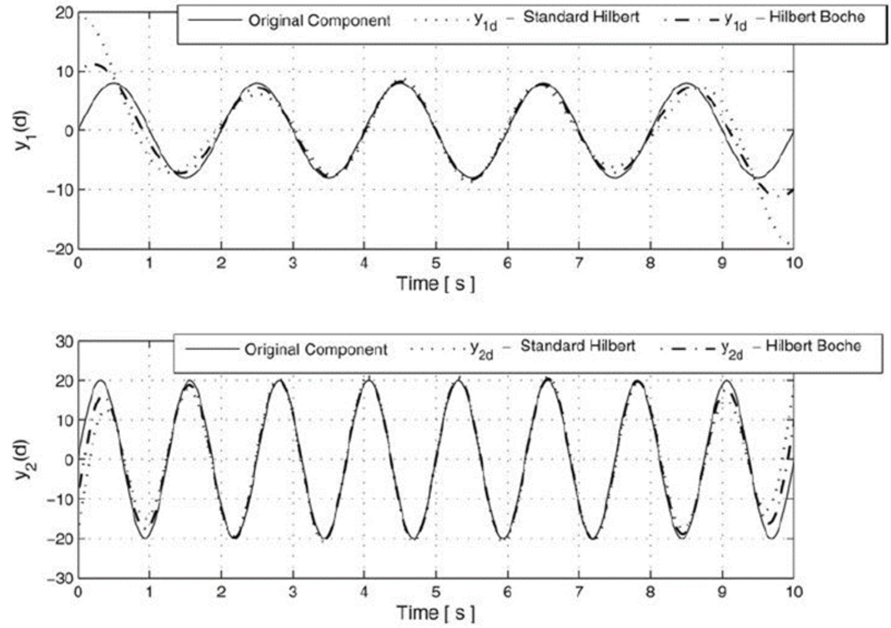

Figure 3.3 Hilbert-Boche method

3.1.3 Method of Decomposition

Decomposition theorem

Statement

In order to obtain the mono-component signals, each characterized by a single frequency, the following method is proposed. Let $y(t)$ be a generic real signal of the variable t in $L^2(-\infty,+\infty)$, characterized by the sum of m signals whose frequencies are $f_1, f_2, \dots, f_m$. Let $\hat{F}(\omega)$ be the Fourier transform of the $y(t)$ signal. This can be decomposed into m elementary signals ${y_i}^d(t)$, whose Fourier spectrum ${\hat{Y}_i}^d(\omega)$ is equivalent to $\hat{F}(\omega)$ within the i-th interval and is zero elsewhere, as shown in Figure 3.4.

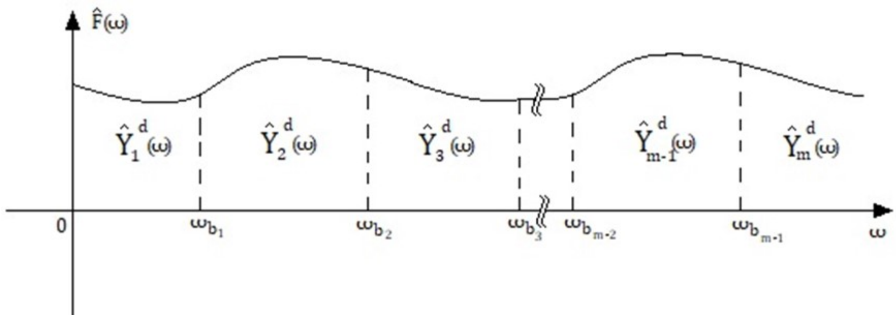

Figure 3.4 Spectra of the signal components

The m mutually exclusive intervals are defined through specific angular frequencies ω_{b_i} called **bisector angular frequencies**. In particular, $\omega_{b_i} \in [\omega_{b_1}, \omega_{b_{m-1}}]$ and will be calculated as an average of the frequencies of 2 signals, with contiguous interval. With this subdivision, each narrowband signal can be determined as follows:

$$y\ (t) = \sum_{i=1}^{m} y_i{}^d(t)$$
$$y_i{}^d(t) = s_i\ (t) - s_{i-1}\ (t)\ , \dots ,\ y_m{}^d\ (t) = y\ (t) - s_{m-1}\ (t)\ with\ s_0\ (t) = 0 \tag{3.22}$$

where each term $s_i\ (t)$ is calculated as:

$$s_i\ (t) = \sin(\omega_{b_i} t)\, H[y(t) \cos(\omega_{b_i} t)] - \cos(\omega_{b_i} t)\, H[y(t) \cos\ (\omega_{b_i} t)] \tag{3.23}$$

Demonstration

A generic signal $y(t)$ can be represented as the sum of two signals $s_1\ (t)$ and $\overline{s_1}\ (t)$, whose Fourier transform $\widehat{s_1}\ (\omega)$ and $\widehat{\overline{s_1}}(\omega)$ cancels out for $|\omega| > \omega_b$ and $|\omega| < \omega_b$, respectively.

$$\begin{cases} \widehat{s_1}\ (\omega) = \begin{cases} 0, & |\omega| > \omega_b \\ \dfrac{\hat{F}(\omega)}{2}, & |\omega| = \omega_b \\ \hat{F}(\omega), & |\omega| < \omega_b \end{cases} \\ \widehat{\overline{s_1}}(\omega) = \begin{cases} 0, & |\omega| < \omega_b \\ \dfrac{\hat{F}(\omega)}{2}, & |\omega| = \omega_b \\ \hat{F}(\omega), & |\omega| > \omega_b \end{cases} \end{cases} \tag{3.24}$$

The angular frequency ω_b is an arbitrary positive value, defined as the bisector angular frequency. This property together with **Parseval's theorem** in the Fourier transform, allows to establish that $s_1(t)$ and $\overline{s_1}\ (t)$ are real functions in$L^2(-\infty, +\infty)$:

$$\int_{-\infty}^{+\infty} |s_1\,(t)|^2 dt = \int_{-\infty}^{+\infty} |\widehat{\overline{s_1}}(\omega)|^2 d\omega \leq \frac{1}{2\pi}\int_{-\infty}^{+\infty} \left|\hat{F}(\omega)\right|^2 d\omega$$
$$= \int_{-\infty}^{+\infty} |y\,(t)|^2 dt < \infty$$
$$\int_{-\infty}^{+\infty} |\overline{s_1}(t)|^2 dt = \int_{-\infty}^{+\infty} \left|\widehat{\overline{s_1}}(\omega)\right|^2 d\omega \leq \frac{1}{2\pi}\int_{-\infty}^{+\infty} \left|\hat{F}(\omega)\right|^2 d\omega \tag{3.25}$$
$$= \int_{-\infty}^{+\infty} |y\,(t)|^2 dt < \infty$$

To prove the statement, consider the functions $s_a\,(t) = \cos(\omega_b t)$ and $s_b\,(t) = \sin\,(\omega_b t)$ whose Fourier transform is non-zero within the same mutually exclusive intervals of $s_1(t)$ and $\overline{s_1}(t)$ (consider that they cancel for every frequency value except in $|\omega| = \omega_b$) . The Hilbert transform of the product $s_a\,(t) \cdot y(t)$ and $s_b\,(t) \cdot y(t)$ becomes:

$$H[\,s_a\,(t) \cdot y(t)] = H[\,s_a\,(t) \cdot s_1\,(t)] + H[\,s_a\,(t) \cdot \overline{s_1}(t)]$$
$$H[\,s_b\,(t) \cdot y(t)] = H[\,s_b\,(t) \cdot s_1\,(t)] + H[\,s_b\,(t) \cdot \overline{s_1}(t)] \tag{3.26}$$

Using the Bedrosian identity, which states that the product of a low-frequency signal $s_{lf}\,(t)$ and a high-frequency signal $s_{hf}\,(t)$ with a non-overlapping spectrum is given by:

$$H\left[s_{lf}\,(t) \cdot s_{hf}\,(t)\right] = s_{lf}\,(t) \cdot H\left[s_{hf}\,(t)\right] \tag{3.27}$$

Therefore

$$H[\,s_a\,(t) \cdot y(t)] = s_1\,(t) \cdot H[\,s_a\,(t)] + s_a\,(t) \cdot H[\,\overline{s_1}(t)]$$
$$H[\,s_b\,(t) \cdot y(t)] = s_1\,(t) \cdot H[\,s_b\,(t)] + s_b\,(t) \cdot H[\,\overline{s_1}(t)] \tag{3.28}$$

These two equations represent a system of two equations in two unknowns $s_1\,(t)$ and $H[\,\overline{s_1}(t)]$, calculable thanks to the following relations:

$$s_1(t) = \frac{s_b(t) \cdot H[s_a(t) \cdot y(t)] - s_a(t) \cdot H[s_b(t) \cdot y(t)]}{s_b(t) \cdot H[s_a(t)] - s_a(t) \cdot H[s_b(t)]}$$

$$H[\overline{s_1}(t)] = \frac{H[s_a(t)] \cdot H[s_b(t) \cdot y(t)] - H[s_b(t)] \cdot H[s_a(t) \cdot y(t)]}{s_b(t) \cdot H[s_a(t)] - s_a(t) \cdot H[s_b(t)]} \quad (3.29)$$

Since:

$$s_b(t) \cdot H[s_a(t)] - s_a(t) \cdot H[s_b(t)] = 1$$
$$H[s_a(t)] = \sin(\omega_b t) \quad (3.30)$$
$$H[s_b(t)] = -\cos(\omega_b t)$$

The above equations can be rewritten as:

$$s_1(t) = \sin(\omega_b t) \cdot H[y(t) \cdot \cos(\omega_b t)] - \cos(\omega_b t) \cdot H[y(t) \cdot \sin(\omega_b t)]$$
$$H[\overline{s_1}(t)] = \sin(\omega_b t) \cdot H[y(t) \cdot \sin(\omega_b t)] + \cos(\omega_b t) \cdot H[y(t) \cdot \cos(\omega_b t)] \quad (3.31)$$

The terms $\overline{s_1}(t)$ and $H[s_1(t)]$ can be directly obtained from the following relations:

$$\overline{s_1}(t) = y(t) - s_1(t)$$
$$H[s_1(t)] = H[y(t)] - H[\overline{s_1}(t)] \quad (3.32)$$

The decomposition now demonstrated for ω_b is generalizable, applying m-1 times the bisection process with respect to bisector angular frequencies $\omega_{b_i} \in [\omega_{b_1}, \omega_{b_{m-1}}]$. Therefore, the following relationships will apply:

$$y(t) = s_1(t) - \overline{s_1}(t) = s_2(t) - \overline{s_2}(t) = \cdots = s_{m-1}(t) - \overline{s}_{m-1}(t)$$
$$s_i(t) = \sin(\omega_{b_i} t)\, H[y(t) \cos(\omega_{b_i} t)] - \cos(\omega_{b_i} t)\, H[y(t) \cos(\omega_{b_i} t)] \quad (3.33)$$
$$y_i{}^d(t) = s_i(t) - s_{i-1}(t)\ , \dots ,\ y_m{}^d(t) = y(t) - s_{m-1}(t)$$
$$with\ \ s_0(t) = 0\ \ with\ i = 1,2, \dots, m-1$$

Identification of bisector frequencies

In order to obtain the signals $y_i{}^d(t)$ to which only one frequency is associated, that is, the single-component signals, the decomposition method seen in the previous paragraph is used [28]. However, it remains to be established the method by which to obtain the value of bisector angular frequencies, calculated as an average of the frequencies of mono-component signals. To achieve this, the signal analysis methodologies typically used are:

- L_p – norm Periodogram;
- Discrete Fourier Transform (DFT).

Both methodologies are able to identify the frequencies of the mono-component signals even if they are very close to each other on the frequency axis.

L_p – norm Periodogram

Direct extension of the Laplace periodogram (p=1) and the ordinary periodogram (p=2), the periodogram L_p is defined as follows:

$$P(\omega) = \frac{1}{n}\left|\sum_{t=1}^{n} y_t \cdot e^{-jt\omega}\right|^p \quad with \quad p \in \{1\,,2\}$$

$$P(\omega) = \frac{n}{4}\|\beta_n(\omega)\|^2 \tag{3.34}$$

$$\beta_n(\omega) = arg \min_{\beta \in R^2} \sum_{t=1}^{n} |y_t - c_t{}^T(\omega)\beta\,|^p$$

It basically consists in minimizing the norm by the method of least squares, through the trigonometric regressor $c_t = [\cos(\omega t)\,, \sin(\omega t)]^T$. Once calculated $\beta_n(\omega)$ containing the coefficients representative of the amplitude of the cosine and sine component as ω varies, it is possible to obtain the graphic representation of the periodogram. The recommended choice of p in the literature is p=1.5. It turns out to be an excellent compromise between the **robustness** to noise of the Laplace periodogram (p=1) and the **efficiency** against spectral dispersion of the ordinary periodogram (p=2).

Discrete Fourier Transform

Discrete Fourier Transform (DFT) is a particular type of Fourier transform. Unlike the continuous Fourier transform, the DFT requires at input a discrete function whose values are generally complex and have a limited duration. For an acquired signal of N points:

$$V_k = \sum_{n=0}^{N-1} v_n e^{-j(\frac{2\pi}{N})kn} \quad with \quad k = 0{,}1, \dots\ , N-1 \tag{3.35}$$

At the base of these uses there is the possibility of efficiently calculating the DFT using the algorithms for the Fast Fourier

Transform (FFT).
The signal v_n is obtained from a discrete (unfinished) signal x_n through multiplication by a **rectangular window**. Thanks to the Fourier transform, the ordinary product becomes a convolution product:

$$\begin{cases} v_n = w_n \cdot x_n \\ \mathrm{V}(\omega) = \dfrac{1}{2\pi}\displaystyle\int_{-\pi}^{+\pi} \mathrm{X}(\omega) \cdot \mathrm{W}(\omega - \theta) d\theta \\ w_n{}^{Rett} = \begin{cases} 1, & 0 \leq n < N \\ 0, & 0 > n \geq N \end{cases} \end{cases} \tag{3.36}$$

There are different types of windows that can be used in the DFT, each with different characteristics but with the common intent to solve two fundamental problems:

- Scallop Loss;
- Spectral Leakage.

The goal is to accurately identify the bisector angular frequencies and to do so it is necessary to identify, through a maximum-finding algorithm, the frequency values to which the local maxima of $|\mathrm{V}(\omega)|$ are associated. For this purpose, the classic rectangular window will be used (Figure 3.5). The rectangular window, unlike other types of window, ensures the lower width of the main lobe, which translates into greater precision of frequency estimation; it also offers the greatest robustness against noise. Since in the specific case of inter-area oscillations we cannot guarantee synchronous sampling conditions (being non-periodic phenomena and not knowing their period) it is not possible to eliminate the so-called "sidelobes". Compared to the other windows, the rectangular window loses in terms of spectral leakage (related to sidelobes), but the error on the estimation of the frequency is poorly affected, instead it is particularly affected by the problem of scallop loss (linked to the amplitude of the main lobe).

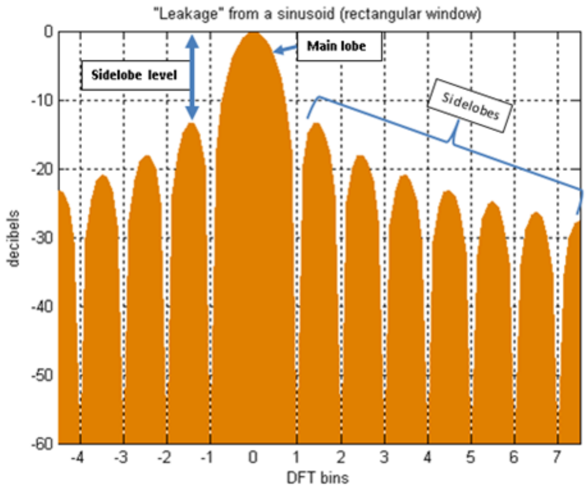

Figure 3.5 Rectangular window

3.1.4 Parameter Estimation

N.L.S. Classic Approach

Downstream of the separation of the signal in its components ${y_i}^d(t)$ provided by the PMU, it is necessary to estimate the parameters of the electromechanical oscillations. For this purpose, a non-linear quadratic minimization method, named Non-linear Least Squares (N.L.S.) is used [29]. Minimization occurs after taking as a basic form of regression:

$$ {y_i}^d(t) \cong A_i e^{\sigma_i t} sin(\omega_i t + \varphi_i) \tag{3.37} $$

- A_i= amplitude of the i-th oscillation;
- σ_i= damping of the i-th oscillation;
- ω_i= angular frequency of the i-th oscillation;
- φ_i= phase of the i-th oscillation.

The terms described above represent the unknowns of the minimization problem. The type of N.L.S. approach considered is the Variable Projection method (Var.Pro).

Var.Pro

The starting point of the proposed regression method is the reformulation of ${y_i}^d(t)$ in the form:

$$ \begin{gathered} {y_i}^d(t) = A_i e^{\sigma_i t} sin(\omega_i t + \varphi_i) = \\ = A_i e^{\sigma_i t} \sin(2\pi f_i t) \cos(\varphi_i) + A_i e^{\sigma_i t} \cos(2\pi f_i t) \sin(\varphi_i) = \\ = C_{1i} e^{\sigma_i t} \sin(2\pi f_i t) + C_{2i} e^{\sigma_i t} \cos(2\pi f_i t) \end{gathered} \tag{3.38} $$

The peculiarity of the Var.Pro method is to carry out the nonlinear regression only with respect to the parameters σ_i and f_i, the remaining parameters C_{1i} and C_{2i} are estimated through a linear regression, without any need for initial estimates.
The structure of the objective function is as follows:

$$\begin{aligned} L_i(\alpha_i, \beta_i) &= \sum_{j=1}^{h} \left[{y_i}^d(t_j) - \theta_i(\beta_i, t_j)\alpha_i \right]^2 = \\ &= [{y_i}^d - \theta_i(\beta_i)\alpha_i]^T \cdot [{y_i}^d - \theta_i(\beta_i)\alpha_i] = \\ &= \left\| [{y_i}^d - \theta_i(\beta_i)\alpha_i] \right\|^2 \end{aligned} \tag{3.39}$$

- $\alpha_i = [C_{1i}\ C_{2i}]$ vector of linear parameters;
- $\beta_i = [\sigma_i, f_i]$ vector of nonlinear parameters;
- $\theta_i = \theta_i\ (\beta_i, t_j)$ non-linear regressor;
- h number of samples.

Minimization can then be reformulated as:

$$L_i\left(\widehat{\alpha_i}, \widehat{\beta_i}\right) = \min_{\beta_i}\left\{ \left\| \min_{\alpha_i}\{ {y_i}^d - \theta_i(\beta_i)\alpha_i \} \right\|^2 \right\} \tag{3.40}$$

It is easy to see that if the value of β_i is fixed, the internal minimization becomes a linear regression problem. It follows that the minimum of linear parameters is:

$$\widehat{\alpha_i}\,(\beta_i) = {\theta_i}^+(\beta_i){y_i}^d \tag{3.41}$$

where ${\theta_i}^+$ is the pseudo-inverse matrix of $\theta_i(\beta_i)$.
Substituting the result obtained in the objective function we get:

$$L_i\left(\widehat{\alpha_i}, \widehat{\beta_i}\right) = \min_{\beta_i}\left\{ \left\| \min_{\alpha_i}\{ {y_i}^d - \theta_i(\beta_i) \cdot {\theta_i}^+(\beta_i){y_i}^d \} \right\|^2 \right\} \tag{3.42}$$

The minimization is now function only by the parameter β_i, calculable through an iterative process, allowing then to derive the value of

$$\widehat{\alpha_i}\,(\beta_i) = {\theta_i}^+(\beta_i){y_i}^d \tag{3.43}$$

Finally, to trace the value of A_i and φ_i it will be sufficient to apply the following relations:

$$A_i = \sqrt{{C_{1i}}^2 + {C_{2i}}^2}$$
$$\varphi_i = tg^{-1}\left(\frac{C_{2i}}{C_{1i}}\right) \tag{3.44}$$

3.2 Kalman Filter

An important mathematical tool able to extrapolate the characteristics of interest of the signals, starting from the measurements obtained through the PMU, is the Kalman Filter (KF) [30].

The KF is essentially a predictive-corrective estimator made through a set of mathematical equations. The concept of *optimum* generally associated with this tool is related to its ability to minimize the covariance matrix associated with the state vector, the estimation of which is the objective of the analysis conducted. The term *filter* is associated with the estimator's ability to operate even in noisy conditions, i.e. with measurements affected by noise.

The Discrete Kalman Filter (DKF) solves the universal problem of estimating the state $x \in R^n$ of a discrete-time linear dynamical system characterized by the difference equation:

$$x_k = A\,x_{k-1} + B\,u_k + w_{k-1} \tag{3.45}$$

with the measure $z_k \in R^m$ linked to the state by the relationship:

$$z_k = H\,x_k + v_k \tag{3.46}$$

The random terms w and v represent process and measurement noise, respectively. It is assumed that they are unrelated, white and characterized by a zero-centered normal probability distribution function:

$$p(w) \sim N(0, Q)$$
$$p(v) \sim N(0, R) \tag{3.47}$$

The process noise (Q) and measurement (R) covariance matrices may vary at each step, but for simplicity it is assumed that they are constant.

The KF thus behaves as a control system with output feedback, i.e., for each instant of sampling, the prediction (or first estimation) of the state is then readily corrected due to the feedback provided by the measured sample, thus obtaining a later estimate.

The equations that make up the Kalman filter are then divided into two groups:

- predictive (or time update)
- corrective (or measure update)

The first are then responsible for projecting the state vector and covariance matrix forward in time; the second implement a correction of the predicted parameters through knowledge of the measured sample [31].

- A simplified diagram of the recursive action of the Kalman Filter is shown in Figure 3.6. Where:
- $\hat{x}_k{}^-$ is the prediction of the state at the k-th step
- $P_k{}^-$ is the prediction of the covariance matrix at the k-th step
- K_k is the gain of the filter at the k-th step
- $\hat{x}_k$ is the estimated state at the k-th step
- P_k is the matrix of covariances estimated at the k-th step.

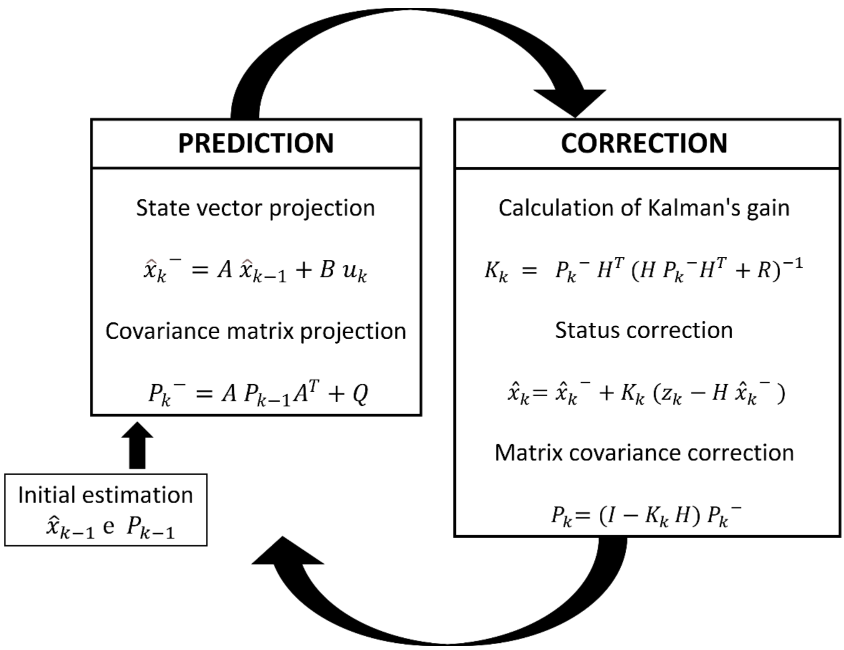

Figure 3.6 Simplified Kalman Filter scheme

3.2.1 Extended Kalman Filter

The DKF introduced above solves the problem of estimating the state of discrete-time processes described by a linear difference equation.
However, most of the problems for which an estimate of the state vector is required are characterized by the nonlinearity of the equations of state and measurement:

$$x_k = f(x_{k-1}, u_k, w_{k-1})$$
$$z_k = h(x_k, v_k) \tag{3.48}$$

The Kalman filter that linearizes the functions f and h around the expected value of the state vector and its covariance matrix is called the Extended Kalman Filter (EKF) [32].
It is important to note that the main defect of the EKF, resulting from the model linearization, is the alteration of the probability distribution of the random variable to be measured. Another consideration of fundamental importance is the voluntary omission of random process and measurement noises during the prediction phase:

$$\tilde{x}_k = f(x_{k-1}, u_k, 0)$$
$$\tilde{z}_k = h(x_k, 0) \tag{3.49}$$

The linearized model on which the EKF is based is:

$$x_k = \tilde{x}_k + A(x_{k-1} - \hat{x}_{k-1}) + W w_{k-1}$$
$$z_k = \tilde{z}_k + H(x_k - \tilde{x}_k) + V v_{k-1} \tag{3.50}$$

Where:

- x_k and z_k are the state and measure values;
- $\tilde{x}_k$ and $\tilde{z}_k$ are the approximate values of state and measure around which linearization occurs;
- $\hat{x}_k$ is the later estimate of the state;
- w_k and are the process and measurement noisesv_k;
- A is the Jacobian matrix obtained from the partial derivatives of f with respect to the *state x* and calculated at the point $(\hat{x}_{k-1}, u_k, 0)$;
- W is the Jacobian matrix obtained from the partial derivatives of f with respect to noise w and calculated at the point $(\hat{x}_{k-1}, u_k, 0)$;
- H is the Jacobian matrix obtained from the partial derivatives of h with respect to the *state x* and calculated at the point $(\tilde{x}_k, 0)$;
- V is the Jacobian matrix obtained from the partial derivatives of h with respect to noise v and calculated at the point $(\tilde{x}_k, 0)$.

It should be noted that the matrices A, H, W, V can vary at each step k, although these are not marked with the subscript k [33].
Like the DKF, the EKF also has two sets of equations well represented in Figure 3.7.

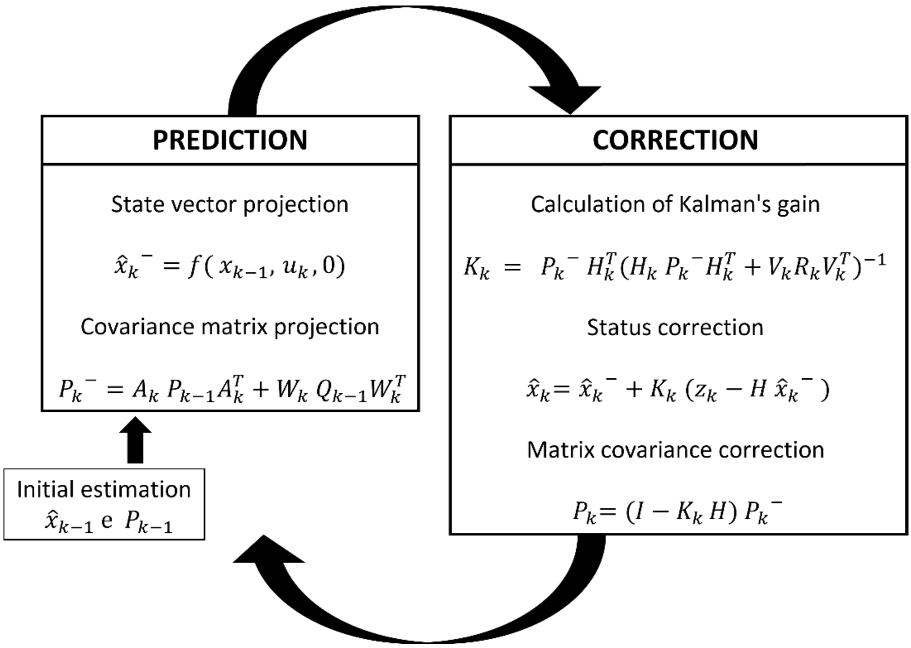

Figure 3.7 Simplified Extended Kalman Filter scheme

3.2.2 Unscented Kalman Filter

The EKF is probably the most widely used estimator for nonlinear systems. Nevertheless, over the years it has been observed a difficulty of calibration and a lower reliability for applications on systems not sufficiently linear in the Δt range of sampling. In order to overcome these limitations, the *Unscented Transform* was developed, which allows the propagation of information on media and covariance through a nonlinear transformation [34]. Such a transformation is more accurate, easier to implement (does not require Jacobian calculation) and computationally heavy as EKF [35].

The Unscented Transformation is based on the idea that "it is easier to approximate a probability distribution function than to approximate a nonlinear function or transformation". The strategy pursued is shown in Figure 3.8.

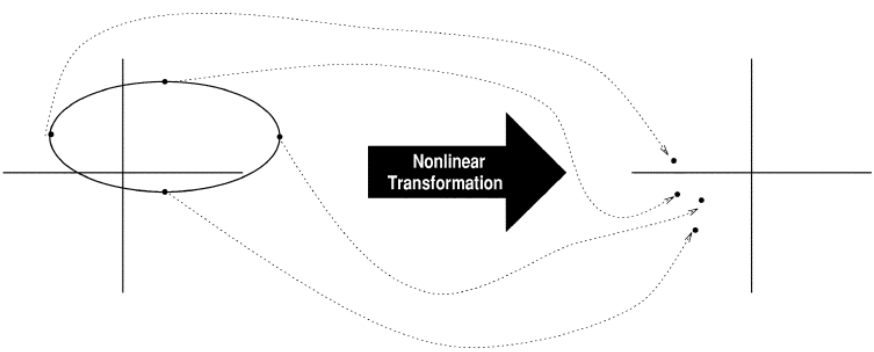

Figure 3.8 Unscented Transformation

A set of points, called *sigma points*, is chosen, known average $\bar{x}$ and covariance P_x of the input probability distribution function, so that its mean and covariance coincide with the latter. A group of sigma points S consists of a set of n state vectors and their weights:

$$S = \{i = 0, 1, \dots, p : X^{(i)}, W^{(i)}\} \tag{3.51}$$

The $W^{(i)}$ weights can be both positive and negative but, in order to guarantee an estimate free from conditioning, the relationship must be respected:

$$\sum_{i=0}^{p} W^{(i)} = 1 \tag{3.52}$$

Assigned S, the output of the system is obtained as follows.

1) Transformation of sigma points:

$$Y^{(i)} = h\left(X^{(i)}\right) \tag{3.53}$$

2) Output prediction:

$$\bar{y} = \sum_{i=0}^{p} W^{(i)} Y^{(i)} \tag{3.54}$$

3) Calculation of the output covariance:

$$P_y = \sum_{i=0}^{p} W^{(i)} \left(\bar{y} - Y^{(i)}\right) \left(\bar{y} - Y^{(i)}\right)^T \tag{3.55}$$

In most cases, a number of sigma points p equal to $2N_x + 1$, is chosen, having indicated with N_x the size of the state vector. The distribution of sigma points can be obtained from the following relations:

$$X^{(0)} = \bar{x}$$
$$W^{(0)} = W^{(0)}$$
$$X^{(i)} = \bar{x} + \left(\sqrt{\frac{N_x\, P_x}{1 - W^{(0)}}}\right)_i$$
$$W^{(i)} = \frac{1 - W^{(0)}}{2N_x} \tag{3.56}$$
$$X^{(i+N_x)} = \bar{x} - \left(\sqrt{\frac{N_x\, P_x}{1 - W^{(0)}}}\right)_i$$
$$W^{(i+N_x)} = \frac{1 - W^{(0)}}{2N_x}$$

Where the term $\left(\sqrt{\frac{N_x\, P_x}{1-W^{(0)}}}\right)_i$ represents the i-th row/column of the matrix expressed in round brackets.[1]
The only degree of freedom available in such a system of equations is the weight $W^{(0)}$ associated with the sigma point coinciding with the expected value of the imposed distribution.
The choice of $W^{(0)}$ affects the position of the other points with respect to the point $\bar{x}$:

- If $W^{(0)} > 0$ the dots tend to move away from the origin $\bar{x}$;
- If $W^{(0)} \leq 0$ the dots tend to approach the origin $\bar{x}$.

The set of UKF equations is summarized below.

Prediction

- Calculation of Sigma Points and their weights:

$$S = \{i = 0, 1, \ldots, p : \; X^{(i)}, W^{(i)}\} \tag{3.57}$$

- Projection of sigma points:

$$\hat{X}_{a,k} = f(X_{a,k-1}^{(i)},\, u_k) \tag{3.58}$$

[1] If the matrix A square root of P is in the form $P = AA^T$ then the sigma points are obtained from the lines of A. Otherwise, if $P = A^T A$, columns are used.

- Prediction of the state vector:

$$\hat{x}_{a,k}^{-} = \sum_{i=0}^{p} W^{(i)} X_{a,k}^{(i)} \tag{3.59}$$

- Projection of the covariance matrix:

$$P_{a,k}^{-} = \sum_{i=0}^{p} W^{(i)} (X_{a,k}^{(i)} - \hat{x}_{a,k}^{-})(X_{a,k}^{(i)} - \hat{x}_{a,k}^{-})^{T} \tag{3.60}$$

- Transformation of sigma points:

$$Y^{(i)} = h\left(X_{a,k}^{(i)}, u_k\right) \tag{3.61}$$

- Output prediction:

$$\hat{y}_k = \sum_{i=0}^{p} W^{(i)} Y_k^{(i)} \tag{3.62}$$

- Calculation of the output covariance:

$$P_{y,k} = \sum_{i=0}^{p} W^{(i)} \left(\hat{y}_k - Y_k^{(i)}\right) \left(\hat{y}_k - Y_k^{(i)}\right)^{T} \tag{3.63}$$

- Calculation of the state-exit covariance matrix:

$$P_{xy,k} = \sum_{i=0}^{p} W^{(i)} \left(\hat{y}_k - Y_k^{(i)}\right) \left(\hat{x}_k^{-} - X_k^{(i)}\right)^{T} \tag{3.64}$$

Correction

- Calculation of filter gain

$$K_k = P_{xy,k} \, P_{y,k}^{-1} \tag{3.65}$$

- Updating the Status Vector

$$\hat{x}_k = \hat{x}_{a,k}^{-} + K_k \,(z_k - \hat{y}_k) \tag{3.66}$$

- Reduced covariance matrix update (to state only)

$$P_k = P_k^- - K_k P_{y,k} K_k^T \tag{3.67}$$

3.3 Heuristic Approach

A *Heuristic Approach* means a problem-solving process based on mere intuition and disregarding scientific rigor.
In order to comply with the aforementioned requests, i.e. to estimate the modal parameters of the oscillations manifested on the electricity grid, the heuristic algorithms analyzed and tested are as follows:

- Genetic Algorithm (GA);
- Particle Swarm Optimization (PSO).

3.3.1 Genetic Algorithm

Genetic Algorithms (GA) are complex, adaptive procedures, aimed at solving research and optimization problems and conceptually based on the principles that regulate the natural evolution of species [36]. The idea behind the GAs is therefore to select the best solutions and to recombine them in some way with each other in such a way that they evolve towards a point of optimum. In the language of GA the function to be maximized is called fitness F. Suppose that the fitness function depends on n variables:

$$F = f\,(x_1, x_2, \dots, x_n) \tag{3.68}$$

A set of n values $x_1, x_2, \dots, x_n$ belonging to a certain range is called *individual* (or solution). A set of individuals forms a *population.* A solution can be coded biunivocally in binary code. The specific sequence (string) of 0 and 1 that make up an individual (solution) is called *chromosome*. Considering that we are in the presence of a temporal evolution of the population, we speak of *generation* to indicate the population in a given instant of time.
In nature, individuals reproduce by mixing in this way their genetic heritage, that is, their chromosomes: the new individuals generated will therefore have a genetic heritage derived partly from the father and partly from the mother. Natural selection (i.e. the reuse of good solutions) ensures that only the strongest, "most suitable" individuals are able to survive and therefore reproduce, that is, those with the highest fitness (closer to the optimum); the average fitness of the population will therefore tend to increase with the generations, thus leading the species to evolve over time.

GA Structure

1) Defining the initial build

Define (even at random) a first set of possible solutions to the considered problem. Each genome is identified by a string of bits.

2) Evaluation of each solution and selection of the best

Evaluate all possible solutions, associating each one with a quality (or fitness) indicator so that it can be ordered.

3) Defining a New Generation

Define a new group of solutions by appropriately modifying the solutions with high quality, so as to favor development at the expense of the worst ones.

4) Conclusion of processing

If the number of iterations established has been reached or the quality of the best available solution is acceptable (above a tolerance threshold) processing can be terminated, otherwise return to step 2 to define a new set of solutions.

Selection

The selection of an individual depends on his fitness value (i.e. how "good" the individual is at solving the problem): a higher fitness value corresponds to a greater chance of being chosen as parent to create the new generation. One of the most used criteria is that of Holland who attributes a probability of choice proportional to fitness. Thanks to the mechanism of selection, only the best individuals have the opportunity to reproduce and then pass on their genome to subsequent generations.

Crossover and Mutation

For the creation of new individuals at each generation, two operations inspired by biological evolutionism are used: *crossover* and *mutation.* Once a pair of parents with the selection mechanism has been identified, their genomes can undergo each of the two operations:

- Crossover: given two strings, a point is identified that separates each of them into two parts; the head of the first string combines with the tail of the second and vice versa.
- Mutation: inversion of one or more bits that make up the string (from 1 to 0 and vice versa).

3.3.2 Particle Swarm Optimization

The origin of this particular approach can be summarized by Figure 3.9 [37]. It is not a graph or a formula, but a swarm of birds in flight that, moving according to a well-defined logic, is looking for a "global optimum", which could be translated into a safe place for winter or the food search [38].

Figure 3.9 Flock of birds in motion (principle behind PSO)

The characteristics of the flock, which can be of birds, ants or fish, are taken up in the fundamental concepts of Particle Swarm Optimization (PSO).

The search for solutions to complex problems, such as the one treated in this work, is based on "particles" (individual elements of the flock) that moving in the solution space, seek a solution very close to the optimal one by exploiting two fundamental principles [39]:

- *Exploration:* the particles explore the decisive space in search of what is the optimal solution; once they find the best position at that moment they keep memory of it, continuing their exploration. Only at the end of the exploration process will the particles return to what has been their "best place".
- *Exploitation:* Particles exchange their knowledge to help each other find the best place to position themselves.

It is now understandable how PSO can be defined as bio-inspired, that is, inspired by the world of biology.

The *population-based* approach, on which the PSO is based, is characterized by individual elements (particles) that seek excellent solutions within a space [40]. The most interesting aspect of PSO is the interaction between particles, a kind of "dialogue" where each particle shares its results and at the same time constantly obtains information from the rest of the swarm. Precisely the interaction between these particles produces a result close to optimal, as individually they are not able to deal with the problem. To better facilitate the search for solutions in the eligible region, it is correct to assume that the particles should not be placed in a single point, as they would risk producing results that are too similar to each other, neglecting other unexplored areas with a certain probability. Therefore the initial placement of the particles occurs randomly in the space of solutions, called D. Each individual particle i is characterized in iteration t by:

- a position $x_i^t \in R^n$;

- speed v_i^t, at which the particle explores the space of solutions;
- a fitness function ($f: S \rightarrow R \; with \; S \subseteq R^n$) that represents a quality index associated with the particle;
- p_i^t represents the memory of the particles, that is, the best position assumed until the instant t (personal best) by the i-th individual.

In addition to the p_i^t, representing a local optimum, at the moment t is defined the best position assumed, up to that moment, by the entire group of particles g^t *(global best)*. This parameter, unlike the personal best, therefore arises from the communication between the different units that make up the swarm, and therefore represents the position of absolute optimum at the generic instant t.
The initial position will therefore be the vector (x_i^0, v_i^0) with a certain fitness function (which can at most inform about its good initial positioning), while in p_i^t the fitness function it will be $p_{best,i}^t = f(p_i^t)$. Finally, the vector (g^t) that represents the best position of the entire group of particles is associated with a fitness function $g_{best}^t = f(g^t)$.

PSO Structure

The classic algorithm [41] is executed by iterating the following steps:

1) Random initialization of the particle population in terms of location and velocity.
2) Evaluation of the fitness function associated with each particle.
3) Compare the fitness function (step 2), with the function p_{best}^t. If the current value is better than p_{best}^t , arises $p_i^{t+1} = x_i^t$.
4) Identify the particle that has achieved the best fitness function, that is, the best positiong^t, and fix $g_{best}^t = f(g^t)$.
5) Update of position and speed according to the equations:[2]

$$\begin{gathered} v_i^{t+1} = w^t v_i^t + c_1 U_1^t \otimes \left(p_i^t - x_i^t\right) + c_2 U_2^t \otimes (g^t - x_i^t) \\ x_i^{t+1} = x_i^t + v_i^{t+1} \end{gathered} \qquad (3.69)$$

Where:

- w^t is the inertia of the particle to stabilize its velocity ($0 < w < 1.1$);
- $c_1 (self\ adjustment\ weight)\ and\ c_2 (social\ adjustment\ weight)$ are two positive constants imposed in the programming phase and particularly incidents on the performance of the algorithm;
- $U_1^t \; e \; U_2^t$ are two independently generated vectors for each particle, of similar size to x_i^t and composed of elements

[2] The symbol ⊗ indicates the element-by-element multiplication between two matrices or vectors of similar dimensions.

obtained from a uniform distribution function defined in the range [0;1] .[3]

6) If the stop condition is reached[4], the cycle ends and a solution is obtained, otherwise return to step 2.
   Particular attention should be paid to the term w (variant time). A larger inertia value produces a rapid increase in velocity and exploration over a larger region of state space. Conversely, a smaller value allows a smaller portion of space to be meticulously screened. In order for a "coarse" exploration of the state space to be allowed initially and, only subsequently, to proceed with a "fine" investigation on a reduced portion of space, a variant and decreasing time inertia must be provided at each iteration step [42]. Therefore, in order to guarantee this result, the only band belonging to w, i.e. the terms:
   - w^0 initial value of inertia;
   - $w^{t_{max}}$ final value of inertia.

The law by which inertia decreases linearly is:[5]

$$w^t = (w^0 - w^{t_{max}})\frac{(t_{max} - t)}{t_{max}} + w^{t_{max}} \tag{3.70}$$

3.4 Dynamic Mode Decomposition

Dynamic Mode Decomposition (DMD), is an emerging data-driven technique used to obtain reduced linear models for complex systems of large dimensions, extracting from a data matrix, coherent spatio-temporal structures that dominate the measurements of the dynamic system under consideration [43]. Originally introduced to the scientific community of fluid dynamics by Peter Schmid and later extended to generic nonlinear dynamical systems by Koopman's theory, the DMD algorithm is the subject of applications in different fields, such as neuroscience, video processing, robotics, finance, social media and more. Its adaptability is due to the fact of disregarding the equations that govern the system under consideration, if there is a huge availability of data, of measures of the system itself [44].
Consider a dynamic system that evolves over time, for example a signal or fluid distributed in a two-dimensional space that changes its

[3] These "random" terms allow to avoid stalling at local minimum points of the fitness function.

[4] Different shutdown conditions can be imposed: maximum number of iterations; maximum tolerance; maximum number of iterations for which the fitness function is below a threshold value.

[5] In literature are presented other methods that allow to obtain a reduction of inertia with each iteration.

shape over time. Suppose that the mathematical dynamic model describing its evolution over time is unknown. Proceed as schematically shown in Figure 3.10.

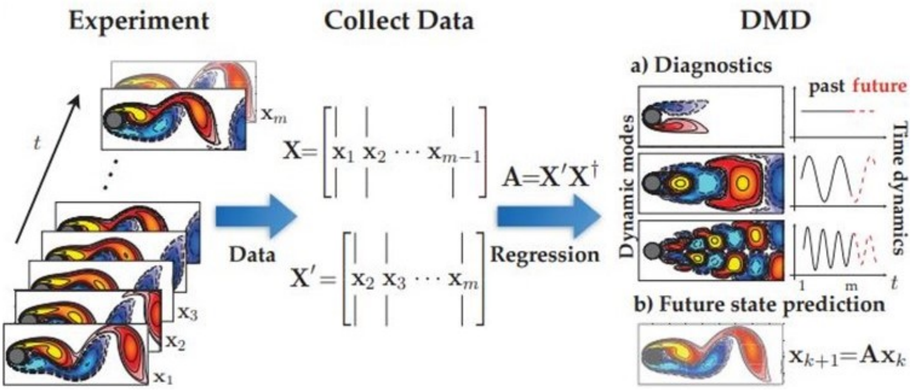

Figure 3.10 Conceptual scheme of DMD algorithm

1) **Data collection**: take snapshots of the system for each time interval (which is the sampling period Δt) and for each generic instant t the spatial distribution of the system, the state of the system, is had.

2) **Data reorganization:** The data is organized into two matrices. Each state of the system at the instant t_k is reshaped as a column vector, and as time increases, after each Δt, the subsequent columns of the matrix are filled. Imagining to sample up to the instant t_m, the first matrix X will be formed by the samples for $k = (1,2,3, \ldots, m - 1)$, while the second matrix X' will be identical to the first but translated by a later time interval with the samples for $k = (2,3,4, \ldots, m)$:

$$X = \begin{pmatrix} | & | & | & | \\ \boldsymbol{x}_1 & \boldsymbol{x}_2 & \ldots & \boldsymbol{x}_{m-1} \\ | & | & | & | \end{pmatrix}; X' = \begin{pmatrix} | & | & | & | \\ \boldsymbol{x}_2 & \boldsymbol{x}_2 & \ldots & \boldsymbol{x}_m \\ | & | & | & | \end{pmatrix} \quad (3.71)$$

3) **Application of DMD:** DMD aims to estimate the best linear operator that can transform X into X'. So, the basic hypothesis is to describe the system under consideration with a linear time-invariant model, which has a matrix structure of the type:

$$X' \cong AX \quad (3.72)$$

That is, each element of the matrix X' is bound to that of the matrix X by the following equation:

$$\boldsymbol{x}_{k+1} = A(\boldsymbol{x}_k) \tag{3.73}$$

Consequently, the solution that best approximates matrix A is given by:

$$A = X'X^{-1} \tag{3.74}$$

where X^{-1} representing the pseudo-inverse of X. This solution is capable of minimizing the error $||X' - A\mathbf{X}||^2$.

Ultimately, the goal of the DMD algorithm is to derive eigenvectors and eigenvalues of the matrix A to describe the mathematical model of the system, to predict its future state or possibly to control it.

3.4.1 Singular Value Decomposition

The X and X' data matrices usually have millions of elements in a column and/or row, they are characterized by a 'narrow and long' shape, having one of the two dimensions preponderant over the other. These are orders of magnitude that return an array A the size of $million\, x\, million$. From a computational point of view, it therefore becomes extremely complex to have to calculate the operator A, and also useless since the important information is contained in a reduced part of the matrix. Before proceeding to step 3 then, a decomposition to singular values is made: Singular Value Decomposition (SVD). The goal is to bring X and X' back to small matrices, of the order of thousands or hundreds of rows and/or columns, without losing information in terms of eigenvalues and eigenvectors [45].
Given a matrix X, real or complex, of dimension $n\, x\, m$ its decomposition to singular values is the representation of X as a product of three matrices, with particular characteristics:

$$X = U\Sigma V^T$$

$$\underset{(n\,x\,m)}{X} = \underset{(n\,x\,n)}{\begin{bmatrix} | & | & | \\ u_1 & .. & u_n \\ | & | & | \end{bmatrix}} \underset{(n\,x\,m)}{\begin{bmatrix} \sigma_1 & 0 & 0 \\ 0 & \dots & 0 \\ 0 & 0 & \sigma_m \end{bmatrix}} \underset{(m\,x\,m)}{\begin{bmatrix} | & | & | \\ v_1 & .. & v_m \\ | & | & | \end{bmatrix}^T} \tag{3.75}$$

These matrices enjoy the following properties:

- U and V are unitary matrices.[6] The column vectors of U are called left singular vectors, while those of V^T are called right

[6] A unit matrix is a complex square matrix that satisfies the condition: $UU^T = U^TU = I$, where I is the identity matrix.

singular vectors.

- Every left singular vector is of the same shape as the column vector of X, but with the particularity that the vectors $\underline{u}$ are eigenvalues arranged in hierarchical order. The vector $\underline{u_1}$ is in a sense more capable of describing the characteristics of the matrix X than the next vector $\underline{u_2}$. In addition, the U matrix is orthogonal and forms a basis.
- Σ is a diagonal matrix whose elements are called singular values of X. They are non-negative elements, and they are hierarchically ordered so that the amplitude decreases as the index increases. Is:

$$\sigma_1 \geq \sigma_2 \geq .. \geq \sigma_m \geq 0 \qquad (3.76)$$

- The vector v_1 is a representation of how the mode u_1 evolves over time. Each vector $\underline{x}$ consists of a certain amount of the mode $\underline{u_1}$ but how this mode varies in the considered time interval is described by the vector $\underline{v_1}$. It is important to note, however, that the SVD considers the transpose of V that is thus generated:

$$V^T = \begin{bmatrix} - & {v_1}^T & - \\ - & \dots & - \\ - & {v_m}^T & - \end{bmatrix} \qquad (3.77)$$

  The first column of V^T is an expression of the composition of modes u_k necessary to equal x_1, the second column informs us of the mixture of ways u_k necessary to describe x_2, and so on.
- It can be shown that the rank of the matrix X is equal to that of the matrix Σ. In particular, it is observed that the rank of Σ is just equal to the number of non-zero singular values.

These properties, in particular the consideration that the elements and vectors of the U, V and Σ matrices are ordered hierarchically, leads us to the fundamental result that the first vector $\underline{u}$, the first sigma element, and the first line $\underline{v}$, will be more important than the subsequent ones in terms of describing the starting matrix X. It means that the information contained in the first elements is more descriptive of the matrix X, and they already manage to give us a good approximation of the matrix X itself, without having large dimensions in terms of rows and columns. Most often, significantly non-zero singular values are concentrated in a small submatrix of Σ, and then the other elements can be discarded without losing information.

3.4.2 Matrix Truncation

The above considerations suggest that it is possible to reduce the X matrix to an approximation of it, but to understand quantitatively what it consists of and what term to stop at, we must focus our attention on the matrix Σ and its rank. The rank of the Σ matrix is shown to be equal to that of the starting matrix but since this matrix consists of singular values, gradually decreasing, it can be truncated to a lower rank, which can be arbitrarily chosen based on the number of information of interest. To better understand this concept, it is useful to propose an example described by Steven Brunton and Nathan Kutz in the book "*Data-Driven Science and Engineering*" [46]. By importing a photo into MATLAB, and applying the singular value decomposition, it is possible to visually notice how the approximate matrix is able to well represent the starting matrix and how convincing results are achieved even with a truncation of the relevant rank. In the example shown, a photo of a dog is considered, report it in black and white to make it a two-dimensional matrix, and apply its SVD on MATLAB using the simple command:
[U,S,V] = svd(X) (The matrix Σ on MATLAB is denoted by letter S).
The dimensions of the matrices considered are:

$$\underset{(2000\ x\ 1500)}{X} = \underset{(2000\ x\ 2000)}{U}\ \underset{(2000\ x\ 1500)}{\Sigma}\ \underset{(1500\ x\ 1500)}{V^T} \tag{3.78}$$

To understand what happens intuitively, it is useful to see a numerical example. First of all, the matrix Σ is rectangular and diagonal, which means that outside the diagonal there are all null elements and that it can in the very first analysis always be reduced to its square shape by eliminating all excess zeros (in this case, 500 elements can be eliminated). In addition, the difference between the first two elements is remarkable, as Figure 3.11 shows: the first is an order of magnitude greater than the second. It is clear, therefore, that choosing a lower rank allows us to work with a few singular but preponderant values.

S

2000x1500 double

	1	2	3	4	5	6	7	8	9	10
1	3.0300e+05	0	0	0	0	0	0	0	0	
2	0	6.0138e+04	0	0	0	0	0	0	0	
3	0	0	4.6113e+04	0	0	0	0	0	0	
4	0	0	0	2.6157e+04	0	0	0	0	0	
5	0	0	0	0	2.1827e+04	0	0	0	0	
6	0	0	0	0	0	1.7336e+04	0	0	0	
7	0	0	0	0	0	0	1.5957e+04	0	0	
8	0	0	0	0	0	0	0	1.5504e+04	0	
9	0	0	0	0	0	0	0	0	1.2415e+04	
10	0	0	0	0	0	0	0	0	0	1.1864e
11	0	0	0	0	0	0	0	0	0	

Figure 3.11 Example of an SVD S matrix

To impose the rank of the matrix S equal to 5 is to work with the following dimensions:

$$\underset{(2000\,x\,1500)}{X} \cong \underset{(2000\,x\,5)}{U} \quad \underset{(5\,x\,5)}{\Sigma} \quad \underset{(5\,x\,1500)}{V^T} \tag{3.79}$$

Figure 3.12 compare four different cases, with variable and increasing rank:

- **Rank = 5**. A satisfactory approximation is not reached even if a dog and its characteristic traits can be distinguished.
- **Rank = 20**. All the main information and sufficient clarity of the image are obtained, but some details are still unclear.
- **Rank = 100**. A more than satisfactory result is achieved. The image looks the same as the original. Note that rank equal to 100 means having reduced the number of singular values taken into account by 15:1.
- **Rank = 500**. Despite the increase in the singular values considered, there is no noticeable improvement compared to the previous case. Only by paying more attention, some differences can be noticed.

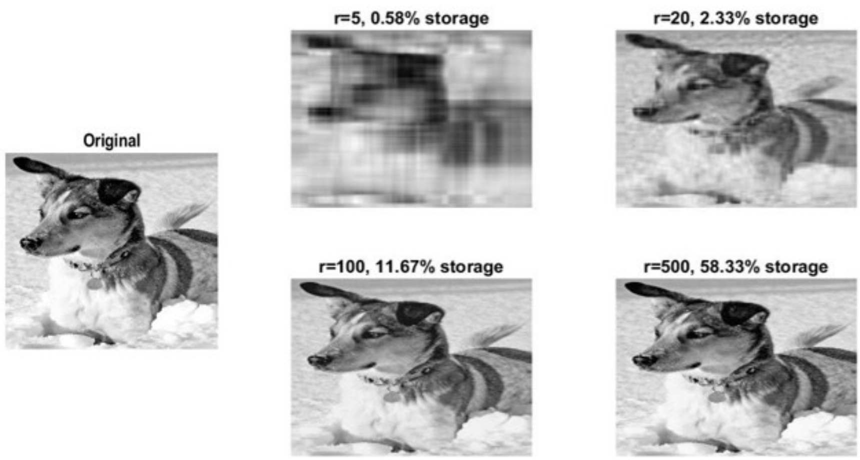

Figure 3.12 Approximation of the image, as the rank considered changes

Therefore, as an initial option, it is possible to choose an arbitrary and fixed number to be assigned to the rank of the sigma matrix, perhaps identified based on experimental evidence and through comparison of results. In this example, rank 100 can be chosen, which cuts the computational load sufficiently but is extremely like the input matrix. This is the *static rank*. If, on the other hand, a more precise statement is desired, the sum of all singular values can be considered and each element weighed in relation to the total, highlighting its contribution.

In the Figure 3.13 on the left are shown the orders of magnitude of each element constituting the diagonal, and the strong decrease is once again evident. On the right, however, the cumulative sum of the singular values is shown on a logarithmic scale, with respect to the total sum of the same. It can be seen that in this example about 90% of the energy is contained in the first 500 elements alone and how choosing rank = 100 means identifying about 70% of the energy.

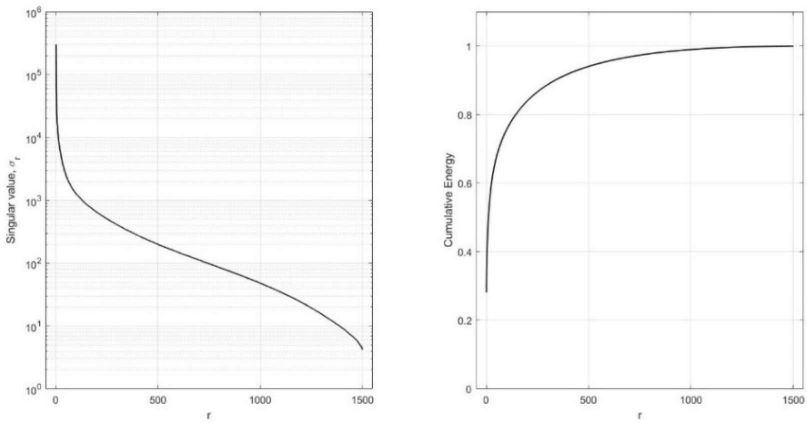

Figure 3.13 Evolution of singular values, and their cumulative sum on a logarithmic scale

It is therefore not difficult to guess that the algorithm itself can be asked to stop as soon as a sufficient energy threshold is reached, and to identify the rank at that threshold accordingly. This condition can be imposed through a simple *find* command that identifies the index of the element that first reaches, for example, 70% of the energy. This command was applied to the previous example and the figures demonstrate the consistency between the results obtained graphically and numerically. In fact, in Figure 3.14 it is shown how, according to the MATLAB find command, 0.756 of the energy is associated with the index element 100 on the diagonal, while the first singular value that reaches 0.90 of the energy is that of index 336. Graphically these values are confirmed in Figure 3.15. This is the *dynamic rank*.

```
Command Window
>> cdS = cumsum(diag(S))./sum(diag(S));
>> find(cdS>0.756, 1 )

ans =

   100

>> find(cdS>0.90, 1 )

ans =

   336

fx >>
```

Figure 3.14 Index detection of the required energy threshold via MATLAB command

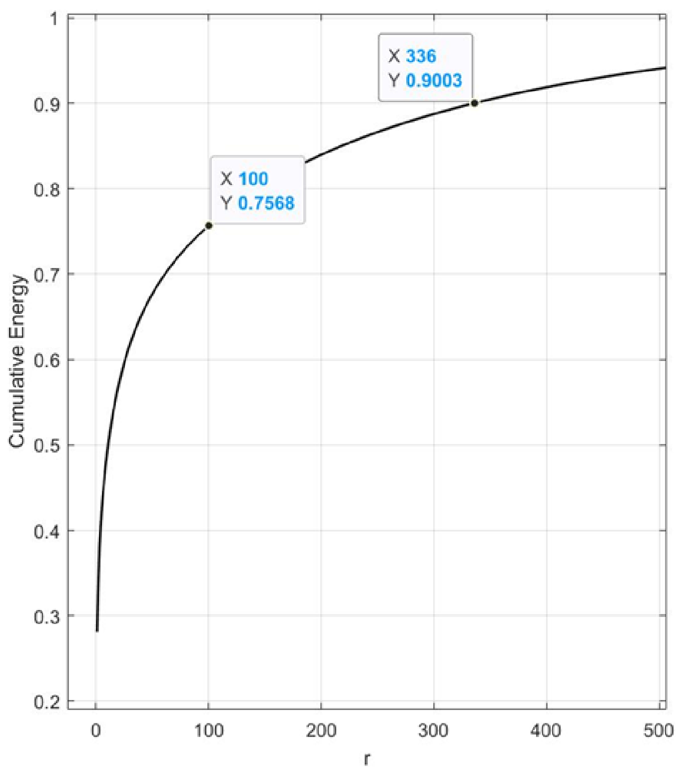

Figure 3.15 Index detection of the required energy threshold via graph

3.4.3 Static Order and Dynamic Order

Thanks to these considerations the DMD algorithm can be distinguish in two sub-cases: with static order or dynamic order. It is important to note the connection between the choice of the rank of the S-matrix of the SVD, and the choice of the order of the DMD algorithm. Reducing the sigma matrix to a matrix of n elements, whether they are identified by the static or dynamic rank, benefits not only in computational terms but allows to focus attention on the most relevant modes of the studied system, and therefore gives important information on the number of modes that DMD detects. The dynamic rank of the SVD corresponds to a dynamic order of the DMD, just as the static rank corresponds to a static order [47].

- *Static order:* a fixed value is arbitrarily chosen to which to truncate the size of the matrix, which may be between 2 and the size of the matrix itself. This will correspond to the same number of ways. It is necessary to have an even number of complex conjugate eigenvalues in order to reconstruct the oscillatory dynamics typical of the signals we will examine; reason why, minimum rank equal to 2 will be imposed and a condition to always choose it even. Obviously, the smaller the order, the better and faster the algorithm will perform, but the more information will be lost.
- *Dynamic order:* an energy threshold is chosen. With a condition on the cumulative sum, after reaching 90% of the energy, the matrix is chosen to be truncated and thus take that index as the order of the DMD. This leaves the algorithm with the task of identifying the preponderant modes that make up the system.

3.4.4 Algorithm Structure

To understand what is meant by ways of the system, and understand how they are found by the DMD algorithm, it is necessary to know the algorithm framework itself, or the mathematical steps that compose it [48]. Returning to its application, after the collection of data and their reorganization in the two input matrices X and X', the following steps are taken:

1) Singular value decomposition of the input data array X:

$$X \approx U\Sigma V^* \tag{3.80}$$

In this step, it is necessary to choose which order to refer to, whether to the static or the dynamic one and consequently choose which rank to cut the SVD matrices.

2) The matrix A could be obtained by the pseudo-inverse of X obtained

by SVD according to the formula:

$$A = X'V\Sigma^{-1}U^* \tag{3.81}$$

At the computational level it is more efficient to work on the matrix $\tilde{A}$, obtainable through *Proper Orthogonal Decomposition:*

$$\tilde{A} = UAU^* = U^*X'V\Sigma^{-1} \tag{3.82}$$

The matrix $\tilde{A}$ define a small-size linear model of the dynamic system:

$$\tilde{\boldsymbol{x}}_{k+1} = \tilde{A}\tilde{x}_k \tag{3.83}$$

3) The spectral decomposition of the matrix $\tilde{A}$ is calculated:

$$\tilde{A}W = W\Lambda \tag{3.84}$$

In which the columns of W represent the eigenvectors and $\boldsymbol{\Lambda}$ is a diagonal matrix that contains the corresponding eigenvalues λ_k.

4) Finally, it is possible to reconstruct the spectral decomposition of A starting from the knowledge of W and Λ. In particular, the eigenvalues of A are given by Λ, while the eigenvectors of A, defined *DMD modes,* or the searched modes, are given by the columns of the matrix Φ, obtainable as:

$$\Phi = X'V\Sigma^{-1}W \tag{3.85}$$

Obtained eigenvectors and eigenvalues of the matrix A, it is now possible to reconstruct the entire dynamics of the system, for any future state. Reporting in continuous time the eigenvalues

$$\omega_k = \frac{\ln(\lambda_k)}{\Delta t} \tag{3.86}$$

the solution approximated to the generic instant k is written as:

$$\boldsymbol{x}(t) \approx \sum_{k=1}^{n} \phi_k e^{(\omega_k t) b_k} = \boldsymbol{\Phi} \mathrm{e}^{(\boldsymbol{\Omega} t)\boldsymbol{b}} \tag{3.87}$$

Where b_k represents the initial amplitude of each mode, $\boldsymbol{\Phi}$ is the matrix whose columns correspond to the eigenvectors ϕ_k obtained by DMD and Ω is the diagonal matrix of the eigenvalues ω_k. As already discussed in the previous paragraph, it is possible to interpret the equation (3.87) as the best least squares approximation of the discrete-time dynamic system:

$$\boldsymbol{x}_{k+1} = A(\boldsymbol{x}_k) \tag{3.88}$$

The matrix A is reconstructed in such a way that at each sampling instant the error is minimized

$$||\boldsymbol{x}_{k+1} - A\mathbf{x}_\mathrm{k}||^2 \tag{3.89}$$

Finally, to derive the value of the coefficients b_k, the state vector $\boldsymbol{x}(0)$ must be considered at the initial instant $t = 0$. From equation (3.87) it is derived that:

$$\boldsymbol{x}(0) = \boldsymbol{\Phi}\mathbf{b} \tag{3.90}$$

From the pseudoinverse of $\boldsymbol{\Phi}$**,** the coefficients b_k can be derived:

$$\mathbf{b} = \boldsymbol{\Phi}^{\dagger}\boldsymbol{x}(0) \tag{3.91}$$

3.5 Tufts Kumaresan

The Tufts-Kumaresan method was first proposed in 1982 as an extension of well-known Prony's analysis to noise-corrupted signals [49,50]. A feature of the method is the display of the estimated results and the ability to easily distinguish between the modes associated with the noise or the signal itself, with the discriminating factor of falling inside or outside the unit circle in Gaussian space. In this research, however, this peculiarity will not be considered because for the proposed application it is more useful to display the results in a different way. As mentioned above, the purpose of the method is to obtain the parameters that characterize a signal, that is the parameters of frequency, amplitude, damping and phase. In fact, an oscillatory signal can be described mathematically as a sum of several modes:

$$x(t) = \sum_{i=1}^{M} A_i \mathrm{e}^{-\sigma_i \mathrm{t}} \sin(2\pi f_i t - \varphi_i) \tag{3.92}$$

Where M is the number of modes that make up the signal, A, σ, f, ϕ, are respectively the amplitude, damping, frequency and angle of the general mode i.
To achieve the goal, the Tufts-Kumaresan technique uses backward linear prediction, that is, it estimates the samples of a signal with a linear function of its subsequent samples; and uses the SVD to cut noise in the mass of processed measurements [51,52]. To explain this, consider now having N samples of a signal, such as the frequency measurements provided by WAMS, taken at different moments of time, each Δt. The method hypothesis is that the signal is a sum of dampened exponentials, which are modes M_s, ideally equal to M.

$$y(n) = \sum_{k=1}^{M_s} a_k e^{s_k n} \qquad n = 1, \dots . N \tag{3.93}$$

The samples are arranged in this way to construct the Hankel matrix A and the vector h, as follows:

$$A = \begin{bmatrix} y^*(1) & y^*(2) & .. & y^*(L) \\ y^*(2) & .. \quad .. & & .. \\ .. & .. \quad .. & & .. \\ y^*(N-L) & .. \quad .. & & y^*(N-1) \end{bmatrix} \quad h = \begin{bmatrix} y^*(0) \\ y^*(1) \\ .. \\ y^*(N-L-1) \end{bmatrix} \tag{3.94}$$

Where "*" indicates the complex conjugate values. N is the number of samples and L is a constant.
The linear approximation is carried out by the linear function defined as the polynomial prediction-error filter with order L.

$$B(z) = 1 + b(1)z^{-1} + \cdots . + b(L)z^{-L} \tag{3.95}$$

It is possible to impose the following equation that clarifies the concept of backward prediction:

$$Ab = -h \tag{3.96}$$

where b is the vector of the coefficients of the prediction-error filter. From this formula it is easy to determine the vector b with the inverse matrix operation which, as has been shown, minimizes the quadratic norm.
The method consists in finding the roots of the prediction-error filter; $B(z)$ will have zeros at e^{-s_k*} ; $k = 1,2, \dots L$. In the case of noise-free data and in the case of $L = M$ these zeros would be exactly the complex conjugate values of s_k, with a changed sign. From this it is easy to

determine the damping and frequency since $s_k = -\sigma_k \pm j2\pi f_k$ the parameters are taken from the imaginary and real part. To determine, instead, the amplitude and the phase it is necessary to go back in the equation (3.93). Once the terms $e^{s_k n}$ and the $y(n)$ are known, the only variables to be determined are the coefficients a_k. With the inverse equation it is therefore easy to estimate these values, whose absolute value and angle, will give the desired amplitude and phase.
The crucial point of the algorithm is to identify the right value of the constant L and here the SVD becomes relevant. Before calculating the vector b, the Hankel matrix A is processed by means of an SVD decomposition [53]. The matrix S, containing the singular values, is a diagonal matrix whose elements are non-negative values, placed in descending order. The most significant information about the system is somewhat concentrated in the highest part of the S matrix, so it is convenient to truncate the matrix to a lower rank that will be the order of the new Hankel matrix and the number of estimated modes. Operationally the steps are: starting from a hypothetical value of L, the first Hankel matrix is created; then the matrix is subjected to an SVD and then with the truncation of the matrix S to an acceptable value, normally chosen as a threshold on an estimated standard deviation of noise, a new constant M_s, less than L, is estimated, which is replaced as the new dimension of the Hankel matrix.
The discrimination between significant singular values and noisy components is obtained by calculating the average of the elements in the lower part of the matrix S, usually considering the elements whose index ranges from a percentage of L, called L_1, to L itself. In practice, it is possible to select the index of the first singular value greater than a threshold of this mean, such as a constant M_s, which is the number of modes that the algorithm intends to estimate.
After this stage, the Hankel matrix is reshaped, and the calculation of the parameters is carried out as explained above.

Chapter 4

4 Experimental Tests

In this chapter, the algorithms described in Chapter 3 are tested on both simulated signals and real data provided by Terna. The use of the latter necessarily involves a pre-processing step characterized by:

1. Fill missing of NaNs
2. Filtering for noise elimination
3. Detrending of the mean value.

The real data used in this chapter have already been pre-processed, so the steps listed above are not further described
In addition, all algorithms must be characterized by lower computation times of the processing window. In fact, the latter is chosen with reference to the monitoring application but normally not chosen greater than 30 s.

4.1 Hilbert Transform

4.1.1 Simulated tests

In order to determine the accuracy of parameter estimation, of a numerically synthesized signal (frequency), through the proposed algorithm a canonical signal was initially chosen:

$$y(t) = 1e^{\sigma_1 t}\sin(2 \cdot \pi \cdot f_1 \cdot t) + 1e^{\sigma_2 t}\sin(2 \cdot \pi \cdot f_2 \cdot t) \qquad (4.1)$$

On this signal several tests were carried out as the parameters of interest varied, namely:

1) In the first scenario, the frequencies are fixed and the dampings are varied:
   - $f_1 = 0.1\ Hz$;
   - $f_2 = 0.6\ Hz$;
   - $\sigma_1 = [-0.05; 0.05; 0.1; 0.15; 0.2; 0.25; 0.3]$;

- $\sigma_2 = [-0.05; 0.05; 0.1; 0.15; 0.2; 0.25; 0.3]$.

2) In the second scenario, the dampings were fixed and the frequencies varied:
   - $\sigma_1 = 0.1$;
   - $\sigma_2 = 0.3$;
   - First case, $f_2 = 1$ and $f_1 = (0.1; 0.9)$;
   - Second case, $f_1 = 0.1$ and $f_2 = (0.9; 0.2)$.
     As the Δf changed, it was possible to analyze both cases in which both components are at low frequencies and cases in which they are at high frequencies.

In all tests, error in estimating the parameters of interest, i.e., damping, is assessed:

$$errore\% = \frac{\hat{x} - x}{x} \cdot 100 \tag{4.2}$$

Where $\hat{x}$ is the estimated parameter and x is the real parameter. These are then depicted appropriately with respect to the values of the variable parameters.

Damping variation

In the Figure 4.1 are shown on the z axis the damping error related to the i-th component and on the x and y axes the variations of the damping of the individual components.

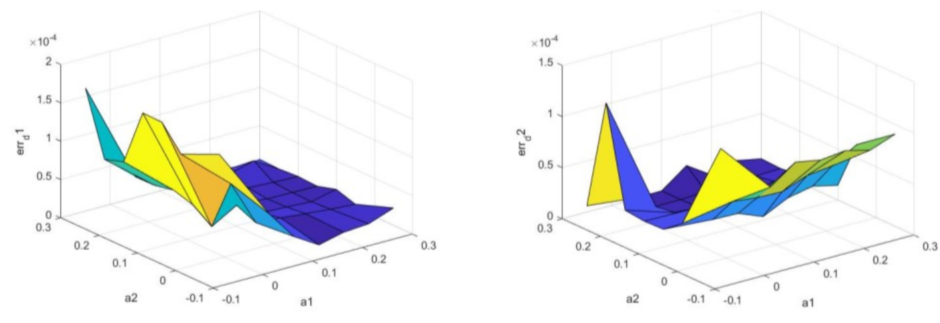

(a) (b)

Figure 4-1 (a) Damping error of first component (b) Damping error of second component

As can be seen from the Figure 4.1, the higher errors are obtained, in

this case, when the two components turn out to have damping of opposite sign, this can also be seen from the Table 4.1 where in the two cases, chosen randomly, the error is reduced by an order of magnitude.
This essentially happens because the spectrum of the signal is more influenced by the component characterized by a negative damping. This result can be seen in the Figure 4.2, where two spectra reproducing two different cases are shown. In the case of components with damping of opposite sign the minimum point between the spectra of the mono-components is raised, this implies a greater error on parameter evaluation due to a greater portion of the spectrum of the negative damping component being approximated.

Table 4.1 Damping error of first component and of second component

COMPONENT 1	DAMPING CASE 1	DAMPING CASE 2
REAL	-0.05	0.1
ESTIMATED	-0.04997	0.0999982
RELATIVE ERROR [%]	1.3 E-04	-1.8 E-06
COMPONENT 2	**DAMPING CASE 1**	**DAMPING CASE 2**
REAL	0.05	0.2
ESTIMATED	0.050031	0.1999987
RELATIVE ERROR [%]	3.1 E-05	-1.3 E-06

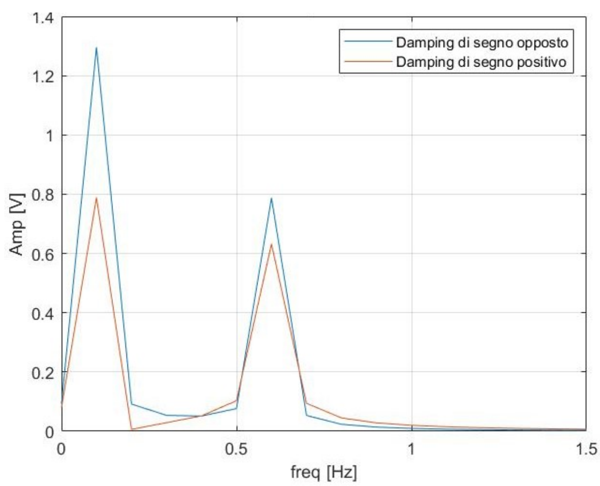

Figure 4-2 Signal Spectrum

For further analysis, even during the simulated tests, a 8-bit numerical quantization error and a Gaussian white noise of a signal-to-noise ratio of 40 dB were applied to the above synthesized signal. As an example, Figure 4.3 shows one of the adopted simulated signal, where the quantization effect is clearly evident.

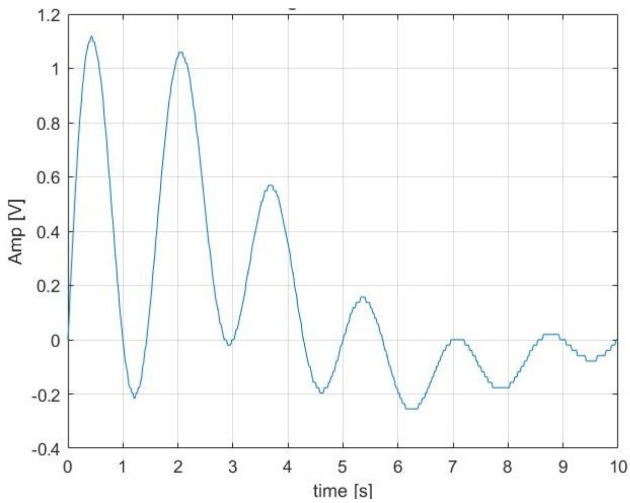

Figure 4-3 Signal generated

Proceeding to process all possible combinations related to the considered scenario, it can be seen (Figure 4.4) that in the ideal case of the signal not affected by any noise, the error committed on the damping estimation is of the order of 10^{-4}%, while applying to it the quantization error and the noise shows an increase in the estimation error, which remains below 1% in any case.

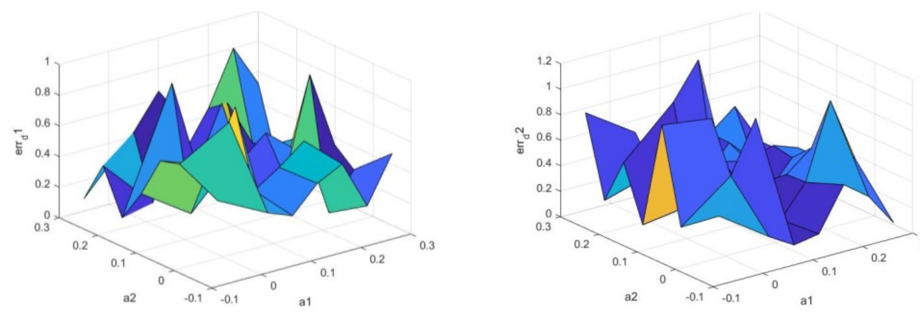

(a) (b)

Figure 4-4 (a) percent error of damping of component 1; (b) percentage error of component damping 2

Frequency variation

In the case of frequency variation, as mentioned above, it was decided to vary only one parameter at a time, so as to be able to analyze the various scenarios. This implies a reproduction of the estimation error no longer with respect to three axes but only with respect to the x and y axes, which represent, respectively, the difference Δf between the frequency of components and the estimation error of the i-th damping (Figure 4.5).

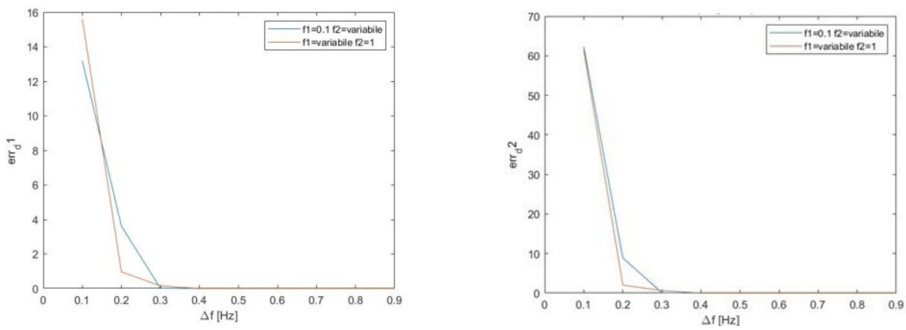

(a) (b)

Figure 4-5 (a) percent error of damping of component 1; (b) percentage error of component damping 2

Also in this scenario, the case in which a quantization error is applied to the canonical signal was analyzed. The results obtained show that the estimation error remains less than 1% until the Δf is greater than or equal to 0.3 Hz. If the frequency distance between the components is lower than 0.3 Hz, the error begins to grow (Figure 4.6).

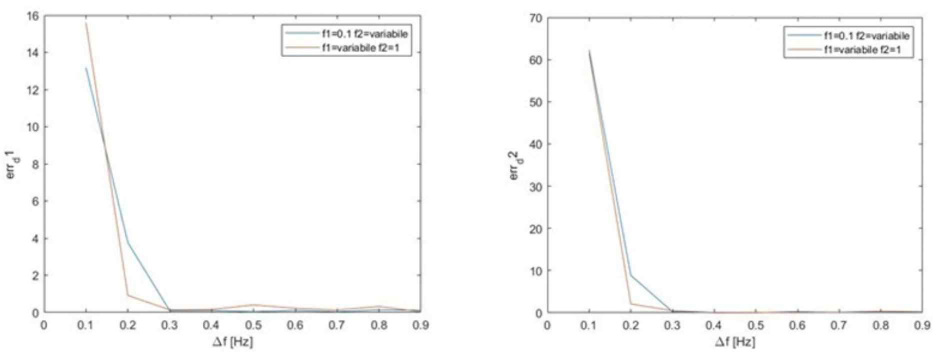

(a) (b)

Figure 4-6 (a) percent error of damping of component 1; (b) percentage error of component damping 2

The critical point occurs at a $\Delta f = 0.1\,Hz$ where, given the adopted frequency resolution, it is not possible deriving the bisector frequency from the frequency.
Consider the signal reported in equation (4.1), where:

- $f_1 = 0.2\,Hz$
- $f_2 = 0.3\,Hz$
- $\sigma_1 = 0.1$ s^{-1}
- $\sigma_1 = 0.3$ s^{-1}

Figure 4.7 shows the representation of this signal in the time domain and frequency domain.

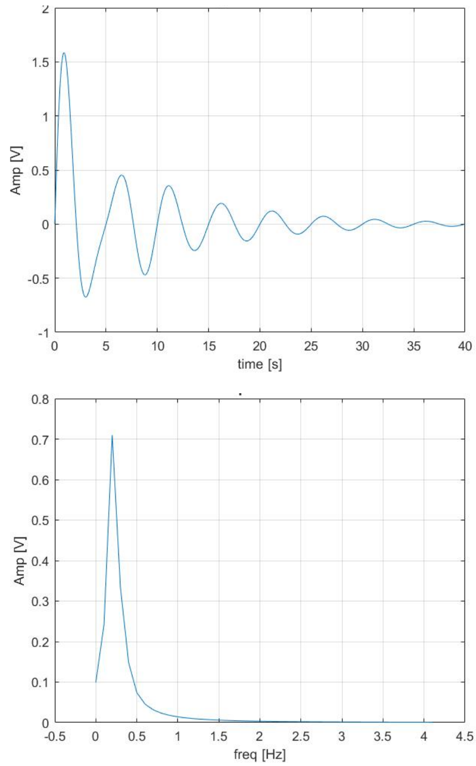

(a)

(b)

Figure 4-7 (a) Signal generated; (b) Signal spectrum

The algorithm as a first approach to this problem acquires 10 s of the signal, makes the frequency analysis and not recognizing the two peaks related to the two mono-components behaves as if it had acquired a signal consisting of a single component, obtaining the parameters of interest. With the latter reconstructs the signal and a comparison is applied with the windowed acquired signal.

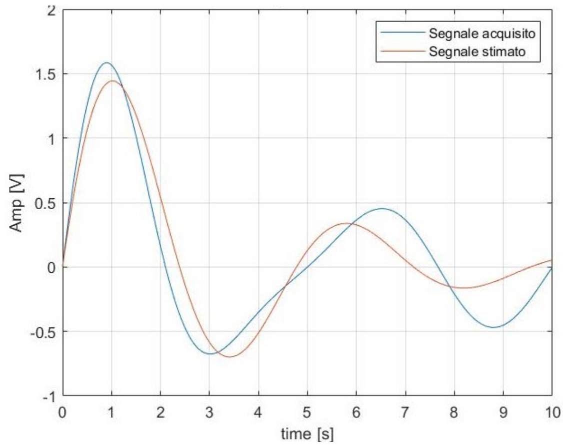

Figure 4-8 Comparison of generated and estimated signal

As shown in Figure 4.8, the first reconstruction of the signal is affected by a big error due, essentially, to the presence of a second component not considered. This error is evaluated by the algorithm through the mean square error between the samples of estimated and synthesized signals:

$$\varepsilon = \frac{1}{N}\sum_{i=1}^{N}(y_i - y_{t,i})^2 \tag{4.3}$$

After numerous tests, a threshold of 0.1 was set for ε ; when this threshold is reached, the algorithm finishes applying moving windows. In the considered example, this occurrence is verified in the second window, as can be seen from the Figure 4.9.

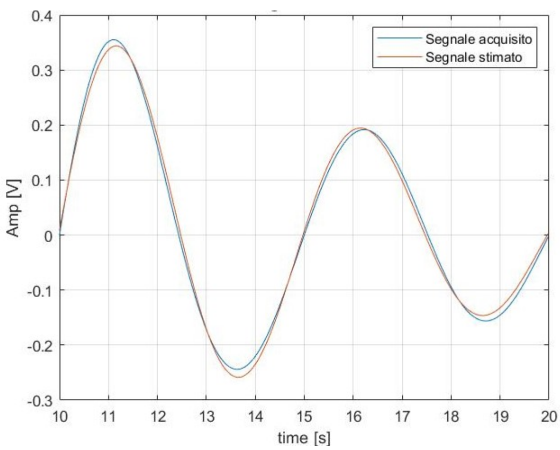

Figure 4-9 Comparison of generated and estimated signal

What occurs in this case is that, after 10 seconds, the component with greater damping is cancelled and consequently the error on the parameter estimation decreases dramatically.
To solve these critical cases, it was decided to obtain as soon as possible the sign of the damping of the predominant component so as to understand if one of the two components is divergent. On the other hand, if the two components are convergent, it is necessary to derive the parameters of the weakly dampened component to ensure the stability of the system over time.
It is interesting to analyse a further example, where one of the two components appears to be divergent and it is therefore of fundamental importance to obtain this information as soon as possible.
In particular the parameters are:

- $f_1 = 0.2\ Hz$
- $f_2 = 0.3\ Hz$
- $\sigma_1 = -0.05$ s^{-1}
- $\sigma_1 = 0.3$ s^{-1}

In the Figure 4.10 the representation of this signal both in the time domain and in the frequency domain is shown.

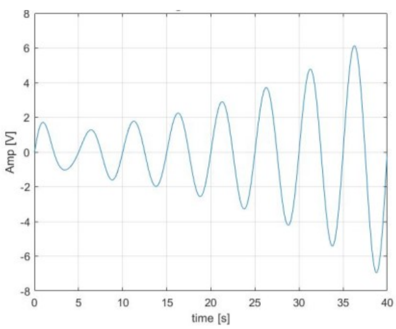

(a)

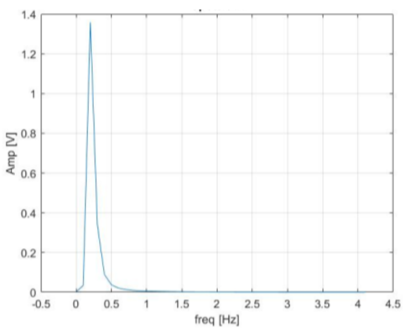

(b)

Figure 4-10 Evolution of the synthesized signal both in time (a) and in frequency (b) domain.

As can be seen from the Figure 4.11, the estimation of the parameters of the windowed signal on the first 10 s is affected by a high error.

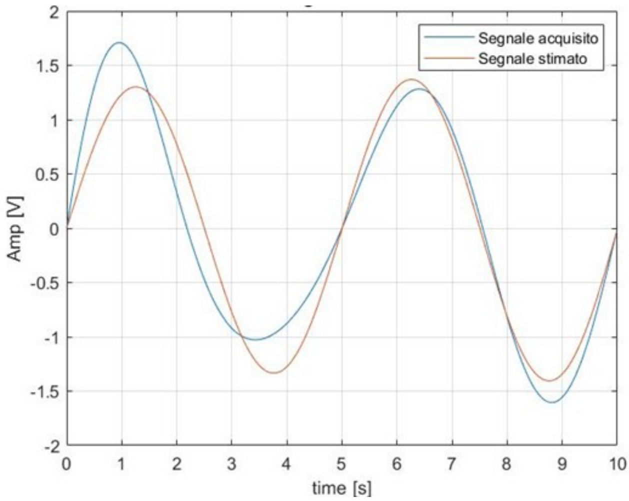

Figure 4-11 Comparison of generated and estimated signal

The overall signal is the sum of two or more components, so its damping turns out to be the sum of exponentials. For this reason the sign of overall damping is strongly influenced by the presence of a divergent component. As it can be observed in these cases, despite the value of the average damping is affected by a notable error, in the first 10 s it is possible to establish with extreme accuracy the damping sign, which allows to verify the presence of a divergent component in order to give an alarm signal, and then obtain greater accuracy by giving time to the algorithm to analyze, as can be seen from the Figure 4.12, where in the second window of the signal the error is negligible.

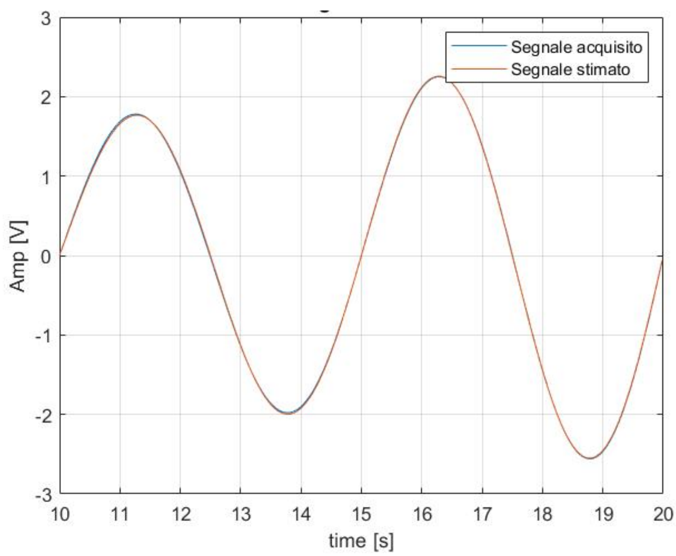

Figure 4-12 Comparison of generated and estimated signal

4.1.2 Experimental Tests

In order to test the proposed algorithm on signals actually provided by real devices, to verify the errors made in the evaluation of damping even in real cases, the method has been assessed through a signal provided by a signal generator. The obtained signals are acquired by an oscilloscope and transmitted to a computer through a GPIB 488.2 in order to analyze them with the algorithm developed in Matlab environment. In particular, the experimental station consists of:

- Agilent 33220A Signal Generator
- Tektronix TDS 2024 Oscilloscope
- GPIB USB-HS National Instrument

As done in numerical tests, even in the experimental phase the performed tests are based on the reproduction of two scenarios, similar to those described above.

Damping variation

The results obtained in the experimental phase, as can be seen from Figure 4.13, are congruent with those obtained in the numerical phase, where the critical points arise more in cases where the components exhibit damping of opposite sign. Although during this phase the signal is subject to real quantization noise, errors are contained below 10%.

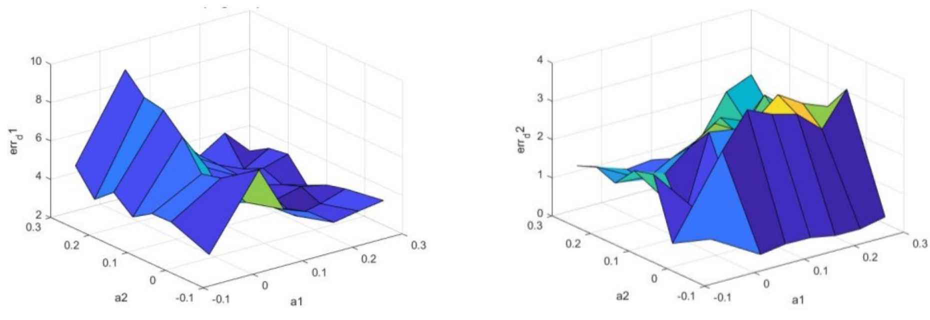

(a) (b)

Figure 4-13 (a) percent error of damping of component 1; (b) percentage error of component damping 2

Frequency variation

As it can be seen from the Figure 4.14, even in experimental tests the same events occur as in simulated tests with the difference that given the presence of quantization noise on the acquired signal there is a small increase in the range of errors

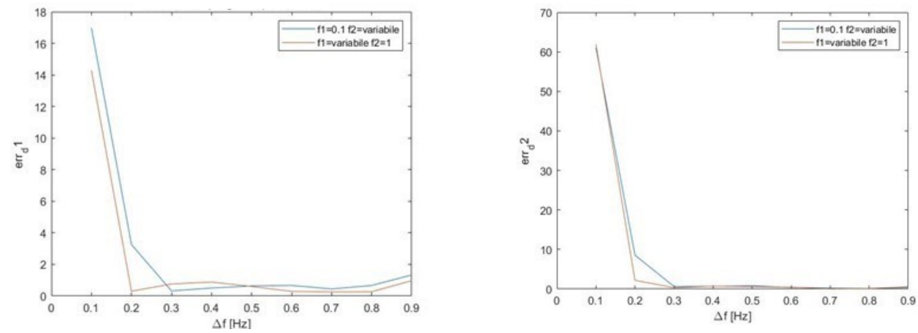

(a) (b)

Figure 4-14 (a) percent error of damping of component 1; (b) percentage error of component damping 2

4.1.3 Tests with non-coherent sampling

In order to reproduce all the possible test scenarios of the proposed algorithm, the case of application of non-coherent sampling was also analyzed in the simulated phase. In the reality of inter-area oscillations it is not possible to guarantee a coherent sampling being non-periodic phenomena and not knowing a priori the period. Consider the signal reported in equation (4.1), where:

- $f_1 = 0.22\ Hz$
- $f_2 = 0.65\ Hz$
- $\sigma_1 = 0.1$
- $\sigma_2 = 0.3$

The results of the parameters of interest obtained at the output of the algorithm are shown in the Table 4.2.

Table 4.2 Risultati ottenuti per il componente 1 e il componente 2

COMPONENT 1	AMPLITUDE	FREQUENCY	DAMPING
REAL	1 V	0.22 Hz	0.1
ESTIMATED	0.9999925 V	0.208 Hz	0.099979
RELATIVE ERROR [%]	-7.5 e-06	-0.012	-2.1 e-05
COMPONENT 2			
REAL	1 V	0.65 Hz	0.3
ESTIMATED	0.9999975 V	0.6438 Hz	0.2999966
RELATIVE ERROR	-2.5 e-06	-0.0012	-3.4 e-06

As it can be seen from the obtained results, even applying non-coherent sampling, the estimation error remains below a threshold of 1%.

4.2 Extended and Unscented Kalman Filters

Referring to the effective value of the main voltage components:

$$E = E_{50} + \sum_{i=2}^{n} A_i \cdot e^{-\sigma_i \cdot t} \cdot \sin(2\pi f_i \cdot t + \varphi_i) \qquad (4.4)$$

and assuming the filtering of the component associated with 50 Hz, the effects of electromechanical oscillation on electrical quantities are accurately described by the relationship:

$$E_{oscill} = \sum_{i=2}^{n} A_i \cdot e^{-\sigma_i \cdot t} \cdot \sin(2\pi f_i \cdot t + \varphi_i) \qquad (4.5)$$

This mathematical model therefore represents the first significant hypothesis of the analysis conducted. Another hypothesis underlying the tests carried out is that the component tones of the oscillation are two in number.

It can also be observed from the previous relation how, also in this case, four *free parameters* are associated with each damped exponential mode:

- Damping σ_i;
- Frequency f_i;
- Amplitude A_i;
- Phase φ_i.

At a preliminary stage, amplitudes and phases were assumed known, limiting the estimation to the damping and frequency of each component mode only.

The frequencies were assumed to belong to the characteristic set of the mode sought:

f = {0.1 0.2 0.3 0.4 0.5 0.6 0.7 0.8 0.9 1} Hz

The damping to the set:

D = {-0.05 -0.04 -0.03 0.03 0.04 0.05 0.1 0.2 0.3 0.4 0.5} s^{-1}

Further imposition is the consistent sampling condition, i.e. the ratio of sampling rate to signal frequencies is obtainable from the relationship:

$$\frac{f_s}{f_i} = \frac{N}{M} \quad \textit{with}\ \text{N ed M integers} \tag{4.6}$$

The last hypothesis is the addition of *white noise* in order to guarantee a signal to noise ratio of 50 dB.

4.2.1 Extended Kalman Filter

As anticipated in the previous chapter, the Extended Kalman Filter (EKF) involves a linearization of the model around a reference point. The linearization process is all the more effective the slower the signal evolution over time. The oscillations examined fall fully within the class of *slowly variable signals* and, therefore, the EKF produces satisfactory results in this type of application.
During the calibration phase, the following parameters were defined:

- $\mathrm{Q} = 10^{-2}\ \mathrm{I}_{4x4}$ (process noise covariance matrix)
- $\mathrm{R} = 10^{-2}$ (measurement noise covariance matrix)

For the initialization of the state vector and its matrix of convariances, the only information available in the preliminary phase was exploited, namely the intervals of belonging to the parameters of interest:

- $\sigma_\mathrm{i} \in [-0.05; 0.5]\ s^{-1}$
- $\mathrm{f_i} \in [0.1; 1]$ Hz

Starting from a condition of absence of information, it is assumed that the state vector, in the role of random variable, is defined by a function of uniform probability distribution. The consequence of this assumption is the following initialization of the filter:

$$\begin{aligned} x_0^i &= \mu_i = \int_{-\infty}^{+\infty} \mathrm{X_i}\ \mathrm{pdf(X_i)}\ \mathrm{dX} \\ var_0^i &= \int_{-\infty}^{+\infty} (\mathrm{X_i} - \mu_i)^2\ \mathrm{pdf(X_i)}\ \mathrm{dX} \end{aligned} \tag{4.7}$$

Where the superscript 'i' is the i-th element of the state vector.

Filter performance is inevitably affected by the sampling rate of PMUs. The linearization required by the EKF is all the more effective the smaller the time interval on which it is carried out. Therefore, the higher the sampling rate, the shorter the period over which linearization is carried out, increasing the performance of the filter. The EKF then works with a sampling frequency of 50 Hz, the frequency at which the Italian PMUs operate.

Convergence

To highlight the convergence of the filter, the case reported in Table 4.3 was considered.

Table 4.3 Parameters of both components

A_1 [V]	A_2 [V]	f_1 [Hz]	f_2 [Hz]	σ_1 [s^{-1}]	σ_2 [s^{-1}]	φ_1 [rad]	φ_2 [rad]
1	1	0.5	0.7	-0.05	0.5	0	π

The Figure 4.15 show a saturation of the correcting action of the filter over time. Convergence, although with minimal error, is guaranteed. An advantage of algorithmic methods is that with them there is an estimator of the measurement uncertainty due to the updating of the state parameters' covariance matrix. Since the filter is a mathematical tool that aims to minimize the variances associated with the state, it is observed that, as time passes, the band of uncertainty affecting the measurement becomes progressively thinner.

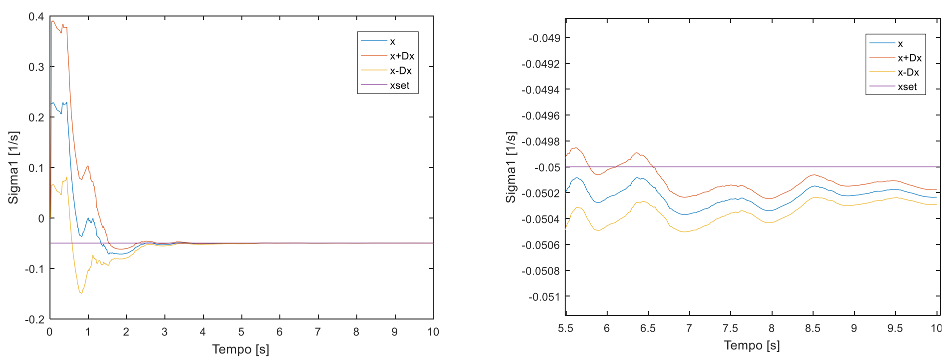

(a) (b)

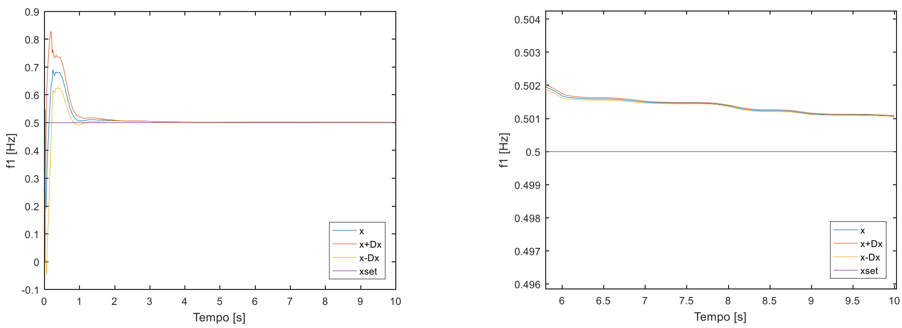

(c) (d)

Figure 4-15 (a) Estimation of sigma$_1$ damping over time, (b) Filter saturation on sigma$_1$ estimate, (c) Estimation of frequency f_1 over time and (d) Saturation of the filter on the estimate of f_1

3-D Charts

The method has been assessed according to two scenarios. In the first case, CASE 1, the adopted signal parameters are reported in Table 4.4.

Table 4.4 Signal parameters of Case 1

A_1 [V]	A_2 [V]	f_1 [Hz]	f_2 [Hz]	σ_1 [s^{-1}]	σ_2 [s^{-1}]	φ_1[rad]	φ_2[rad]
1	1	0.2	0.7	variable	variable	0	π

As shown in Figure 4.16, after only two seconds the sign of damping is estimated correctly.

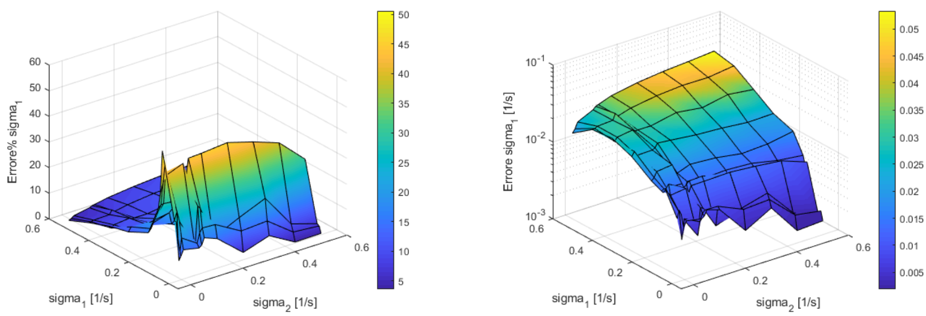

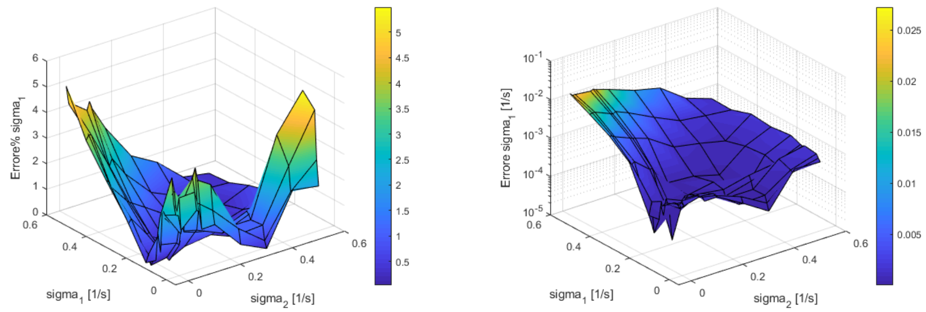

Figure 4-16 Damping error over time in percentage (left) and absolute terms on logarithmic scale (right)

The estimation of frequencies (Figure 4.17) is considerably faster; errors of less than ten percentage points are achieved after only two seconds.

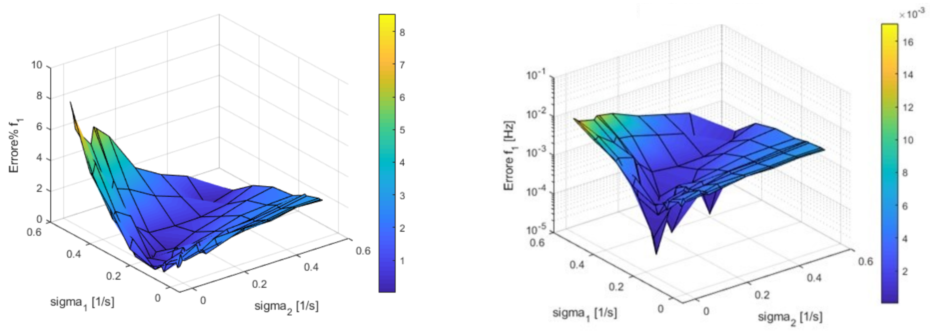

Figure 4-17 Frequency error over time in percentage (left) and absolute terms on logarithmic scale (right)

In the simulation phase, a deterioration in the performance of the filter was manifested as the values of the frequency distance Δf between the components.
Then, the CASE 2 (whose parameters are reported in Table 4.5) was considered.

Table 4.5 Signal parameters of Case 2

A_1 [V]	A_2 [V]	f_1 [Hz]	f_2 [Hz]	σ_1 [s^{-1}]	σ_2 [s^{-1}]	φ_1[rad]	φ_2[rad]
1	1	0.2	0.3	variable	variable	0	π

This case is the case where the worst performance of the EKF is recorded but convergence is still guaranteed. Unlike the previous case, in order for the damping sign to be guaranteed, it is necessary to wait a time equal to four seconds (Figure 4.18).

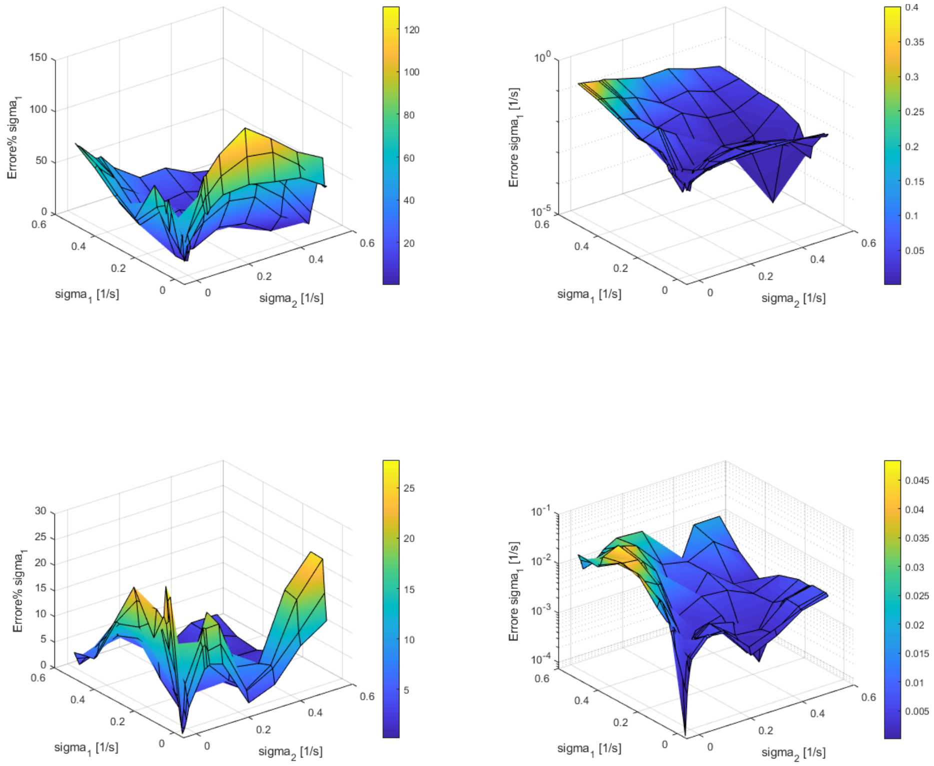

Figure 4-18 Damping error over time in percentage (left) and absolute terms on logarithmic scale (right)

However, the EKF performs poorly if one of the two tones oscillates at a frequency of 0.1 Hz. In such case, a $\Delta f \;=\; 0.3\,Hz$ (loss of resolution) is required for the two tones to be observed correctly. As it can be seen by comparing the results of the previous case by imposing two frequencies of 0.1 and 0.2 Hz, the performance of the filter is extremely degraded.

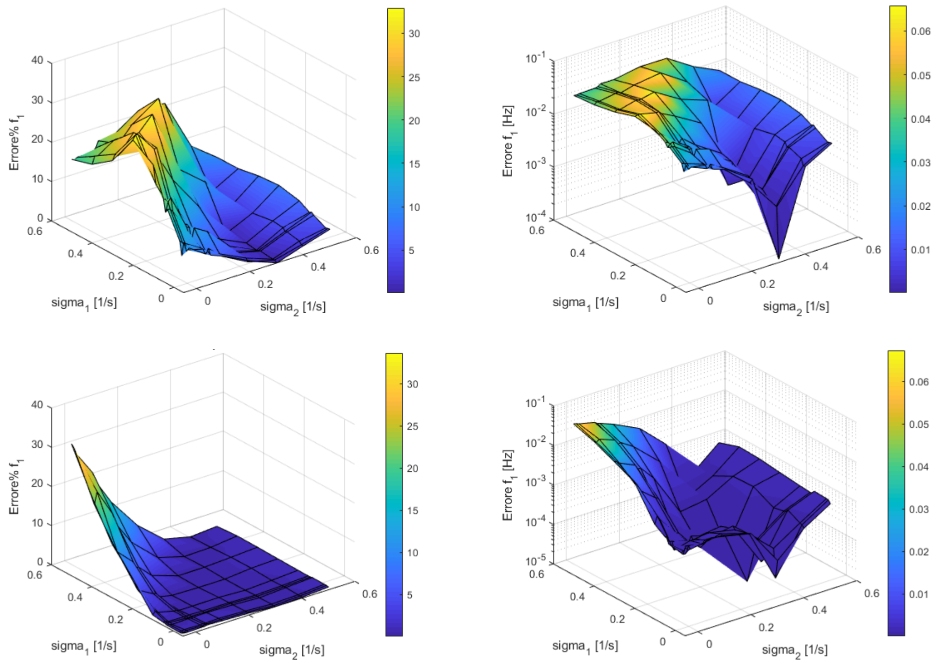

Figure 4-19 Frequency error over time in percentage (left) and absolute terms on logarithmic scale (right)

4.2.2 Unscented Kalman Filter

As with the EKF, the same introductory assumptions were made for the Unscented Kalman Filter (UKF) The state vector and its covariance matrix were initialised according to the equations (4.7). During the calibration phase, the following parameters were defined:

- $n_a = 5$ (increased size of the state vector);
- $n_{SP} = 2n_a + 1$ (number of sigma points);
- $R = 1^{-4}$ (measurement noise covariance matrix);
- $W^{(0)} = \frac{1}{3}$ (weight of the 'central' sigma point);
- $W^{(i)} = \frac{(1-W^{(0)})}{n_{SP}-1}$ (weight of 'peripheral' sigma points).

Unlike the EKF, with the UKF, as no linearisation is required, there is no lower limit to the sampling rate. In the simulation phase, the following results were highlighted:

- Operating with a sampling rate of 50 Hz, the performance of the filter is degraded in the detection of 'low' frequencies (e.g. 0.2 Hz, 0.3 Hz).
- Operating with a sampling rate of 10 Hz, minimum for PMUs, a specular behaviour is obtained, i.e. the performance is

degraded for the measurement of 'high' frequencies (e.g. 0.8 Hz, 0.9 Hz).

The compromise between the two requirements led to the choice of a sampling rate of 25 Hz.

Convergence

To highlight the convergence of the filter, the case reported in Table 4.6 was considered.

Table 4.6 Parameters of both components

A_1 [V]	A_2 [V]	f_1 [Hz]	f_2 [Hz]	σ_1 [s^{-1}]	σ_2 [s^{-1}]	φ_1[rad]	φ_2[rad]
1	1	0.5	0.7	-0.05	0.5	0	π

As shown in Figure 4.20, comparing the performance of the UKF with that of the EKF shows that:
The transitional phase of the UKF is faster than that characterizing the EKF, i.e., the measurement error first falls below a certain threshold.
When fully operational, the estimate obtained through UKF exhibits errors comparable to those obtained with EKF.

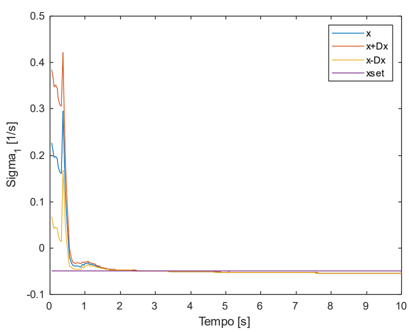

(a)

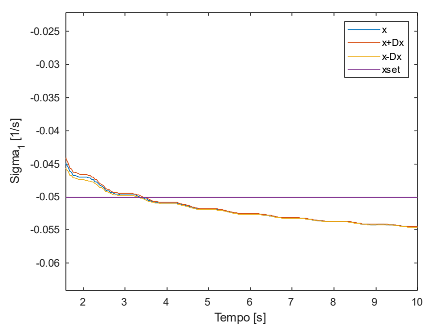

(b)

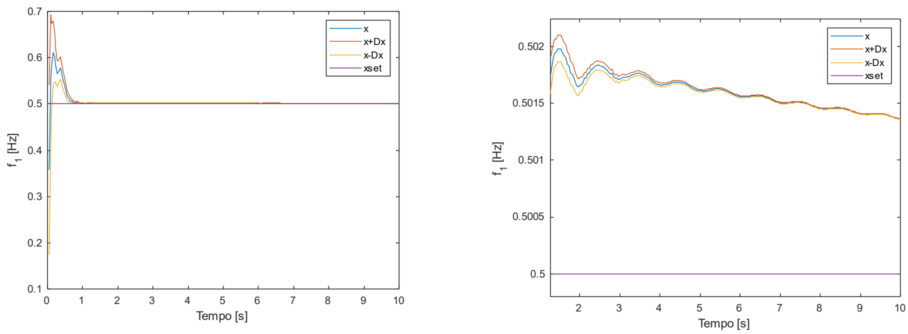

(c) (d)

Figure 4-20 Estimate of (a) $sigma_1$ over time, (b) $sigma_1$ at full speed, (c) f_1 over time and (d) f_1 at full speed

3-D Charts

From the following graphs, it can also be seen that the UKF has degraded performance if the two components have a spectral distance of 0.2 Hz. In fact, it can be seen from the results of case 2 that the frequency estimation error at 0.2 Hz is still high.
Considering the <u>CASE 1</u> reported in Table 4.4, the results shown in Figures 4.21 and 4.22 are obtained.

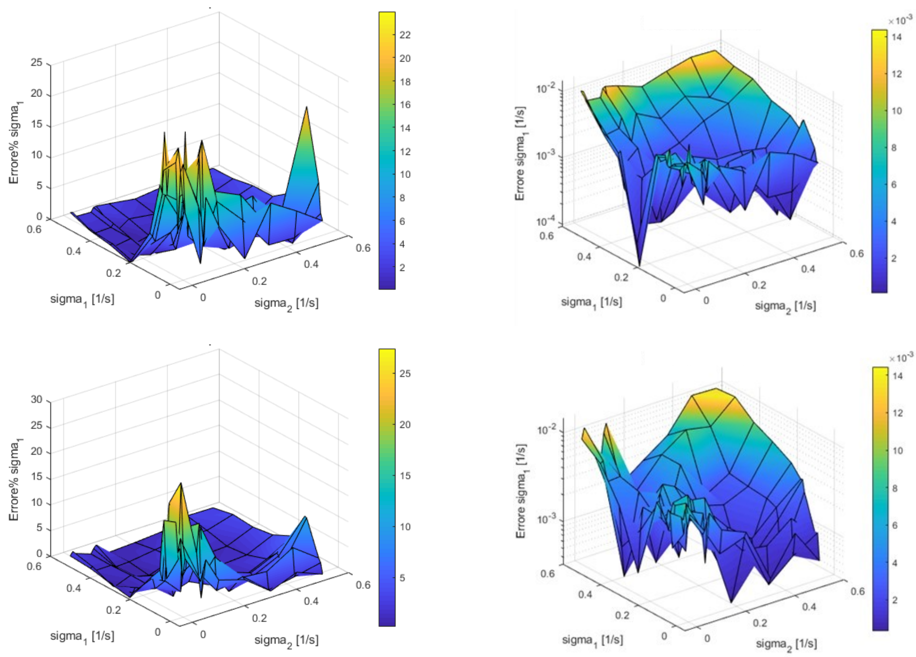

Figure 4-21 Damping error over time in percentage (left) and absolute terms on logarithmic scale (right)

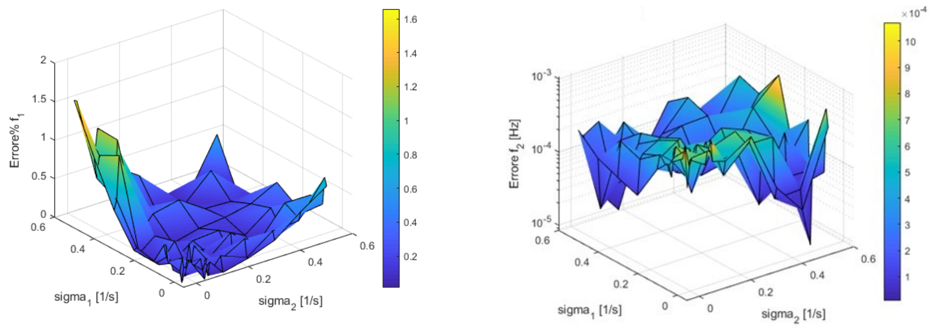

Figure 4-22 Frequency error over time in percentage (left) and absolute terms on logarithmic scale (right)

Case 2

CASE 2 is reported in Table 4.5

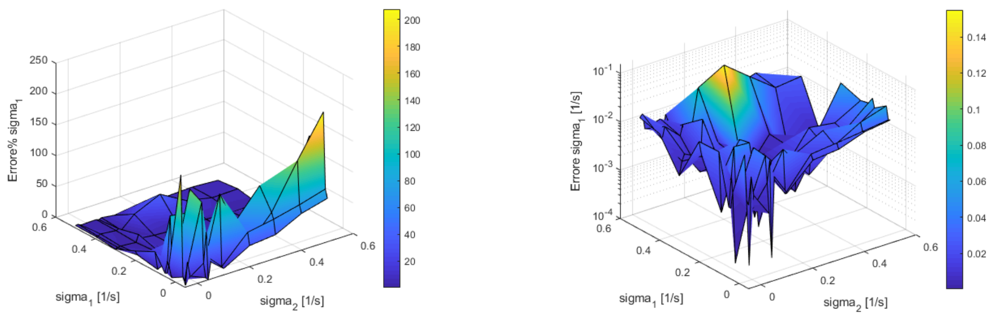

Figure 4-23 Damping error over time in percentage (left) and absolute terms on logarithmic scale (right)

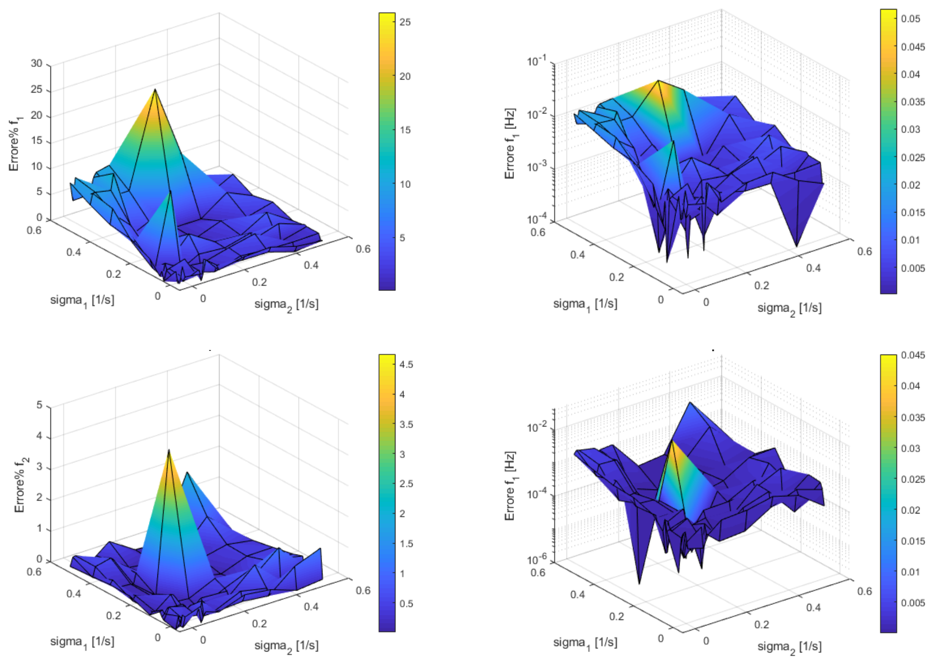

Figure 4-24 Frequency error over time in percentage (left) and absolute terms on logarithmic scale (right)

However, the method guarantees the convergence if the frequency distance Δf is equal to 0.2 Hz, evan if one of the two frequencies is equal to 0.1 Hz, as evidenced by the graphs below.

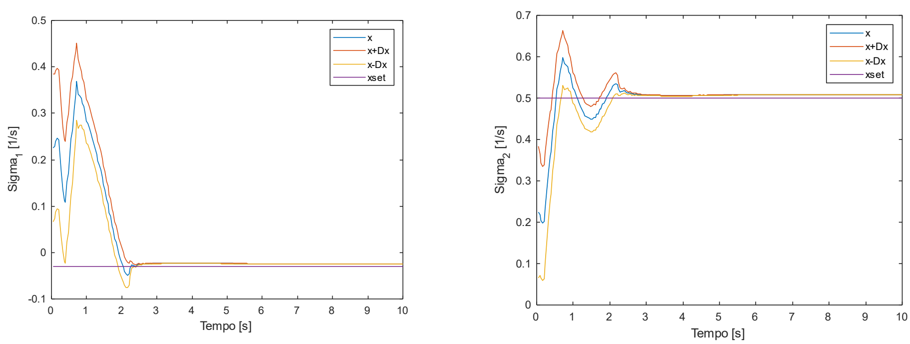

Figure 4-25 Estimation of damping over time

4.3 Heuristic Methods (GA and PSO)

In the preliminary phase, before introducing the main algorithm used for estimating parameters in real time, a characterization of the two methods was carried out [7]. Both predict as a fitness function the inverse of the *root mean square error (RMSE)* between the real signal (z) and the estimated one (y) [8]:

$$RMSE = \sqrt{\frac{\sum_{i=1}^{N}(z_i - y_i)^2}{N}} \tag{4.8}$$

In order to evaluate the dispersion of GA and PSO solution, each algorithm was tested a hundred times on the same signal, and, at the end of the process, the probability distribution functions related to the four parameters obtained at the output were reconstructed for both the approaches.
The test signal is modelled as follows:

$$E_{test} = 1 \cdot e^{\sigma_1 \cdot t} \cdot \sin(2\pi f_1 t) + 1 \cdot e^{\sigma_2 \cdot t} \cdot \sin(2\pi f_2 t + \pi) + noise \tag{4.9}$$

Where the parameters are:
- $\sigma_1 = -0.03\ s^{-1}$
- $\sigma_2 = 0.03\ s^{-1}$
- $f_1 = 0.1\ Hz$
- $f_2 = 0.2\ Hz$

By imposing a window of 4s the following results are obtained.

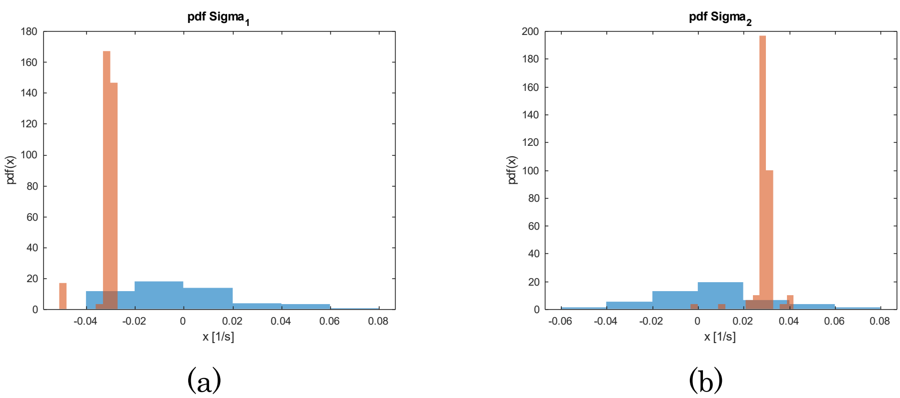

Figure 4-26 (a) Pdf sigma$_1$ via GA (blue) and PSO (red) and (b) Pdf sigma$_2$ via GA (blue) and PSO (red)

[7] For both the GA and the PSO, the functions already present in MatLab.
[8] The "Theoretical" signal is the one reconstructed with the estimates of the parameters.

Table 4.7 Mean, Median and Standard Deviation of the two distributions, Sigma$_1$ (a) and Sigma$_2$ (b)

	Sigma$_1$ [s^{-1}]		
	Average	Median	Dev. Std.
Ga	-0.0024	-0.0074	0.0224
Pso	-0.0311	-0.0301	0.0044

(a)

	Sigma$_2$ [s^{-1}]		
	Average	Median	Dev. Std.
Ga	0.0053	0.0056	0.0226
Pso	0.0293	0.0299	0.0044

(b)

The Figure 4.27 shows a greater dispersion of the estimates obtained through a GA compared to the results given by PSO. This result is evidenced by the values of mean and standard deviation obtained by imposing a time window of four seconds (Table 4.7).
The anomalous behaviour of the PSO represents the inspiration that led to the creation of the algorithm proposed in the next section. In fact, it can be observed how the error tends to fall below the percentage point when considering the distribution's median. Since the target algorithm of this thesis has to work in real time, it is impossible for it to perform repeated measurements on the detected track. The concept of test repeatability will therefore be guaranteed by making measurements with a cadence of one second, considering a window that expands and guarantees the selection of larger portions of the track at each step. This time increment in the windowing will be precisely equal to the step at which the updating of the estimate will take place (1 s).
For the frequencies, on the other hand, the following results were obtained (Figure 4.27).

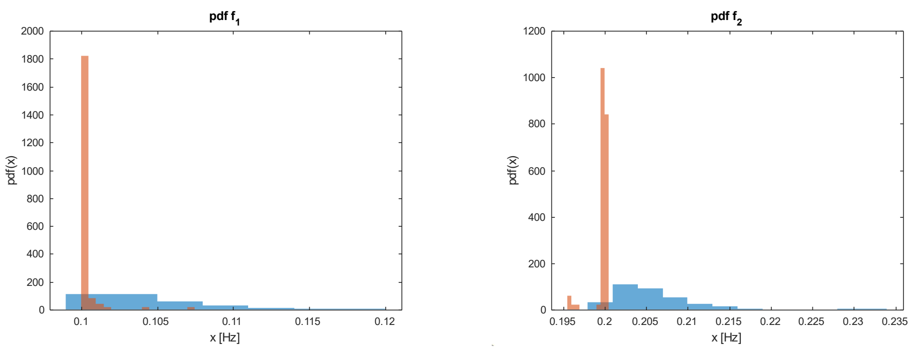

(a) (b)

Figure 4-27 (a) Pdf f$_1$ via GA (blue) and PSO (red) and (b) Pdf $_{f2}$ via GA (blue) and PSO (red)

Also in this case, the GA approach exhibits a greater dispersion if compared to the PSO. Nevertheless, the performance may be considered comparable. Reducing the width of the working window shows a deterioration in the performance of both proposed methods. Increasing the duration of the window, on the other hand, does not see significant improvements.

4.4 PSO with Continuous Weighted Average

According to the previously shown tests, the PSO has been selected as heuristic method for the realization of an algorithm operating in real time. In the literature, most of the conducted research involves the use of PSO for the regulators sizing operating on the electrical system. The poor research that sees the PSO used as an estimator of the parameters that characterize the electromechanical oscillations seem to highlight an absolute convergence of the method, neglecting the problem of "anomalies" recorded during the characterization of the method itself (Figure 4.28).

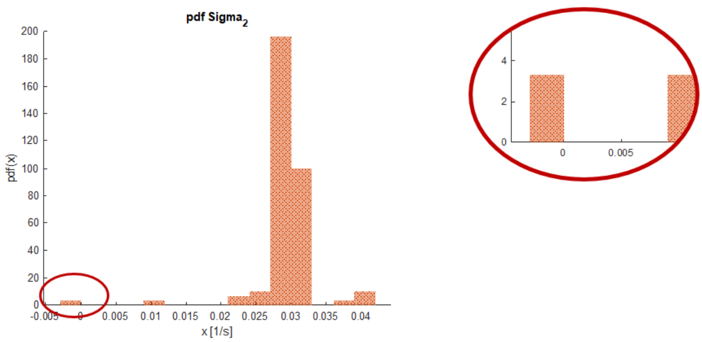

Figure 4-28 Damping probability distribution function obtained with PSO

The proposed algorithm, in order to ensure greater reliability during the measurement phase, provides, in addition to the PSO, the use of an expandable window and a weighted average. The cadence with which the output is updated is 1 s. At each step 'k' the following operations are therefore planned:

1) Extension of the time window by 1 s: $[0; \mathrm{k}-1]\, s \rightarrow [0; \mathrm{k}]$ s ;
2) Start of PSO with the RMSE calculated on the estimate obtained from the window set in step 1 as the fitness function.
3) Parameters are calculated by weighted averaging of the different estimates obtained up to the k-th step via PSO. Each estimate is weighted for the same parameter k (indicating the window duration) so that estimates made on longer frames, being more reliable, have greater relevance.

It should be noted that, in order for the algorithm to operate correctly, the calculation time, due to the PSO and the average step (T_c), must be less than 1 s. Whatever the value of T_c, the effect produced by the intervention of the PSO is a translation of the output along the time axis (delay in information). In the worst case ($T_c = 1\ s$), at step 'k' the estimate shown to the user will be the one calculated on the signal seen between 0 s and (k-1) s. Downstream of the considerations carried out, the results obtained with the aforementioned algorithm are shown below. The PSO has been calibrated as follows:

- Number of particles: 100
- Tolerance: 1e-6
- Maximum number of iterations: 2n (with n = number of variables)
- Maximum number of iterations below tolerance: 25
- Inertia range: [0.1 ; 1]
- Self-adjustment weight (c_1): 1.49
- Social adjustment weight (c_2): 1.49

The signal, taken from the PMUs, is supposed to be sampled at 50 Hz.

4.4.1 3D Charts

The following graphs were obtained by choosing two frequencies from the set {0.1 0.2 0.3 0.4 0.5 0.6 0.7 0.8 0.9 1} Hz and varying the damping in the set {-0.05 -0.04 -0.03 0.03 0.04 0.05 0.1 0.2 0.3 0.4 0.5} s^{-1}
The most critical case involves the following set of parameters:
<u>**CASE 1**</u> reported in Table 4.4.
It is observed that, unlike Kalman filters, the "worst" case examined involves the measurement of two frequencies equal to 0.1 Hz and 0.2 Hz. These conditions, particularly critical for the mathematical estimator, do not seem to cause any particular problems for the proposed method.
From the Figure 4.24 it is clear that:

- The estimate improves over time, i.e. the greater the portion of the track that can be observed;
- The largest percentage errors on damping are observed around zero, i.e. for weakly dampened or slowly diverging oscillations.[9]

[9] It should be noted that, by way of example, a 10% error related to a damping of 0.03 s^{-1} is equivalent to an error in absolute terms of 0.003 s^{-1} (order of 1e-3).

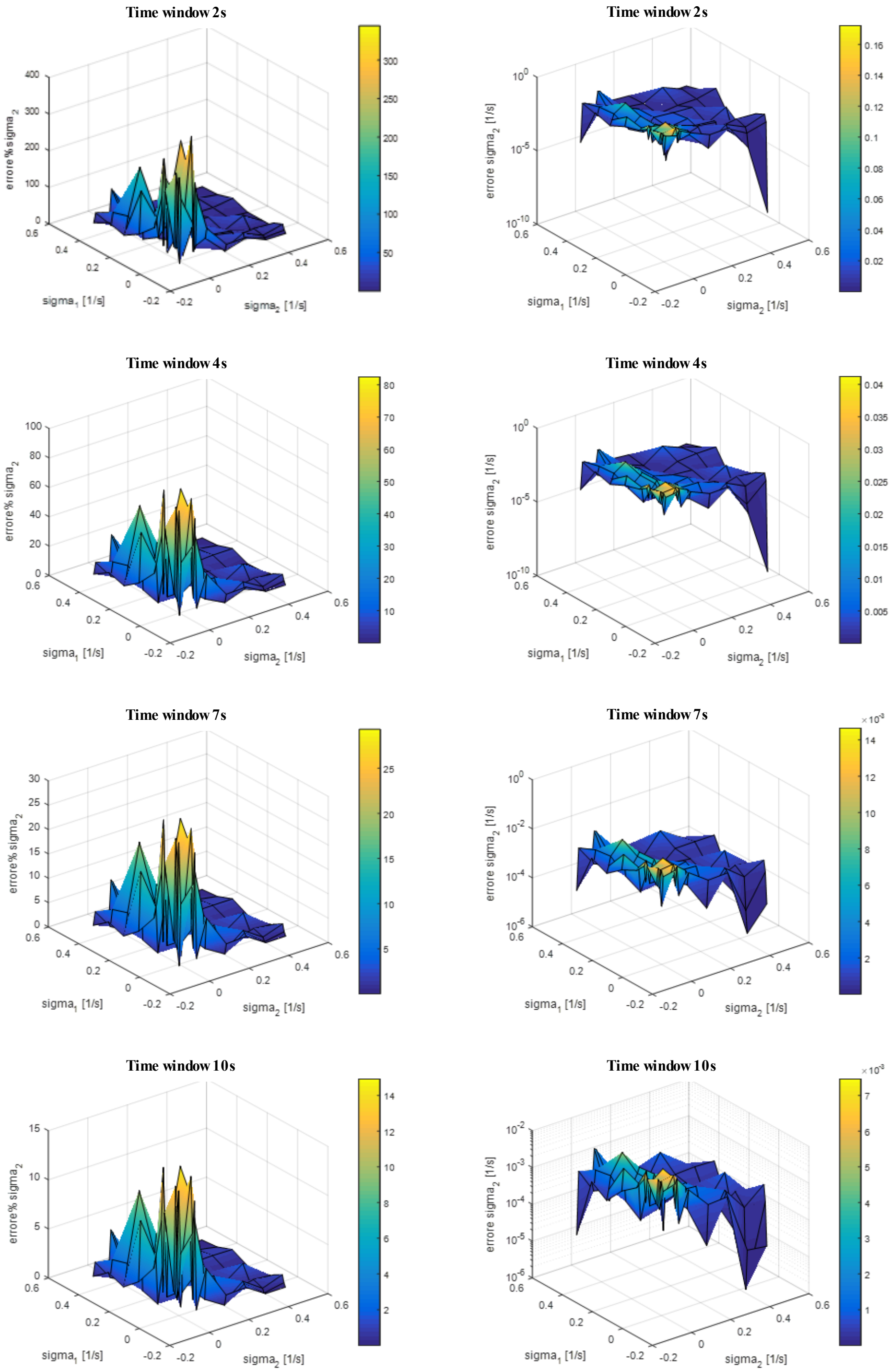

Figure 4-29 Damping error in percentage (left) and absolute terms on logarithmic scale (right)

Frequency estimation takes place more quickly. In just four seconds the percentage error is lower, in the worst case, than 10% of the imposed value (Figure 4.30).

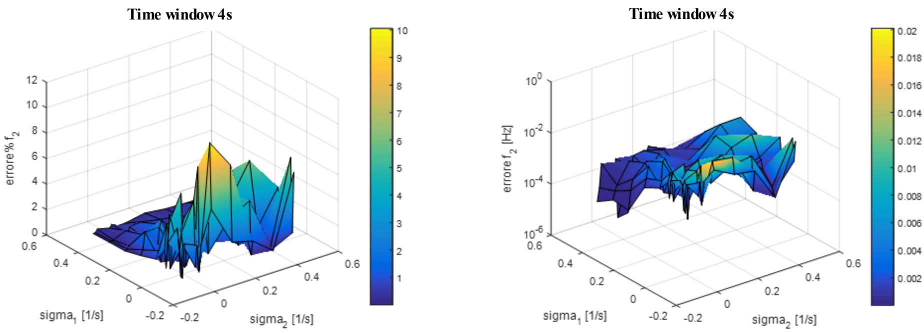

Figure 4-30 Frequency error in percentage (left) and absolute terms on logarithmic scale (right)

The results shown so far refer to the worst case, that is, considering a spectral distance between the two components of 0.1 Hz. If, on the other hand, the two components have a greater spectral distance, that is, the two frequencies differ by an amount greater than 0.1 Hz, the convergence time of the algorithm is shorter.

Consider the **<u>CASE 2</u>** reported in Table 4.5.

It denotes in this case, with the same percentage error, almost a halving of the convergence time (Figures 4.31 and 4.32).

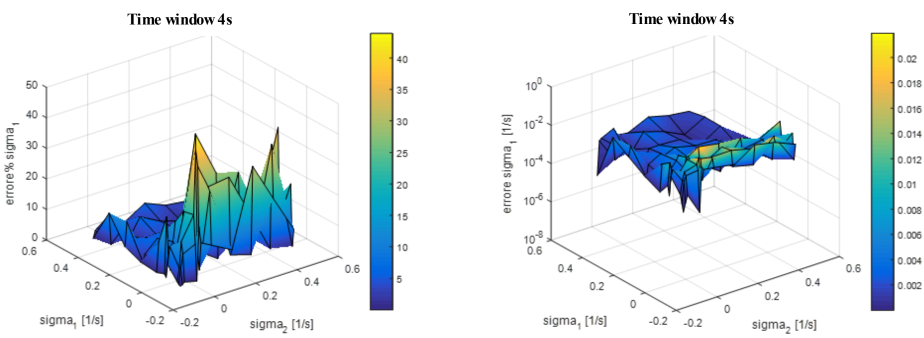

Figure 4-31 Damping $error_1$ in percentage terms (left) and absolutes on logarithmic scale (right)

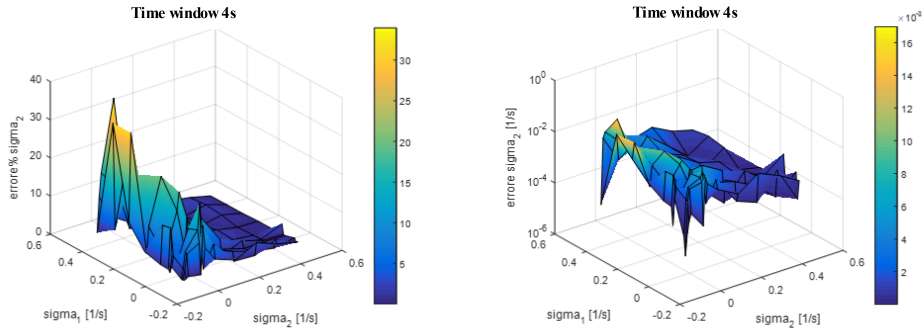

Figure 4-32 Damping error$_2$ in percentage (left) and absolute terms on logarithmic scale (right)

It is worth noting that the phenomenon taken into account regards the electromechanical oscillations of the electrical system. This phenomenon may compromise the stability of the entire electricity grid. In real-time estimation, it is therefore of fundamental importance to know the sign of damping in the shortest possible time. An algorithm capable of realizing this request thus gives Terna (the TSO) full knowledge of what is happening to the electricity system, highlighting any conditions of imminent danger.

4.4.2 Convergence

Assuming in the ideal case $Tc = 0\,s$ and referring to the set of parameters of the CASE 1, the following results are observed:
As regards the **CASE 1** reported in Table 4.4,
from the Figure 4.28, it is clear how the algorithm is able to estimate the sign of damping after just four seconds. It is also highlighted how the output is updated with a cadence equal to 1 s.

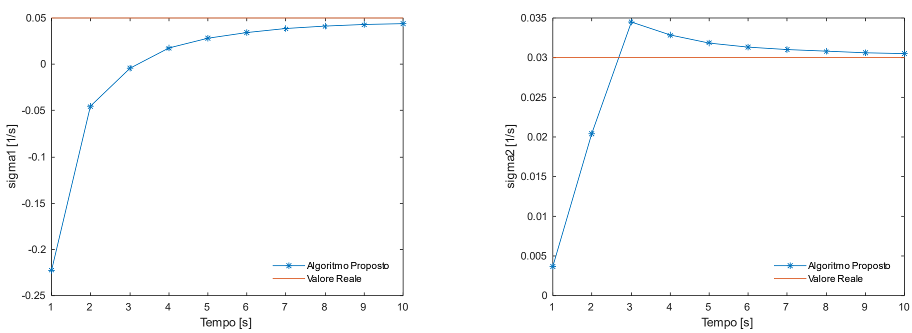

(a) (b)

Figure 4-33 Estimate of (a) damping$_1$ and (b) damping$_2$

If a non-zero calculation time were considered, a translation along the time axis of the estimation of a quantity equal to T_c would be obtained. Once again, the proposed case is one of the most complex. If we move towards higher frequencies, a greater speed of convergence is observed (Figure 4.34).

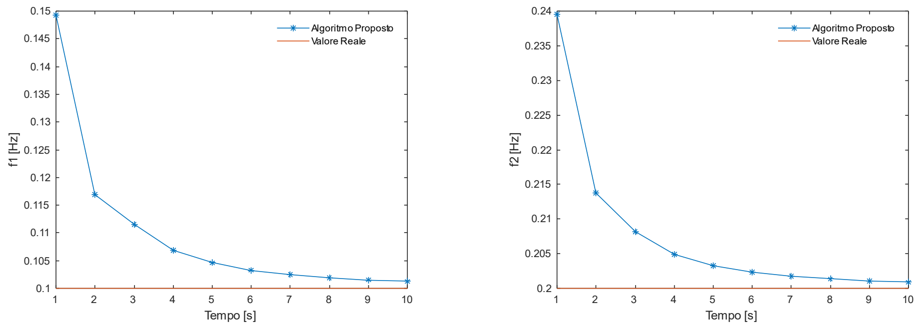

(a) (b)

Figure 4-34 Estimate of (a) frequency_1 and (b) frequency_2

Referring to the **<u>CASE 2</u>** reported in Table 4.5, the trends shown in Figure 4.30 are observed.

It can be concluded that the higher the frequencies, the more efficient is the algorithm. As already appreciated for the other approaches, the algorithm performance is higher when the frequency distance Δf between the oscillations increases (Figure 4.35).

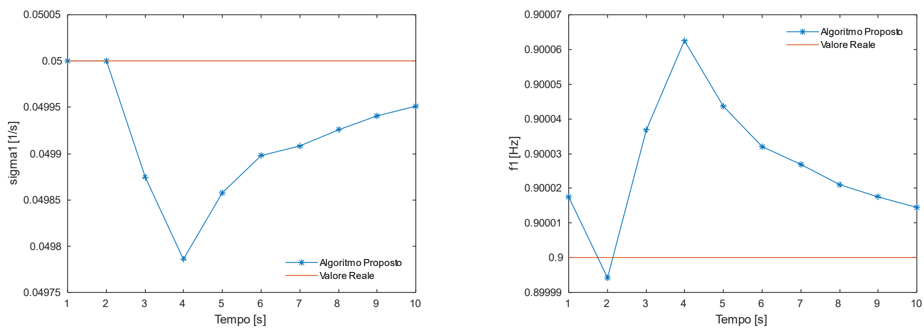

(a) (b)

Figure 4-35 Estimate of (a) damping_1 and (b) damping_2

In the previous tests, simplifying working hypotheses have been used. The following discussion aims to examine the behaviour of the proposed algorithm in conditions of greater "stress" i.e., trying to estimate the amplitude as well.

4.4.3 Estimation of damping, frequencies and amplitudes

The test frequencies are: f_1=0.1 Hz and f_2=0.2 Hz. The trends, shown in Figure 4.36, are obtained

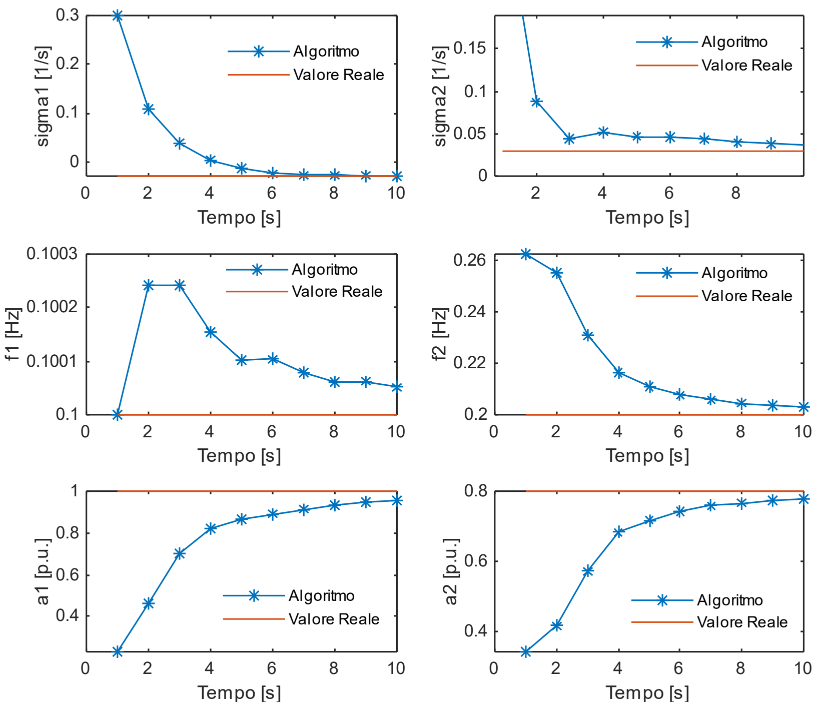

Figure 4-36 Estimation of damping, frequencies and amplitudes

Imposing f_1=0.5 Hz and f_2=0.9 Hz the trends, shown in Figure 4.37, are obtained.

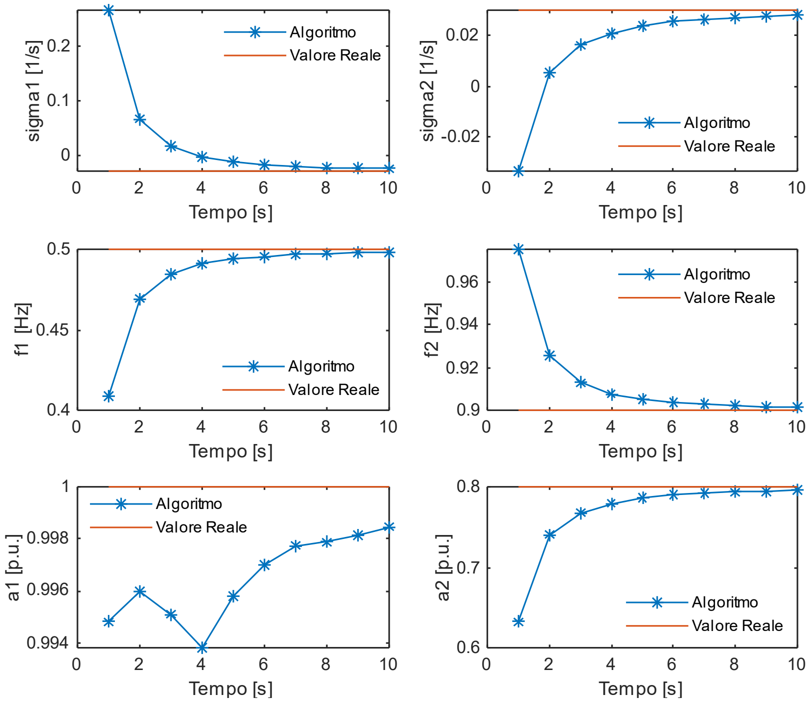

Figure 4-37 Estimates of damping, frequencies and amplitudes

It is observed that, although the obtained results are still acceptable, in order to improve the performance of the method it is necessary to increase the values of the frequencies and the spectral distance between them.

4.4.4 Signal to noise ratio reduced to 25dB

In order to guarantee a signal-to-noise ratio of 25 dB, assuming an amplitude of the two tones equal to 1 p.u., a white noise with variance equal to 0.08 is required. In addition, to obtain reliable results, 0.1 Hz and 0.2 Hz are always used as test frequencies. As shown in Figure 4.38, even in the case of a higher signal-to-noise ratio, the algorithm ensures rapid convergence.

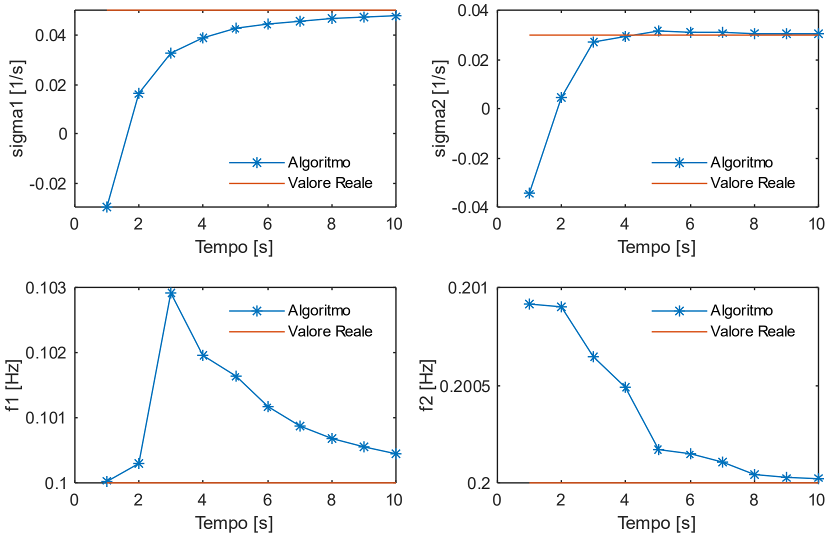

Figure 4-38 Estimates obtained in the case of a signal-to-noise ratio of 25 dB

4.4.5 Non coherent sampling

The following frequencies are imposed: f_1=0.34 Hz and f_2=0.23 Hz. The Figure 4.39 show a slight deterioration in performance, but in any case the reliability of the algorithm is not affected. In fact, after only three seconds the sign of both damping coefficients is detected. Performance improves once again at higher frequencies. In fact, by increasing the frequencies (Figure 4.40)the method exhibits notable performance even with Δf less than 0.1 Hz. The test frequencies are: f_1=0.97 Hz and f_2=1 Hz.

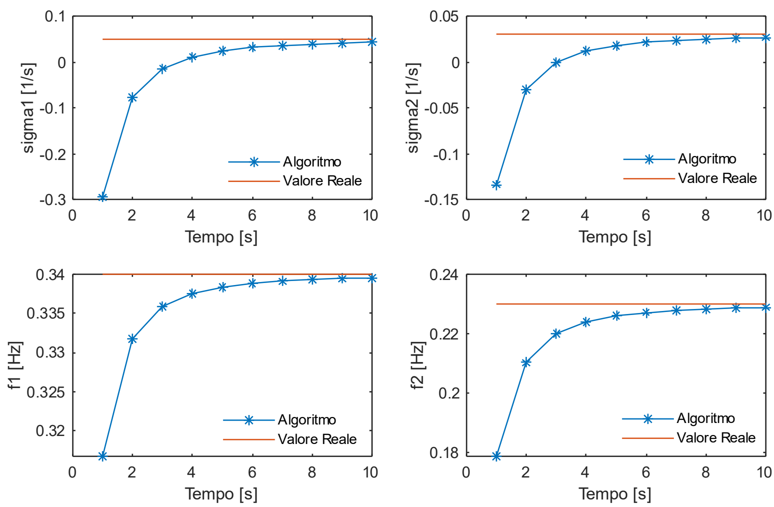

Figure 4-39 Estimates obtained in case of non-coherent sampling

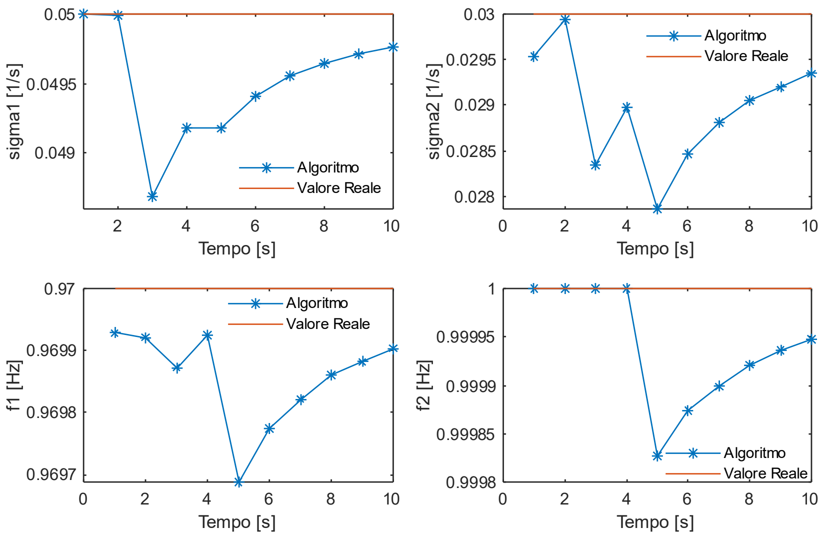

Figure 4-40 Estimates obtained in case of non-coherent sampling

4.4.6 Quantization

The quantization noise resulting from the use of an 8-bit analog-to-digital converter was also simulated, with a full scale equal to 5 V peak to peak.

Worst case and best case are reported in Figure 4.41 and 4.42, respectively.

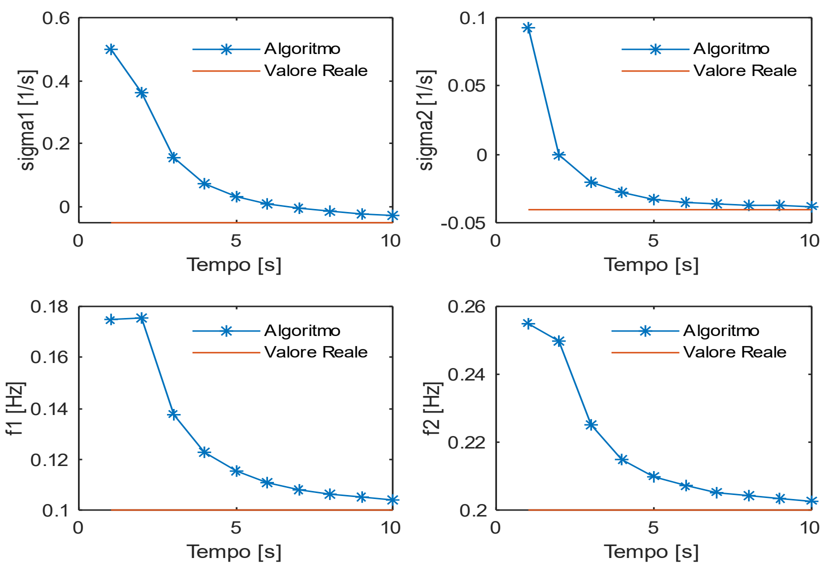

Figure 4-41 Estimates obtained with simulated quantization

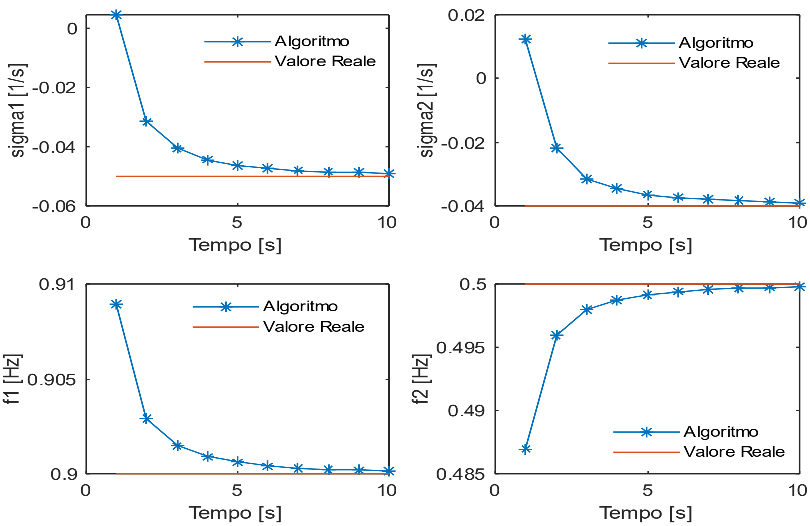

Figure 4-42 Estimates obtained with simulated quantization

4.4.7 One-component signal

In the case where the detected signal is mono-component, i.e., modeled by the equation:

$$y(t) = A \cdot e^{-\sigma \cdot t} \cdot \sin(2\pi f \cdot t + \varphi) \tag{4.10}$$

the proposed algorithm allows to detect all four parameters of interest (Figure 4.43).

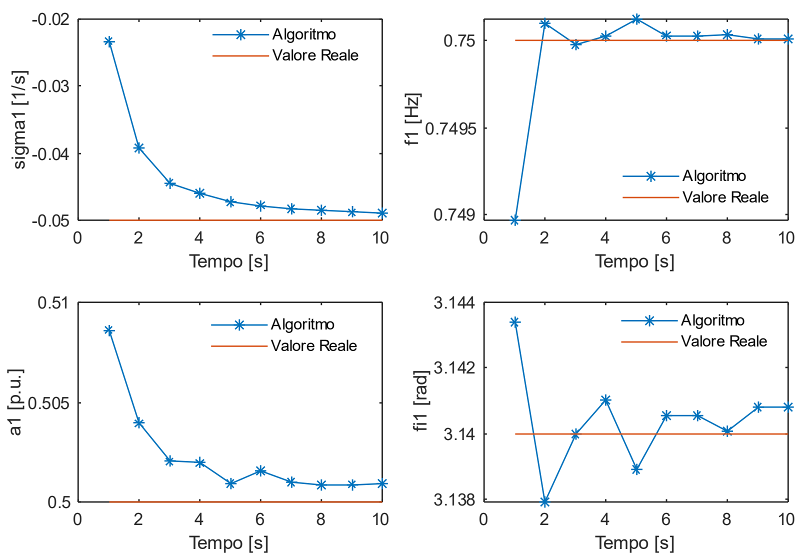

Figure 4-43 Estimates obtained in the case of a one-component signal

4.5 Experimental Tests

4.5.1 Description of the test network

In order to perform the validation of the proposed algorithm, it is necessary to refer to a test network. The model widely adopted for generating low frequency oscillations in literature is the four-machine, two-area Kundur model [19] (Figure 4.44)

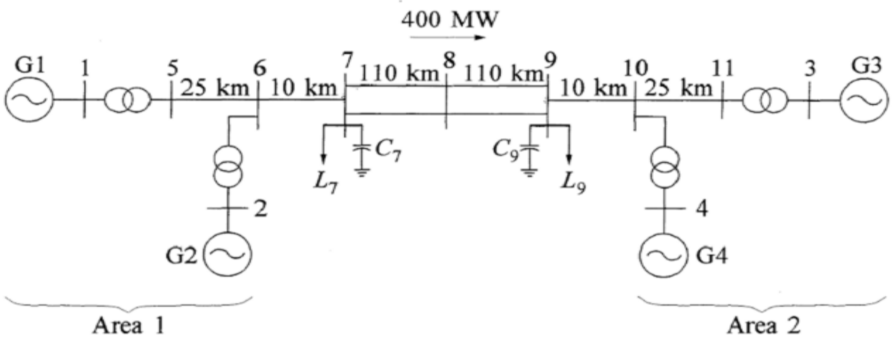

Figure 4-44 Test Network

The equivalent Simulink representation of the test network is reported in Figure 4.45.

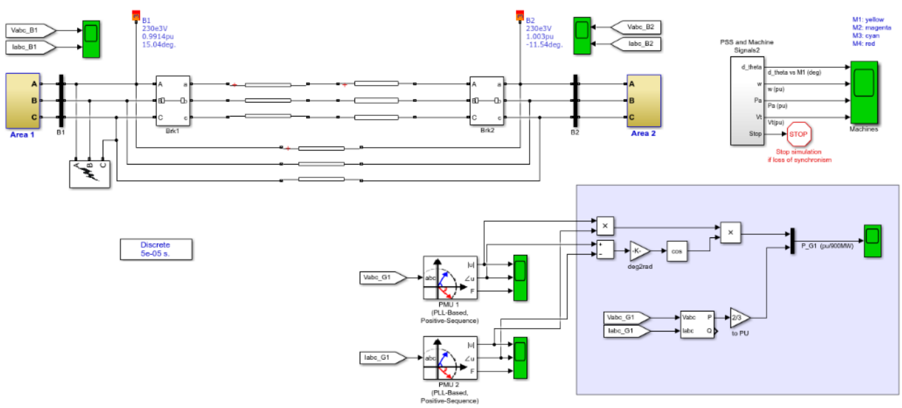

Figure 4-45 Representation Simulink network test

This network is composed by two areas, interconnected through a double three-phase HVAC line of nominal voltage 230 kV. Each area sees two properly controlled synchronous generators (of 900 MVA - 20 kV) and a load. Each generator receives the mechanical power P_m and the excitation voltage V_f by means of a system of turbines/regulators and an exciter/Pss, in which the frequency and voltage adjustments are made. The description of the control logic [1], incident on the

voltage and frequency parameters, is independent of the objective of this work and here is not addressed. .
Each step-up transformer has an impedance of 0 + j0.15 p.u. (taking 900 MVA and 20 kV as basic parameters). The transmission system has a nominal voltage of 230 kV and the line parameters, taking as a basis S = 100 MVA and V = 230 kV, are:

r=0.00001 p.u./km	x_W=0.001 p.u./km	b_C=0.00175 p.u./km

In order to simulate the perturbation, a self-extinguishing three-phase short circuit of 200 ms duration is generated.

Due to the computational time required by the MATLAB® platform, it is not possible to validate the algorithm online in a Simulink environment. Therefore, the analyses were carried out off line on the signal detected by the test network.

4.5.2 Results

Using a sampling rate of 50 Hz, results in the reconstruction shown in Figure 4.46a. Doubling the duration of the time window results in a reconstruction more faithful to the original signal (Figure 4.46b).

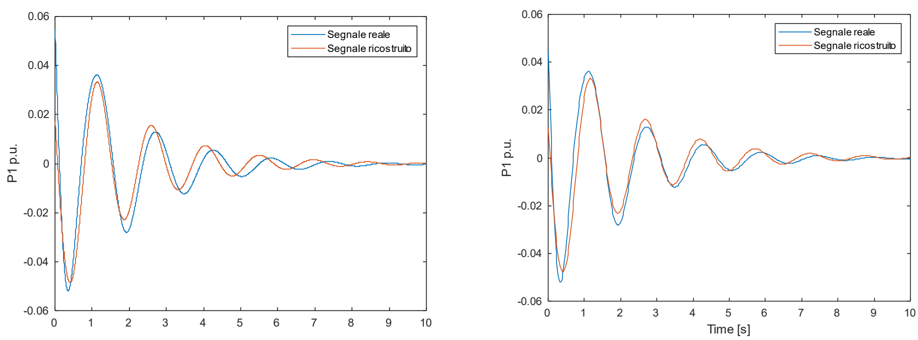

(a) (b)

Figure 4-46 Reconstruction after (a) 5 s and (b) 10 s

The mean square error, calculated on a ten-second window, exhibits the temporal trend shown in the Figure 4.47a. It is therefore deduced that as the observation time on which the PSO works increases, better results are obtained, that is, the $RMSE_{10}$ (calculated on a ten-second window) has a monotonous decreasing trend over time. It is also interesting to note the value of the RMSE at each iteration of the PSO ($RMSE_k$), calculated on the time window equal to that on which the PSO itself works. In this case it is observed how there is an anomaly in correspondence of a window equal to 1 s (Figure 4.47b).

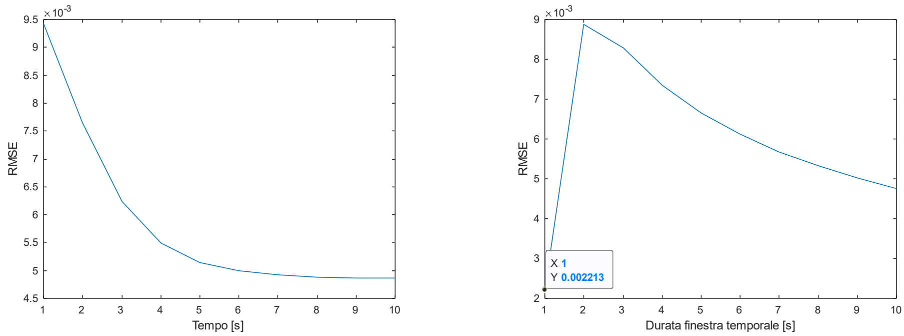

(a) (b)

Figure 4-47 (a) $RMSE_{10}$ calculated on a ten-second time window and (b) $RMSE_k$ as a function of time

The absence of monotony of the RMSE function, calculated on variable portions of the signal, is due to the fact that the optimization related to a one-second window produces different results than the optimization carried out on a window of longer duration (Figure 4.48). What therefore represents a local maximum of the RMSE, used as a fitness function of the PSO, is not actually an absolute maximum, where the concept of absolute is related to the maximum duration of the window (10 s).

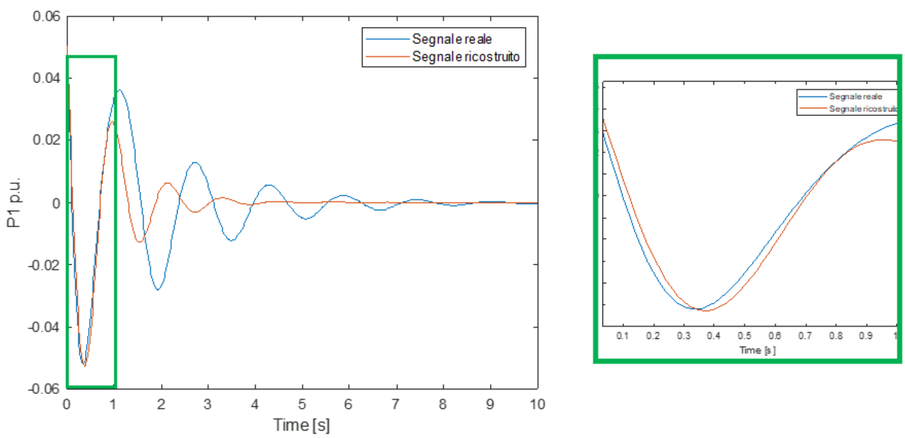

Figure 4-48 Reconstruction after 1s

4.6 Dinamic Mode Decomposition

4.6.1 Simulated tests

Two signals with the following characteristics are created in the MATLAB environment:

- f_1= 0.2 Hz; amplitude 0.5; positive damping
- f_2=0.3 Hz; amplitude 0.2; negative damping

The static DMD algorithm is deliberately required to identify 3 modes, aware that the third mode in this case does not exist. The algorithm's response is shown in Figure 4.49.

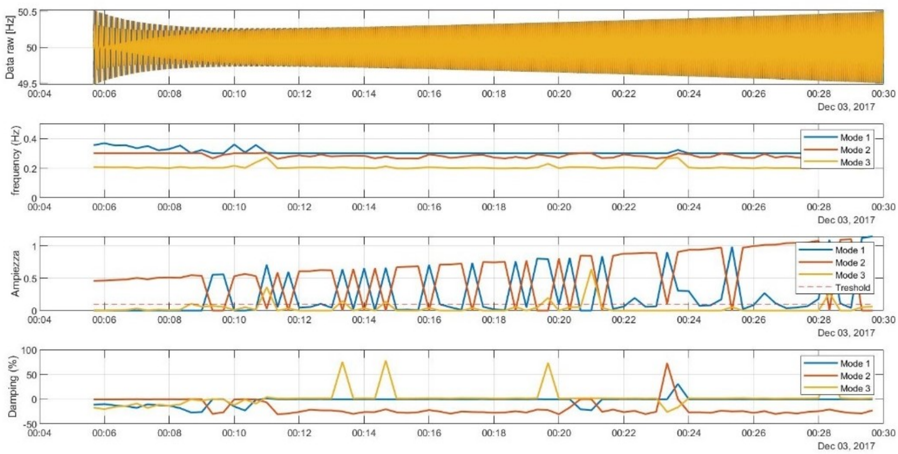

Figure 4-49 Static order DMD algorithm output with a simulated signal input

It is clear that the DMD responds to its inputs with extreme rigor, returning as requested, 3 modes even if they do not exist. The third mode, introduced by DMD is in fact almost superimposed on one of the two simulated, with a frequency slightly different from the 0.3 Hz created. In addition, the existence of two modes very close in frequency involves an anomaly in the detection of amplitudes (mode mixing) that are attributed alternately to one component or to the other mode, as shown by the third plot of Figure 4.49.
The result obtained with the same input signal, but using the dynamic order DMD algorithm is much better. As Figure 4.50 shows, the dynamic order is not forced to identify any non-existent mode, so the reliability in terms of faithful reproduction of real scenario is much higher. In addition, for the same reason, the algorithm is able to show when the first mode has become extinct, and does not present problems in the detection of amplitudes.

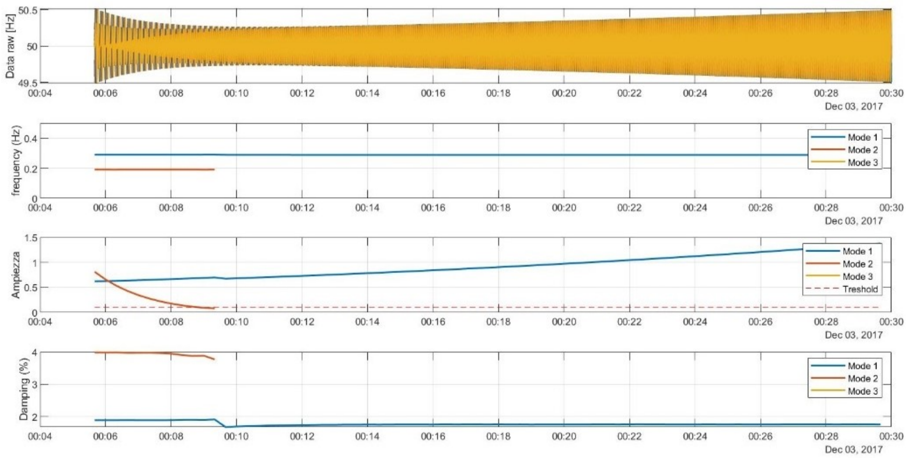

Figure 4-50 Output of the dynamic order DMD algorithm with a simulated signal input

Change in filter order

In signal theory, the phenomenon of spectral dispersion is known. Windowed signals and then transformed into Fourier series suffer errors in the spectrum due to the window itself. This happens for any digital signal, since samples are taken for finite time windows: mathematically it means having multiplied the signal by a function, through a convolution product [10]. In practice, spectral dispersion consists in dispersing the frequency, that is, detecting part of the signal power no longer concentrated at its nominal frequency but also distributed on secondary frequencies. It results in a spread frequency spectrum, which shows harmonic components in secondary lobes. In the present case, while not carrying out any Fourier analysis, but rather, using an algorithm that wants to be alternative to it, it is still a signal acquired for a reduced time interval and also filtered then windowed precisely through a digital filter that acts within the for cycle, filtering for each iteration 1000 samples, to eliminate the noise contained in it and to limit the output only to the frequencies of interest contained in the range (0.1 – 0.5 Hz).

Digital filters are special LTI (Linear Time-Invariant) discrete-time systems. The main ones used are the FIR (Finite Impulse Response) and IIR (Infinite Impulse Response) filters. In this case, a FIR filter was used. Technically, a FIR filter is a causal LTI system with finite impulse response:

---

[10]The convolution is an operation between two functions of a variable that consists in integrating the product between the first and second translated of a certain value

$$h(n) = 0 \text{ for } n < 0 \text{ and for } n \geq M \text{ with } M > 0 \tag{4.11}$$

whose transfer function turns out to be a polynomial in z^{-1}.
The input-output ratio is, in fact, described by the following equation:

$$y(n) = \sum_{k=0}^{M-1} h(k)x(n-k) \tag{4.12}$$

Turning to the z-transforms

$$Y(z) = H(z)X(z) \tag{4.13}$$

Where $X(z)$ and $Y(z)$ are the z-transforms of $x(n)$ and $y(n)$. $H(z)$ is a polynomial in z^{-1}:

$$H(z) = \sum_{k=0}^{M-1} h(k)z^{-k} \tag{4.14}$$

The digital filter used in this case is FIR type and is called Hilbert with a transfer function of the type:

$$H(z) = \frac{\sum_{k=0}^{M-1} b_k z^{-k}}{\sum_{k=0}^{M-1} a_k z^{-k}} \tag{4.15}$$

It was built in a MATLAB environment using the following commands:

```
% FILTRO HILBERT (TERNA)
m=[0,0,1,1,0,0];
f=[0,(segn.fh-segn.fb) * (2*segn.Ts1),
segn.fh*(2*segn.Ts1), segn.fl
*(2*segn.Ts1),(segn.fl+segn.fb)*(2*segn.Ts1),1];
segn.numeratore_filtro=firpm(segn.N,f,m,'hilbert');
```

The parameters m, f and N, define the numerator and denominator polynomials of equation (4.15). Then, with the command 'firpm' and the option 'Hilbert' are realized the characteristics of the required filter. In particular, the parameter N (in the script called segn.N because part of a structure), is the order of the digital filter or the order of the numerator polynomial. This parameter is very significant because it gives information on the accuracy with which the points that will describe the spectrum of the filter itself will be interpolated. As the order increases, the accuracy increases. For this reason, analyses were carried out as the order of the filter changed, focusing only on the ambient case with dynamic order. The Hilbert filter can cause the incorrect estimation of frequencies in the ambient case processed with dynamic order. To have a consistent and valid comparison, as the order of the filter changes, the length of the window considered in the iterations must be increased. It was chosen to keep constant the ratio:

$$\frac{filter\ order}{n°\ samples\ per\ window} \tag{4.16}$$

considering as base values: 600/1000=0.6. In practice, if the order of the filter is varied, the number of samples per window is determined accordingly through this ratio; the knowledge of the window samples and the sampling time allows to calculate the length of the window to be adopted.
In Fig. 4.51, the frequency response of three designed increasing-order filters is shown. The Figure shows the spectra of the filters, the basic one with order 600 (a), one with order 900 (b), and the other with order 1500 (c).

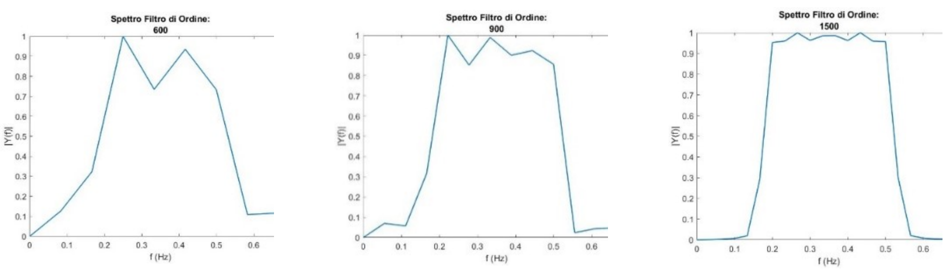

(a) (b) (c)

Figure 4-51 Spectrum of a Hilbert filter of order (a) 600, (b) 900 and (c) 1500

The improvement is evident: secondary lobes are reduced, frequencies outside the required range are not only attenuated but cut off totally.

As expected, as the filter order increases, the roll-off becomes narrower. Also, in Figure 4.51(a) and (b), the pass band ripple is greater than the 10%; as a consequence, frequencies around 0.3 Hz are attenuated and frequencies close to 0.2 Hz are amplified. This situation also no longer occurs in the 1500-order filter (Figure 4.51c).

4.7 Experimental Tests

To have a first clear scenario of the performance of the DMD algorithm, several traces of frequencies acquired through Terna's WAMS system in the two cases of static and dynamic order were tested.

- For the **static** order, a number of required modes equal to 3 is fixed, with the intent of displaying the 3 inter-area modes, North-South, East-West, East-Center-West.
- For the **dynamic** order, an energy threshold of 0.9 is imposed, i.e. the DMD is asked to identify the index of the first element that incorporates 90% of the energy in terms of the cumulative sum of the singular values, and to detect that number of modes of evolution accordingly.

Signals will be distinguished in:

1) *Transient*: signal characterized by a significant oscillation (Figure 4.52)

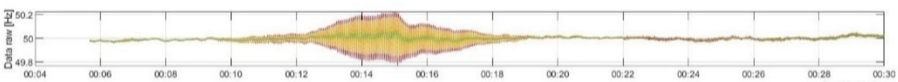

Figure 4-52 Transient signal

2) *Ambient:* signal characterized by the absence of oscillations or by very low amplitude random oscillations, due to the random change of the grid loads (Figure 4.53)

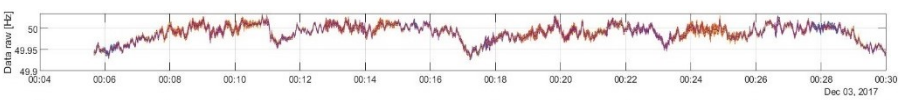

Figure 4-53 Ambient signal

4.7.1 Static order DMD

The static order algorithm is tested with 3 fixed modes, input of the DMD 'function', first for the transient signal and then for the ambient signal. The graphs obtained at the output are shown in the Figures 4.54 and 4.55.

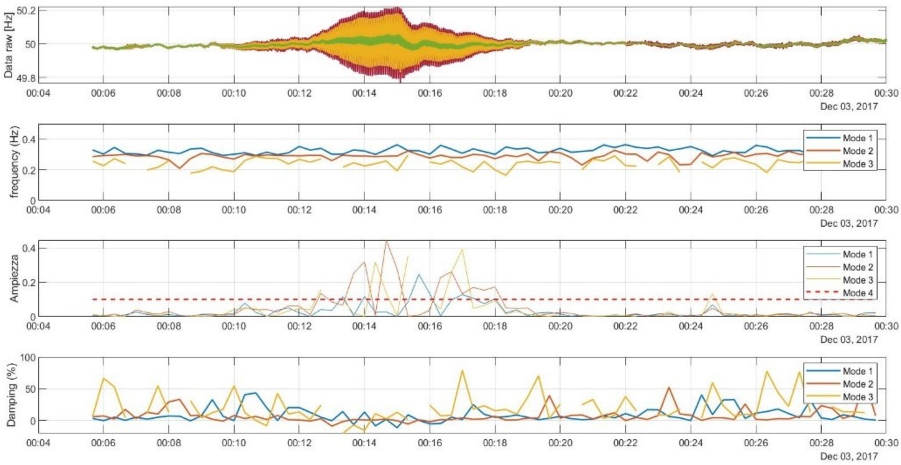

Figure 4-54 Static order DMD algorithm outputs with an input transient signal

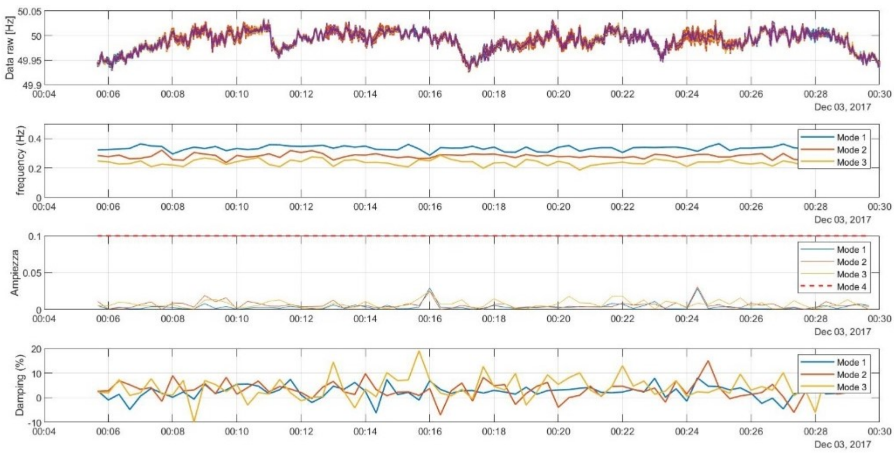

Figure 4-55 Static order DMD algorithm outputs with an ambient input signal

It is evident that in both cases, the 3 required modes described by the three different colours (red, yellow, blue) were returned. It can be noted that the oscillation that induces the activation of a trigger, in Figure 4.54 is well described by the increase in the amplitudes of the modes observed, in those moments, totally in contrast with the very low amplitudes detected instead in Figure 4.55, representing existing modes but their contribution to the signal energy is negligible.

4.7.2 Dynamic Order DMD

The dynamic order algorithm is tested, with a threshold set equal to 0.90, for both types of signal. The graphs obtained at the output are shown in the Figures 4.56 and 4.57. The results are extremely different from the Static Order DMD. In fact, the Dynamic Order algorithm returns (Figure 4.56) for a transient signal, a single mode with a frequency approximately equal to 0.3 Hz, and with a strongly increasing and then decreasing amplitude at the beginning of the emerging oscillation, and at its extinction. When considering the ambient signal, however, in Figure 4.57 the answer is ambiguous: it can be certainly detected one mode for the entire duration of the trace, the frequency of which is in the same range as that identified for the transient signal (close to 0.3 Hz); there are, then, some time intervals, for which the DMD also returns a second mode (red plot).

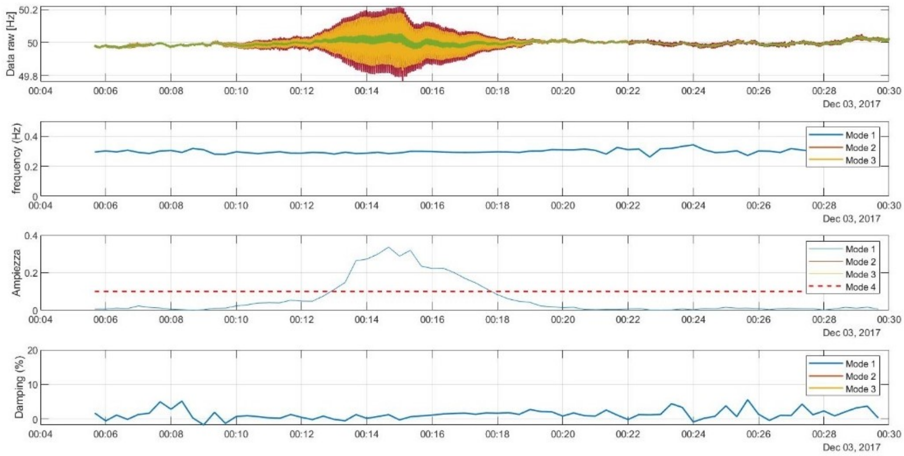

Figure 4-56 Dynamic order DMD algorithm outputs with an input transient signal

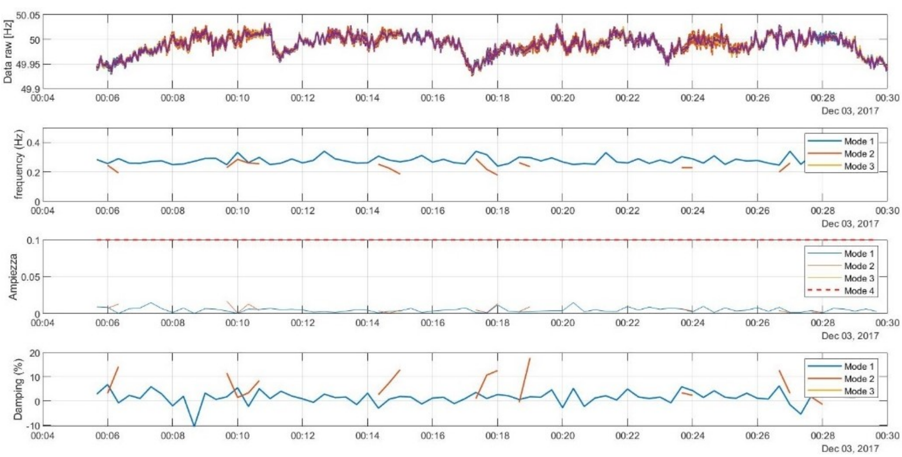

Figure 4-57 Dynamic order DMD algorithm outputs with an ambient input signal

A fundamental stage of the research activity was focused on the causes leading to the different results provided by the two approaches. Since the static order DMD detects three modes, it is important to understand if they are real existing modes or ficticious modes that the DMD provides because the algoritm has been set to detect three modes. Another questions regards the second mode detected by the dynamic order DMD in the ambient data. It has to be determined if that mode is truthful or whether it may be the effect of some undesired phenomenon such as spectral dispersion. To answer these questions an analysis regarding the variation of the filter order and a characterization of the signal in the frequency domain has been performed.

4.7.3 Filter Length Variation

Compared to what was done for Figure 4.57, the DMD algorithm was tested with filter length increased from order 600 and 900 (Figure 4.58).

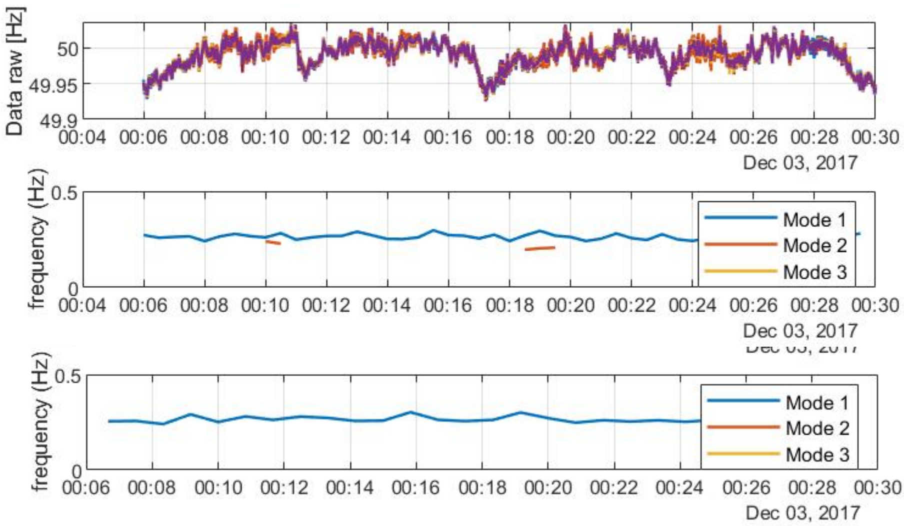

Figure 4-58 First estimate obtained with order filter 900 and second estimate obtained with order filter 1500

As the order of the filter increases, the result changes significantly: the presence of the second mode decreases until it disappears. This seems to show that the second mode does not exist, but that it is due to a spectral dispersion. A spectral analysis, using the FFT, is used to verify this result.

4.7.4 FFT Analysis

It was chosen to consider particularly significant cases, focusing on the trace parts of the signal in which the number of modes found varied, and placing itself downstream and upstream of this variation. The FFT analysis was conducted both before and after filtering. Note, that the time difference visible in the following Figures is due to the variability of the length of the window. The results are reported as the filter changes in Figure 4.59 and 4.60.

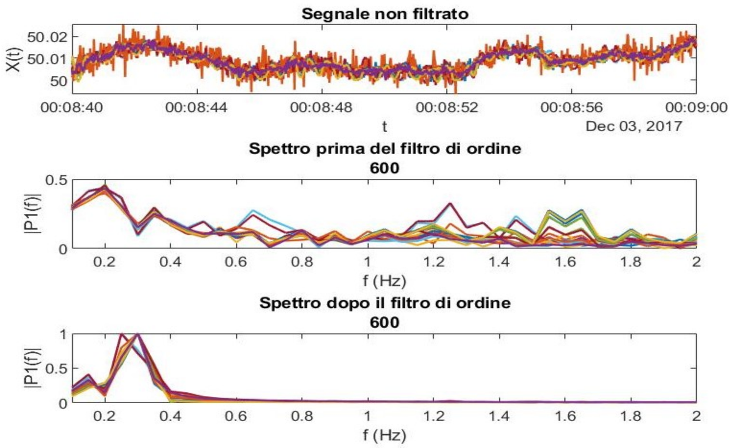

(a)

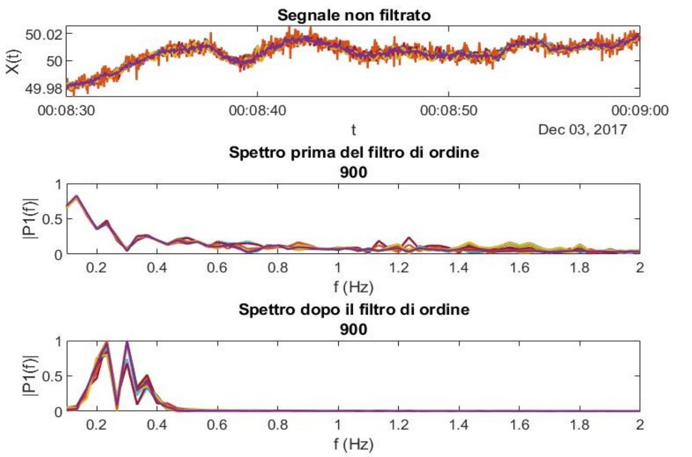

(b)

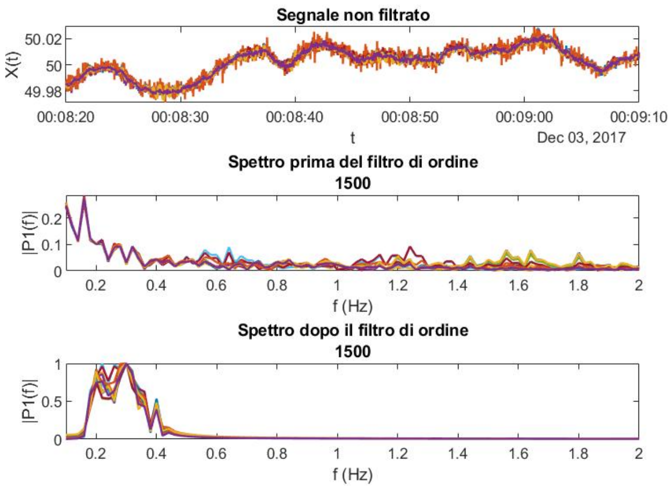

(c)

Figure 4-59 Frequency spectra of the ambient signal, before and after filtering for the stretch between 8 and 9 min, with filter of order (a) 600, (b) 900 and (c) 1500

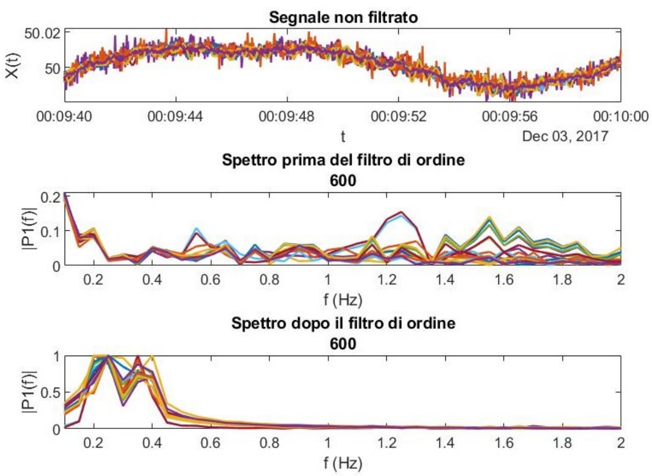

(a)

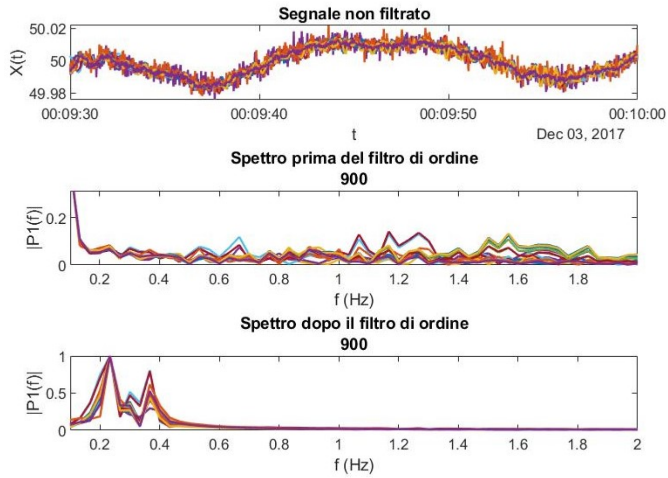

(b)

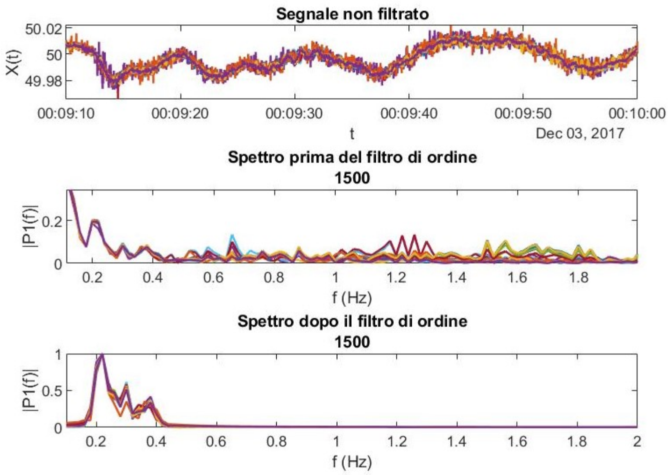

(c)

Figure 4-60 Frequency spectra of the ambient signal, before and after filtering for the time window between 9 and 10 min., with filter of order (a) 600, (b) 900 and (c) 1500

It is not feasible to recognize significant components by observing the spectrum of the raw data, without a proper filter. When the filter is applied, it is possible, with proper zooming, to detect in the part of interest (0.1 -0.4 Hz) three frequency peaks that are then clearly evident and readable in the spectrum. The Figure 4.60c is of particular interest because it concerns the case with filtering at order 1500, thus the one that when used in the DMD algorithm returned only one mode for the entire duration of the trace, leading the operator into the mistake of believing that there was only one mode in the processed signal.

Note, however, that the amplitude of this mode reaches almost unity (the amplitudes are normalized with respect to the maximum value), thus a considerable value that may in a certain way have contributed to the obscuration of the other frequencies with much smaller amplitudes.

4.7.5 Change in the dynamic order detection threshold

As already explained, the dynamic order is performed downstream of the SVD, by means of a condition on the cumulative sum of the singular values of the matrix S. In Figure 4.61 is reported a section of the MATLAB code that determines the dynamic order.

```
%% Calcolo SVD
[U,S,V] = svd(X1,'econ');

 %energies = diag(S).^2;
        cdS = cumsum(diag(S))./sum(diag(S)); % Cumulative energy
        dmd_ord = find(cdS>lim, 1 ); % Find r to capture lim% energy

        if dmd_ord-round(dmd_ord/2)*2 < 0
            dmd_ord=dmd_ord+1; % per avere un rango pari
        end

        if dmd_ord < dmd_ord_min % evito di settare rango<2
            dmd_ord=dmd_ord_min;
        elseif dmd_ord>size(S,1)
            dmd_ord=size(S,1);
        end

        Ur = U(:,1:dmd_ord);
        Sr = S(1:dmd_ord,1:dmd_ord);
        Vr = V(:,1:dmd_ord);
```

Figure 4-61 Section of MATLAB code that determines dynamic order

The parameter 'lim' had been chosen equal to 0.90, with the hypothesis that this threshold could be a good compromise between the not excessive computational overload and the necessity of detecting the modes characterizing the system. After the FFT analysis, in which the existence of the 3 modes is highlighted, it is believed that the modes identified by the DMD algorithm in static order are real and existing. This means that the dynamic order did not show the other two components, because the first component reaches the set energy threshold; the remaining part of the signal is, then, discarded. Therefore, an optimal tuning of the energy threshold was carried out, making it vary in the range between 0.90 to 0.97. As it can be seen the number of estimated modes increases. As the energy threshold increases even by only 0.02, the second mode becomes more visible and, furtherly increasing the threshold, the third mode also appears. In the Figure 4.62 are reported three examples, with 3 different thresholds, with the ambient signal input and a filter order of 600 and

1500.

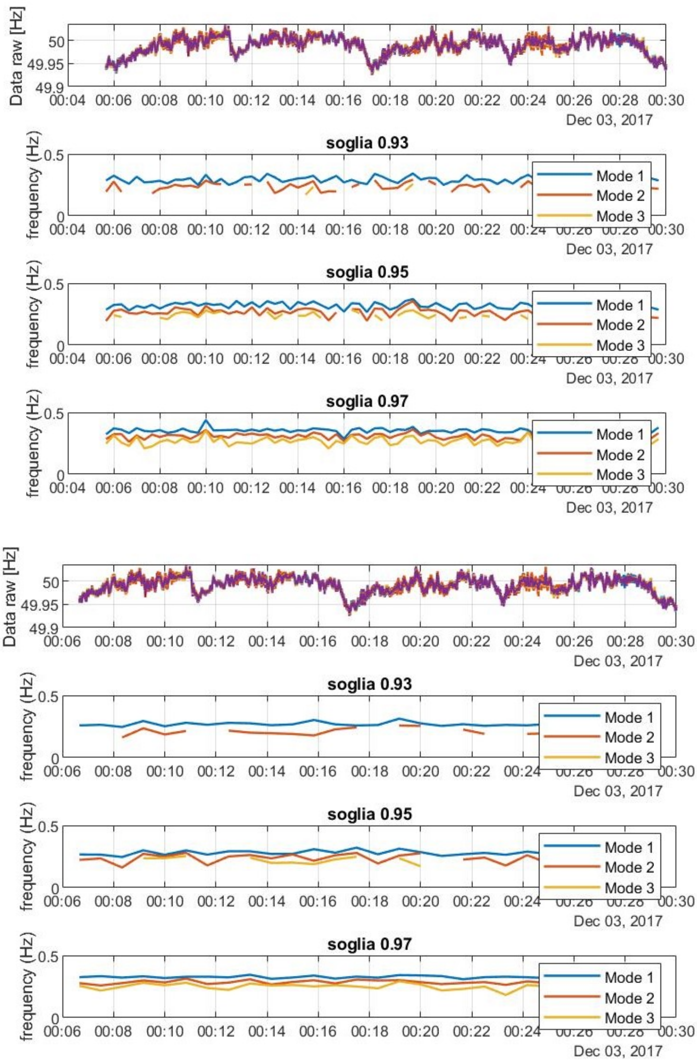

(a)

(b)

Figure 4-62 Modes detected when the threshold determining the dynamic order changes, with an order filter of (a) 600 and (b) 1500

There are differences in the accuracy of frequency detection, attributable to the different length of the considered window.
Finally, as a further test, the algorithm has been assessed with a signal given by the union of the ambient and transient signal considered in the previous tests.The test is performed as the threshold changes and the results obtained are reported in Figure 4.63.

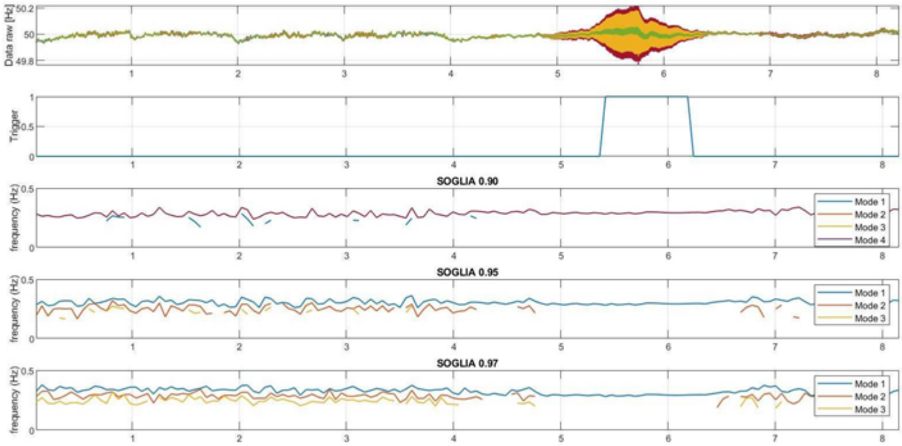

Figure 4-63 Frequency detection with dynamic order DMD algorithm as the threshold changes

The result is surprising: the dynamic order DMD algorithm turns out to dynamically identify the modes contained in the reference signal, depending on whether or not it consists of modes of excited evolutions. In fact, in the so-called trigger area, i.e., between the activation of the trigger and the extinction of the excited mode, it somewhat selects the excited mode by virtue of its property that binds it to the energy threshold. As the amplitude of that mode increases, the order of magnitude of the singular value associated with it varies accordingly, and for that reason, it quickly reaches the imposed energy threshold. From an application point of view, the dynamic order is extremely useful since it can return all the modes identified by the static order without having to doubt their actual existence, provided an appropriate threshold is chosen, and it is also capable of varying the number of modes identified, the moment that dangerous oscillations occur. This means that, in real time, one can visually and promptly see when a mode is increasing its energy and thus when the National Electric System begins to approach an unstable point, and if necessary intervene promptly. To conclude, the value 0.95 is chosen as the new threshold 'lim' and the output of the DMD algorithm is returned to dynamic order complete with amplitude and damping parameters (Figure 4.64).

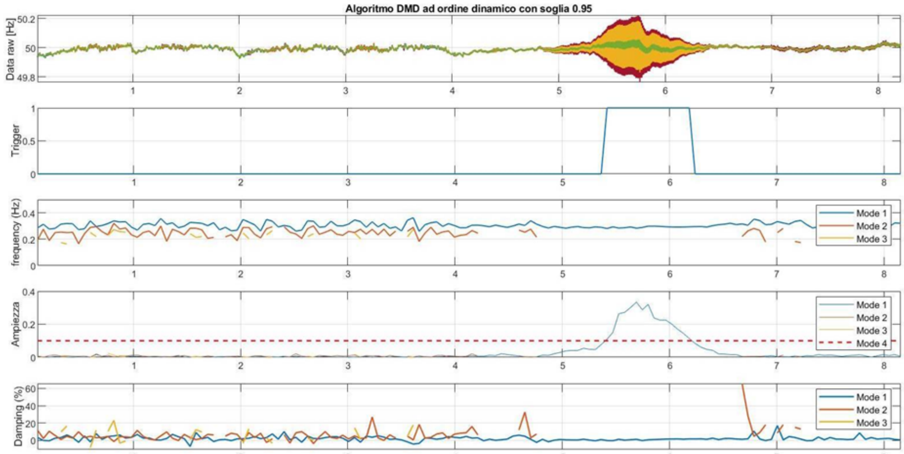

Figure 4-64 Dynamic Order DMD algorithm with threshold 0.95

4.8 Tufts Kumaresan

For the assessment of TK algorithm, the sampling rate is a fixed parameter as it depends on the PMUs that acquire data from the network, while the variable parameters of the algorithm are:

- The number of acquired samples (*N*) that varies according to the time width of the processed window *Tw*;
- *L* (order of the prediction filter) which is usually chosen equal to half the number of samples N;
- *K* (the energy threshold) that allows to distinguish the signal modes from not significant components due to noise.

In the algorithm there is also another parameter, L_1, which has no real meaning for the purposes of the method, in fact, it is inserted for the purpose of making the algorithm more dynamic. Starting from the assumption of not knowing how many modes "*M*" the signal has, the algorithm provides two phases:

- In the first phase, fixed *K* and the length of the acquired window, and then *N*, the Hankel matrix and the vector *h* to find the vector *b* of the prediction coefficients backwards are constructed. Being signals corrupted by noise, the SVD is applied to the Hankel matrix, which returns the values of "sigma", which are used to estimate, together with the chosen *K*, the possible number of signal modes (*Ms*). In order to take the elements corrupted by noise, L_1 is imposed at a value close to *L* (i.e. equal to 80%) and the standard deviation of noise is calculated as the average of sigma values ranging from L_1 to *L*. The estimate of *Ms* is then determined by adding all those values (K.*estimated noise) that are greater than sigma.

- In the second phase, once estimated *Ms*, *L* is set equal to *Ms*; again, as in the first phase, the equation to find the signal zeros of the polynomial *B(z)* is solved and the parameters of interest are calculated: amplitude, phase, frequency and damping.
- In the various tests carried out, a number of estimated modes (Ms) greater than the actual ones will be notice. So a filtering technique, for discarding the noisy found components, is used. The amplitudes will be ordered in a descending way, that is, the components characterized by greater amplitude, which corresponds to a greater energy threshold, will be arranged before the others; moreover, among the detected components, the algorithm will select only that characterized by the frequencies ranging from 0 to 0.8 Hz, that are typical values associated with inter-area oscillations.

4.8.1 Simulated tests

In order to assess the accuracy of parameter estimation of a synthetic signal, the generic model with M exponentially damped sinusoids corrupted by a white Gaussian noise of value w(n) was chosen:

$$y(n) = \sum_{k=1}^{M} a_k e^{s_k n} + w(n) \quad n = 0,1,..,N-1 \qquad (4.17)$$

Where a_k are the amplitudes, $s_k = -\sigma_k + j2\pi f_k \quad K = 1,2,..,\mathrm{M}$, σ_k is the damping and f_k frequency.

The tests will be performed on a synthetic signal with *M* equal to 1, 2 and 3 and as the parameters *K, N, L* vary; then the SNR will be varied to evaluate the robustness of the method, after which the relative percentage error will be determined, which is defined as follows:

$$errore_{\%} = \frac{\hat{x} - x}{x} \cdot 100 \qquad (4.18)$$

Where $\hat{x}$ is the estimated parameter and x is the real parameter.

<u>TEST 1)</u> The signal composed of only one mode (***M = 1***) and with **SNR = 80 dB** has:

- $f_1 = 0.33$ Hz;

- $\sigma_1 = -0.002$;
- $a_1 = 0.01$.

The time evolution of this signal is shown in the Figure 4.65.

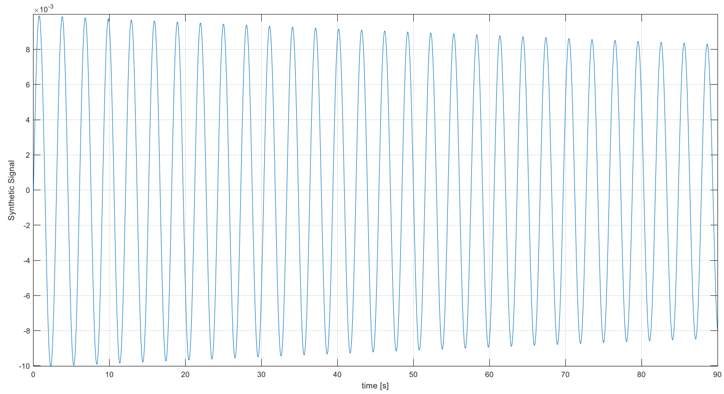

Figure 4-65 Signal trend with M = 1, SNR = 80 dB.

The Table 4.8 shows the various tests carried out, keeping the *L* equal to half the number of N samples and varying:

- The window, *Tw,* from a minimum of 10 s to a maximum of 150 s;
- The parameter *K* set equal to 1, 5, and 7.

Table 4.8 Estimated values for the synthetic signal with M = 1

MODE 1 (L = N/2) SNR = 80 dB		σ ESTIMATED	f ESTIMATED	a ESTIMATED	error% (f)	error% (σ)	error% (a)	Ms
K=1	Tw=10	-0.0020	0.3300	0.0100	0	0	0	228 (1)
	Tw=20	-0.0020	0.3300	0.0100	0	0	0	449
	Tw=40	-0.0020	0.3300	0.0099	0	0	1	910
	Tw=90*	-0.0020	0.3300	0.0098	0	0	2	2041
	Tw=150*	-0.0020	0.3300	0.0097	0	0	3	3384
K=5	Tw=10*	-0.0020	0.3300	0.0100				65 (1)
	Tw=20*	-0.0020	0.3300	0.0100				198 (3)
	Tw=40*	-0.0020	0.3300	0.0099				332
	Tw=90*	-0.0020	0.3300	0.0098				783
	Tw=150	-0.0020	0.3300	0.0097				1241
K=7	Tw=10*	-0.0020	0.3300	0.0100				20 (1)
	Tw=20	-0.0020	0.3300	0.0100				88 (1)
	Tw=40	-0.0020	0.3300	0.0099				116 (2)
	Tw=90*	-0.0020	0.3300	0.0098				278
	Tw=150	-0.0020	0.3300	0.0097				399

It is noted, from the reported data, that the frequency estimation and damping do not present any percentage error for any value of K and Tw, while the amplitude estimate has an error that varies from 1 to 3% as the window increases. As K changes, on the other hand, there is an improvement in the estimation of *Ms*, since with a value greater than K the most significant modes are taken.

<u>TEST 2)</u> Test signal with two modes *(M = 2)* and with **SNR = 80 dB**:

- $f_1 = 0.2$ Hz $f_2 = 0.3$ Hz;
- $\sigma_1 = -0.001 \quad \sigma_2 = 0.0003$;
- $a_1 = 0.001 \quad a_2 = 0.002$.

The time evolution of this signal is shown in the Figure 4.66.

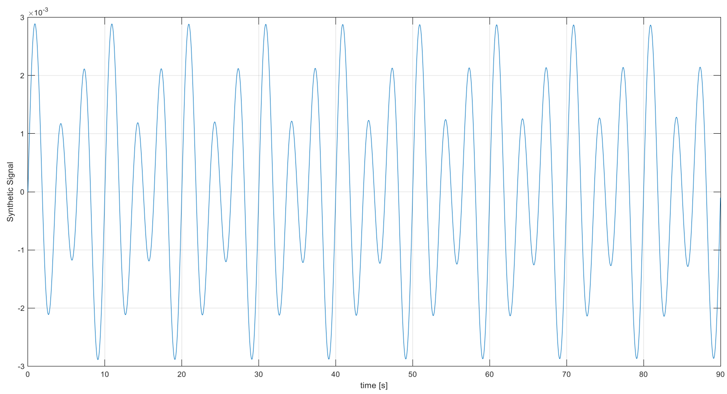

Figure 4-66 Signal trend with M = 2, SNR = 80 dB

The Table 4.9 shows, in the same way as in mode 1, the tests carried out.

It can be seen, from the reported data, that the frequency estimation and damping do not present any relative percentage error, except in the case of K = 7 and K = 5 for a window of 10 s, while the amplitude estimate has a small error.

Table 4.9 Estimated values for the synthetic signal with M = 2

MODE 2 (L = N/2) SNR = 80 dB		σ ESTIMATED	f ESTIMATED	a ESTIMATED	error% (σ)	error% (f)	error% (a)	Ms
K=1	Tw=10	0.0003 -0.0010	0.3000 0.2000	0.0020 0.0010	0	0	0	227
	Tw=20	0.0003 -0.0010	0.3000 0.2000	0.0020 0.0010	0	0	0	450
	Tw=40	0.0003 -0.0010	0.3000 0.2000	0.0020 0.0010	0	0	0	912
	Tw=90	0.0003 -0.0010	0.3000 0.2000	0.0021 0.0009	0	0	5 10	2039
	Tw=150	0.0003 -0.0010	0.3000 0.2000	0.0021 0.0008	0	0	5 20	3383
K=5	Tw=10*	0.0002 -0.0006	0.3000 0.2000	0.0020 0.0010	33.33 X	0	0	67 (2)
	Tw=20	0.0003 -0.0010	0.3000 0.2000	0.0020 0.0010	0	0	0	199 (3)
	Tw=40	0.0003 -0.0010	0.3000 0.2000	0.0020 0.0010	0	0	0	324
	Tw=90	0.0003 -0.0010	0.3000 0.2000	0.0021 0.0009	0	0	5 10	786
	Tw=150*	0.0003 -0.0010	0.3000 0.2000	0.0021 0.0008	0	0	5 20	1237
K=7	Tw=10*	0.0267 0.7725	0.2946 0.1716	0.0021 0.0035	X	1.8 14.2	5 X	19 (2)
	Tw=20	0.0003 -0.0009	0.3000 0.2000	0.0020 0.0010	0 10	0	0	93 (2)
	Tw=40	0.0003 -0.0010	0.3000 0.2000	0.0020 0.0010	0	0	0	110 (2)
	Tw=90	0.0003 -0.0010	0.3000 0.2000	0.0021 0.0009	0	0	5 10	281
	Tw=150	0.0003 -0.0010	0.3000 0.2000	0.0021 0.0009	0	0	5 10	400

TEST 3) The signal with three modes *(M = 3)* and with **SNR = 80 dB**:

- $f_1 = 0.1$ Hz $f_2 = 0.2$ Hz $f_3 = 0.3$ Hz;
- $\sigma_1 = -0.0004 \quad \sigma_2 = -0.001 \quad \sigma_3 = 0.0006$;
- $a_1 = 0.0001 \quad a_2 = 0.01 \quad a_3 = 0.002$.

It has the trend shown in the Figure 4.67.

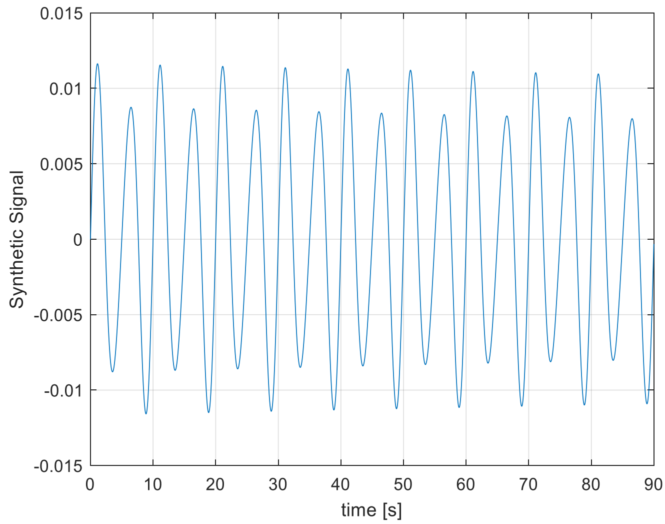

Figure 4-67 Signal trend with M = 3, SNR = 80 dB

The Table 4.10 shows, always in the same way, the tests carried out.

Table 4.10 Estimated values for the synthetic signal with M = 3

MODE 3 (L = N/2) SNR=80dB		**σ** ESTIMATED	**f** ESTIMATED	**a** ESTIMATED	error% (σ)	error% (f)	error% (a)	Ms
		0.0584	0.0842	0.0001	X	15.80	0	
	Tw=10	-0.0014	0.2001	0.0100	40	0.05	0	228
		0.0012	0.2999	0.0020	X	0.03	0	
		-0.0003	0.1000	0.0001	25		0	
	Tw=20	-0.0010	0.2000	0.0100	0	0	0	450
		0.0006	0.3000	0.0020	0		0	
		-0.0004	0.1000	0.0001			0	
K=1	Tw=40	-0.0010	0.2000	0.0099	0	0	1	912
		0.0006	0.3000	0.0021			0	
		-0.0004	0.1000	0.0001			0	
	Tw=90	-0.0010	0.2000	0.0100	0	0	0	2039
		0.0006	0.3000	0.0021			0	
		-0.0004	0.1000	0.0001			0	
	Tw=150	-0.0010	0.2000	0.0096	0	0	4	3383
		0.0006	0.3000	0.0023			X	

		-	-	-	-	-	-	
	Tw=10*	-0.0003	0.2001	0.0099	X	0.05	1	68
		-0.0004	0.2994	0.0020	33	0.2	0	
		0.0209	0.0992	0.0001	?	0.8	0	
	Tw=20	-0.0011	0.2000	0.0100	?	0	0	199
		0.0006	0.3000	0.0020	0	0	0	
		-0.0002	0.10000.2000	0.0001	X		0	
K=5	Tw=40	-0.0010	0.3000	0.0100	0	0	0	324
		0.0006		0.0020	0		0	
		-0.0004	0.1000	0.0001			0	
	Tw=90	-0.0010	0.2000	0.0099	0	0	1	777
		0.0006	0.3000	0.0021			5	
		-0.0004	0.1000	0.0001			0	
	Tw=150	-0.0010	0.2000	0.0099	0	0	1	1227
		0.0006	0.3000	0.0022			10	
		-	-	-	-	-	-	
	Tw=10*	0.0157	0.2032	0.0100	X	1.6	0	20
		1.0679	0.2633	0.0069	X	12.23	X	
		-	-	-	-	-	-	
	Tw=20	-0.0009	0.2001	0.0099	10	0.05	1	92
		0.0008	0.2998	0.0020	X	0.06	2	
		-	-	-	-	-	-	
K=7	Tw=40	-0.0011	0.2000	0.0100	0	0	0	110
		0.0011	0.2999	0.0021	X	0.03	5	
		0.0023	0.1001	0.0001	X	0.1	0	
	Tw=90	-0.0010	0.2000	0.0100	0	0	0	280
		0.0006	0.3000	0.0021	0	0	5	
		-0.0004	0.1000	0.0001			0	
	Tw=150	-0.0010	0.2000	0.0099	0	0	1	393
		0.0006	0.3000	0.0022			10	

It is noted, from the reported data, that there is a good estimate of both frequency and damping, except for some cases that have been deliberately selected to stress the algorithm and evaluate its performance. The parameter that has a greater deviation from its reference value is certainly the amplitude, but it must be considered that the frequencies under consideration are very close to each other and, consequently, the damping and amplitude values are really small numbers; therefore, it can be said that the TK method exhibits notable performance for estimating the oscillation parameters.

In addition, to evaluate the actual weight that L has on the estimation of the parameters of our interest, it is equal to N/10, even if in previous tests it had been chosen equal to N/2, as reported by the studies carried out by Tufts Kumaresan. The tests performed on the signals with M = 1 and M = 3 and evaluated for both L equal to N/2 and N/10 were compared and reported in the Tables 4.11 and 4.12.

Table 4.11 Estimated values for the synthetic signal with M =1 and varying L

MODE 1 SNR=80dB			**σ** ESTIMATED	**f** ESTIMATED	**a** ESTIMATED	Ms
K=1	Tw=20	L=N/10	-0.0020	0.3300	0.0096	90
		L=N/2	-0.0020	0.3300	0.0096	449
	Tw=90	L=N/10	-0.0020	0.3300	0.0083	412
		L=N/2	-0.0020	0.3300	0.0082	2041
	Tw=150	L=N/10	-0.0020	0.3300	0.0082	2041
		L=N/2	-0.0020	0.3300	0.0071	3384
K=5	Tw=20	L=N/10	-0.0004	0.3300	0.0097	3
		L=N/2	-0.0020	0.3300	0.0096	198
	Tw=90	L=N/10	-0.0016	0.3300	0.0085	3
		L=N/2	-0.0020	0.3300	0.0082	783
	Tw=150	L=N/10	-0.0017	0.3300	0.0075	3
		L=N/2	-0.0020	0.3300	0.0072	1241
K=7	Tw=20	L=N/10	-0.0004	0.3300	0.0097	3
		L=N/2	-0.0020	0.3300	0.0096	88
	Tw=90	L=N/10	-0.0016	0.3300	0.0085	3
		L=N/2	-0.0020	0.3300	0.0083	278
	Tw=150	L=N/10	-0.0017	0.3300	0.0075	3
		L=N/2	-0.0020	0.3300	0.0073	399

Table 4.12 Estimated values for the synthetic signal with M = 3 and varying L

WAY 3 SNR=80dB		Tw=20		Tw=90		Tw=150	
		L=N/10	L=N/2	L=N/10	L=N/2	L=N/10	L=N/2
K=1	σ ESTIMATED	- -0.0009 0.0008	-0.0003 -0.0010 0.0006	-0.0004 -0.0010 0.0006	-0.0004 -0.0010 0.0006	-0.0004 -0.0010 0.0006	-0.0004 -0.0010 0.0006
	f ESTIMATED	- 0.2001 0.2998	0.1000 0.2000 0.3000	0.1000 0.2000 0.3000	0.1000 0.2000 0.3000	0.1000 0.2000 0.3000	0.1000 0.2000 0.3000
	a ESTIMATED	- 0.0098 0.0020	0.0001 0.0098 0.0020	0.0001 0.0021 0.0021	0.0001 0.0092 0.0021	0.0001 0.0085 0.0022	0.0001 0.0083 0.0023
	Ms	90	450	411	2039	693	3383
K=5	σ ESTIMATED	0.0014	0.0209 -0.0011 0.0006	- 0.0144 -	-0.0004 -0.0010 0.0006	- 0.0167 -	-0.0004 -0.0010 0.0006
	f ESTIMATED	0.2049	0.0992 0.2000 0.3000	- 0.2066 -	0.1000 0.2000 0.3000	- 0.2073 -	0.1000 0.2000 0.3000
	a ESTIMATED	0.0099	0.0001 0.0098 0.0020	- 0.0087 -	0.0001 0.0091 0.0021	- 0.0065 -	0.0001 0.0085 0.0022
	Ms	5	199	5	777	7	1227
K=7	σ ESTIMATED	0.0014	- -0.0009 0.0008	- 0.0144 -	0.0023 -0.0010 0.0006	- 0.0167 -	-0.0004 -0.0010 0.0006
	f ESTIMATED	0.2049	- 0.2001 0.2998	- 0.2066 -	0.1001 0.2000 0.3000	- 0.2073 -	0.1000 0.2000 0.3000
	a ESTIMATED	0.0099	- 0.0098 0.0020	- 0.0087 -	0.0001 0.0091 0.0021	- 0.0065 -	0.0001 0.0086 0.0022
	Ms	5	92	5	280	7	393

It is noted that the estimates of the parameters for L equal to N/10 worsen considerably, this is related to the fact that the Hankel matrix, imposing that value of L, is excessively reduced and does not allow a proper estimation of the signal components.

Incidence of noise

High noise levels could seriously affect the performance of the estimation algorithm, therefore a dedicated analysis must be performed to analyse the response with respect to different signal-to-noise ratio levels. In particular, the results reported here refer to an addition of white Gaussian noise to the signal through a value of **SNR = 50dB**, a classic noise associated with the quantization of measurement instrumentation.

The test will be carried out on the signal with $M = 1,2,3$, K and Tw variable and a L fixed at $N/2$.

TEST 1) Signal with $\boldsymbol{M = 1}$

There is no relevant variation. For M = 1 the algorithm is robust against noise with an SNR = 50dB.

TEST 2) Signal with $\boldsymbol{M = 2}$

The trend is shown in the Figure 4.68 and the estimated values are reported in Table 4.13.

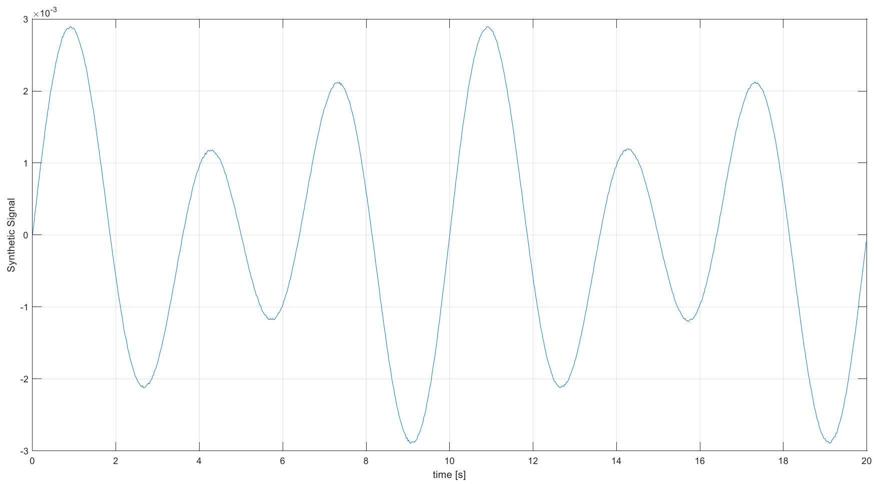

Figure 4-68 Signal trend with M = 2 and SNR = 50dB

Table 4.13 Estimated values for the synthetic signal with M = 2 and SNR = 50dB

MODE 2 L=N/2			σ ESTIMATED	f ESTIMATED	a ESTIMATED	Ms
K=1	Tw=20	SNR=50dB	0.0002-0.0011	0.3000- 0.2000	0.0020 o.oo10	450
		SNR=80dB	0.0003-0.0010	0.3000- 0.2000	0.0020 0.0010	
	Tw=90	SNR=50dB SNR=80dB	0.0003-0.0010	0.3000 0.2000	0.0021 0.0009	2039
	Tw=150	SNR=50dB SNR=80dB	0.0003 -0.0010	0.3000 0.2000	0.0021 0.0008	3383
K=5	Tw=20	SNR=50dB SNR=80dB	0.0003 -0.0008 0.0003 - 0.0010	0.3000 0.2000	0.0020 0.0010	199
	Tw=90	SNR=50dB SNR=80dB	0.0003 -0.0010	0.3000 0.2000	0.0021 0.0009	786
	Tw=150	SNR=50dB SNR=80dB	0.0003 -0.0010	0.3000 0.2000	0.0021 0.0008	1237
K=7	Tw=20	SNR=50dB	0.0002 0.0020 0.0003 - 0.0009	0.3000 0.2001	0.0020	92
		SNR=80dB		0.3000 0.2000	0.0010	93
	Tw=90	SNR=50dB SNR=80dB	0.0003-0.0010	0.3000 0.2000	0.0021 0.0009	281
	Tw=150	SNR=50dB SNR=80dB	0.0003-0.0010	0.3000 0.2000	0.0021 0.0009	400

For each value of K, the window equal to 20 s has only a small variation on the value of the damping, so, even for the signal with M = 2, the method can be considered robust against noise.

<u>**TEST 3)**</u> Signal with **M = 3**

The trend is shown in the Figure 4.69 and the estimated values are reported in Table 4.14.

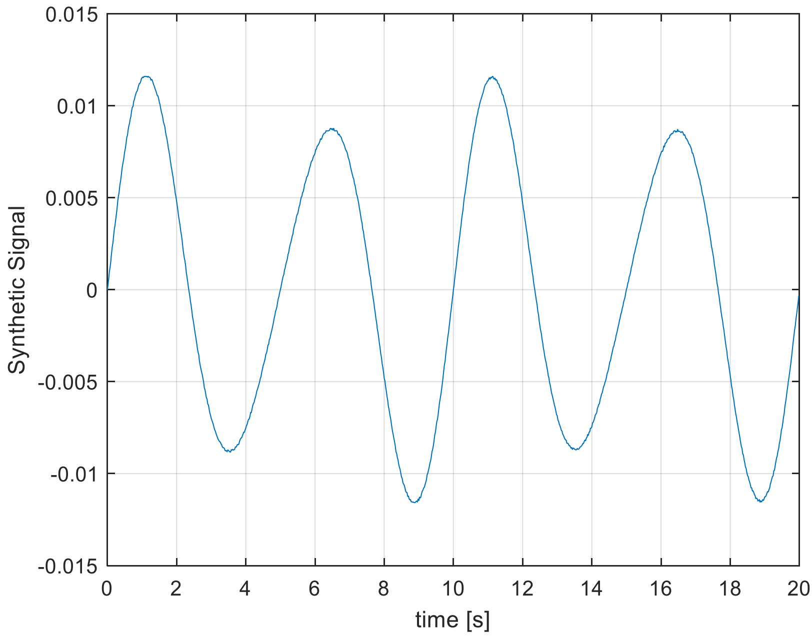

Figure 4-69 Signal trend with M = 3 and SNR = 50dB

Table 4.14 Estimated values for the synthetic signal with M = 3 and SNR = 50dB

WAY 3		Tw=20		Tw=90		Tw=150	
L=N/2		SNR=50dB	SNR=80dB	SNR=50dB	SNR=80dB	SNR=50dB	SNR=80dB
K=1	σ **ESTIMATED**	0.0031 -0.0010 0.0003	-0.0003 -0.0010 0.0006	-0.0010 -0.0010 0.0006	-0.0004 -0.0010 0.0006	-0.0005 -0.0010 0.0006	-0.0004 -0.0010 0.0006
	f **ESTIMATED**	/	0.1000 0.2000 0.3000	0.1001 0.2000 0.3000	0.1000 0.2000 0.3000	/	0.1000 0.2000 0.3000
	a **ESTIMATED**	/	0.0001 0.0098 0.0020	/	0.0001 0.0092 0.0021	/	0.0001 0.0083 0.0023
	Ms	/	450	/	2039	/	3383
K=5	σ **ESTIMATED**	- -0.0014 0.0015	0.0209 -0.0011 0.0006	-0.0005 -0.0010 0.0006	-0.0004 -0.0010 0.0006	-0.0008 -0.0010 0.0006	-0.0004 -0.0010 0.0006

	f ESTIMATED	- 0.2001 0.2999	0.0992 0.2000 0.3000	0.1001 0.2000 0.3000	0.1000 0.2000 0.3000	/	0.1000 0.2000 0.3000
	a ESTIMATED	- 0.0098 0.0020	0.0001 0.0098 0.0020	/	0.0001 0.0091 0.0021	/	0.0001 0.0085 0.0022
	Ms	/	199	/	777	/	1227
K=7	σ ESTIMATED	- -0.0002 0.0053	- -0.0009 0.0008	0.0444 -0.0010 0.0006	0.0023 -0.0010 0.0006	0.0065 -0.0010 0.0006	-0.0004 -0.0010 0.0006
	f ESTIMATED	- 0.2001 0.3000	- 0.2001 0.2998	0.1003 0.2000 0.3000	0.1001 0.2000 0.3000	0.0994 0.2000 0.3000	0.1000 0.2000 0.3000
	a ESTIMATED	- 0.0099 0.0021	- 0.0098 0.0020	0.0002 0.0091 0.0021	0.0001 0.0091 0.0021	/	0.0001 0.0086 0.0022
	Ms	/	92	281	280	/	393

As can be seen from the data, higher noise results in a worse estimate of damping and sometimes also of frequency, while amplitude does not.

In the vector of backward prediction coefficients B(z), the perturbations introduced by the noise can only be partially mitigated so, approximately, the higher the noise, the worse the estimate.

The TK method, like any other method using a truncated SVD, only works well when the signal-to-noise ratio is above a certain threshold, in fact, below this, some singular values of the noise become larger than those of the signal. Thus, the singular values of the noise intervene in the calculation of the b-vector, which leads to a significant degradation of performance. This phenomenon is called the threshold effect.

4.8.2 Kundur Test Network

The two-area Kundur [19] test network is made as reported in Figure 4.44.

Despite having a limited extension, this system is able to simulate in detail what really happens in a real interconnected electrical system.

The description of the control logic, incident on the parameters of voltage and frequency, is independent of the objective of this thesis, for it, in fact, refers to the scientific literature of reference [1].

The equivalent representation of the test network in the Simulink environment is reported in the Figure 4.70.

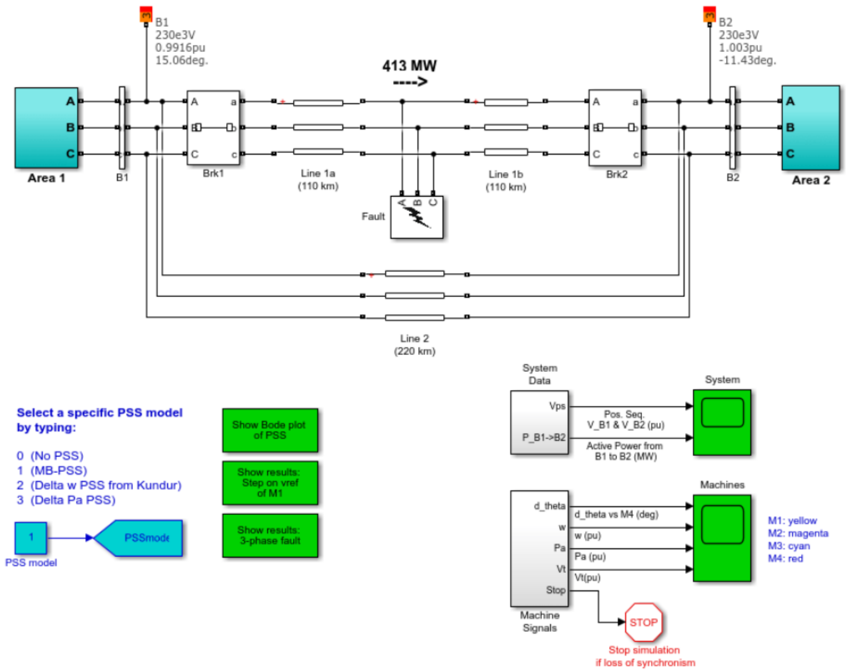

Figure 4-70 Simulink representation of the Kundur network

In the Figure 4.71 is shown a zoom of the single area.

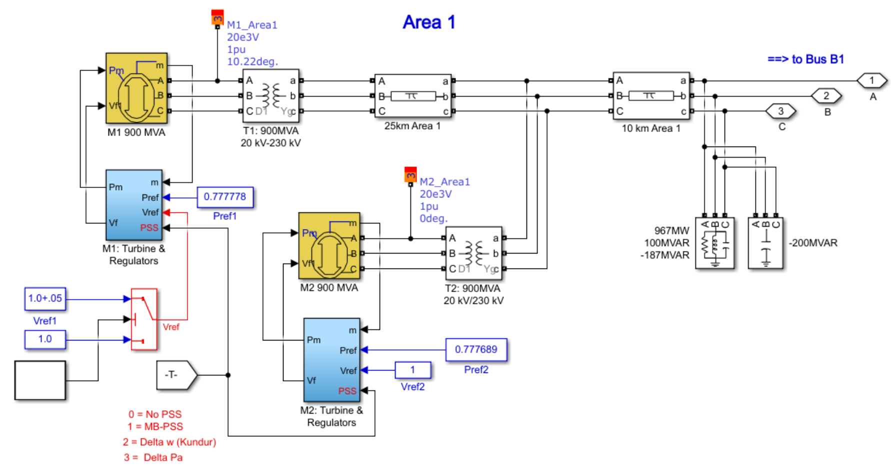

Figure 4-71 Zoom of the single area

Disabling the PSS in the simulation creates an inter-area oscillation between area 1 and area 2; it is measured by measuring the voltage on the bus leaving area 1. In Figure 4.72 are the trends in the power transmitted from area 1 to area 2 and the speed of the generators.

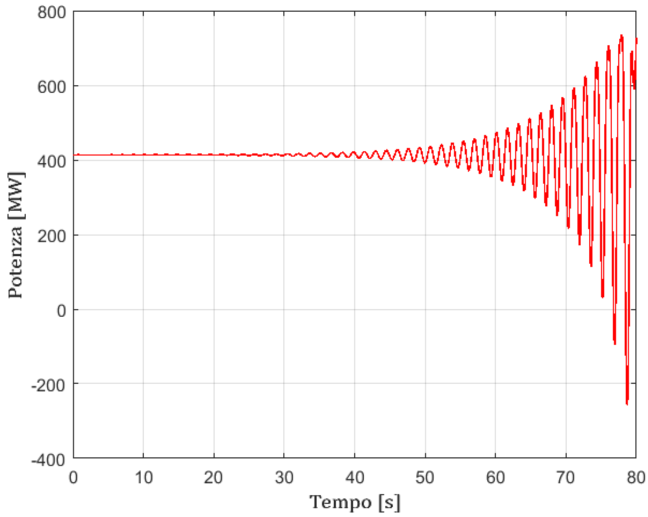

Figure 4-72 Trend of transmitted power

The temporal evolution of these quantities reveals the danger that inter-area oscillations have on the network (Figure 4.73).

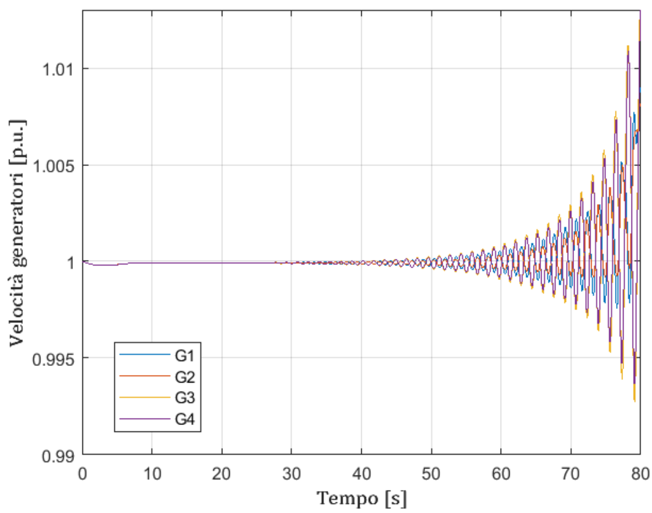

Figure 4-73 Trend of the time of the generators speed

From the measured voltage phasor, Figure 4.74, the phase for calculating the supply frequency is derived.

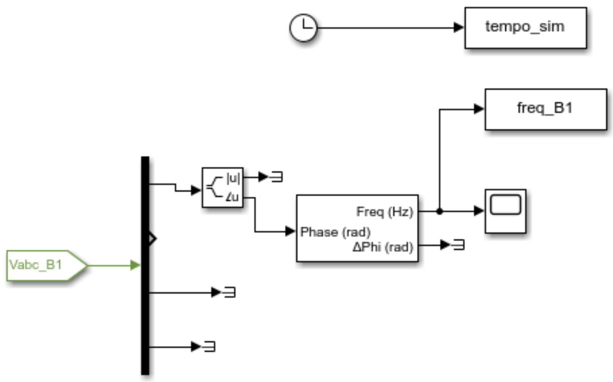

Figure 4-74 Simulink schema

Therefore, the trends of the voltage taken, and the frequency acquired are reported (Figure 4.75).

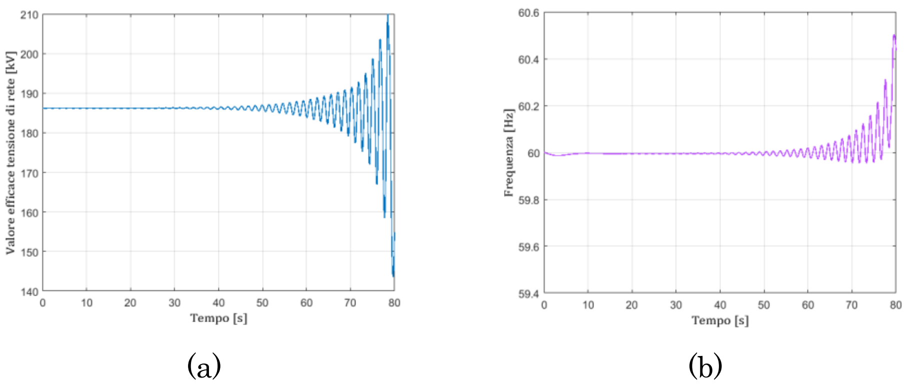

Figure 4-75 Trend over time of the effective value of the mains voltage (a) and (b) frequency

As can be seen from the Figure 4.75b, the frequency reaches high damping values towards the end of the 80 s window; therefore, the results of the algorithm will definitely show damping values related to the last 20 s varied and unreliable.
The used measurement procedure simulated the presence of a PMU capable of acquiring data with a sampling rate of 50 Hz. The time window analyzed has a duration of 80 s, and the sampled signal is

divided into four packets of 20 s each, in such a way as to use them as input to the TK aglorithm to estimate the parameters of the system's inter-area oscillation. The Kundur network [19], in fact, has an inter-area oscillation characterized by a frequency of **0.64 Hz** with a positive damping of σ = **0.13 1/s**. The results obtained by varying K and L are shown in the Table 4.15 (the window and thus N were fixed at the time the signal was divided into packets).

Table 4.15 Estimation of parameters on the Kundur network

Tw=20 SNR=80dB			σ ESTIMATED	f ESTIMATED	a ESTIMATED
K=1	*f1*	L=N/2	0.1029	0.6445	0.0002
		L=N/10	0.3726	0.6434	0.0008
	f2	L=N/2	0.1070	0.6402	0.0026
		L=N/10	0.1075	0.6407	0.0015
	f3	L=N/2	0.1055	0.6404	0.0279
		L=N/10	0.1051	0.6401	0.0114
	f4	L=N/2	0.1045	0.6402	0.2668
		L=N/10	0.0821	0.5983	0.0857
K=5	*f1*	L=N/2	0.1099	0.6436	0.0005
		L=N/10			
	f2	L=N/2	0.1056	0.6404	0.0016
		L=N/10			
	f3	L=N/2	0.1056	0.6402	0.0149
		L=N/10	0.1629	0.6362	0.0100
	f4	L=N/2	0.0700	0.6332	0.0992
		L=N/10	0.7448	0.6147	0.0605

Also onthe Kundur network it is possible to say that the TK method is particularly valid for estimating the frequency.

4.8.3 Experimental Test

The experimental test is carried out on two real signals acquired by the Italian WAMS system and supplied by Terna.

Before giving an input signal to the TK algorithm, it must be properly treated. Initially, taking into account the different PMUs with the relative data provided by these, in the presence of the Not A Number (NaN) and therefore of impossibility for the PMUs to detect the information, the system responds by counting the NaN and if these are in greater number than 30 the examined PMU is excluded, otherwise a moving average interpolation of the held data is carried out, obviously leaving out the NaN results from the aforementioned PMU from this operation. At a later time, a *Detrend* operation is carried out: the 50 Hz one is subtracted from the measured frequencies.

$$f_{measured} = f_{measured} - mean(f_{measured})$$

Finally, to the frequencies detected by the PMUs, a numerical filter is applied that allows to discriminate the frequency between 0.1 and 0.4 Hz.

The tests on the first signal were carried out by imposing K equal to 1, 5 and 7, varying the Tw window from 20 to 90 s and showing the difference with and without the application of a filtering action. Figure 4.76 shows the results obtained by setting K = 1.

In the graph at the window from 00:12 to 00:16, there is what is known as *mode mixing*: when there are two or more different modes of the same signal (to which as many close frequencies correspond) being composed in the time domain, it is difficult to distinguish the frequency components belonging to the different modes, resulting in alternating amplitudes in Figure 4.76.

This phenomenon is also present in the case of non-filtering signal that are reported in Figure 4.79 for a Tw equal to 40 s.

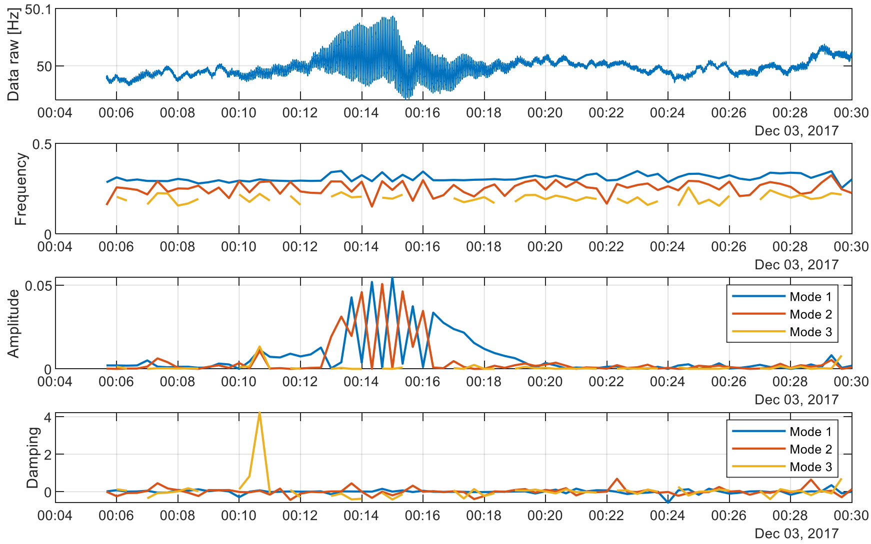

Figure 4-76 Simulation with: K = 1, Tw = 20 and filter

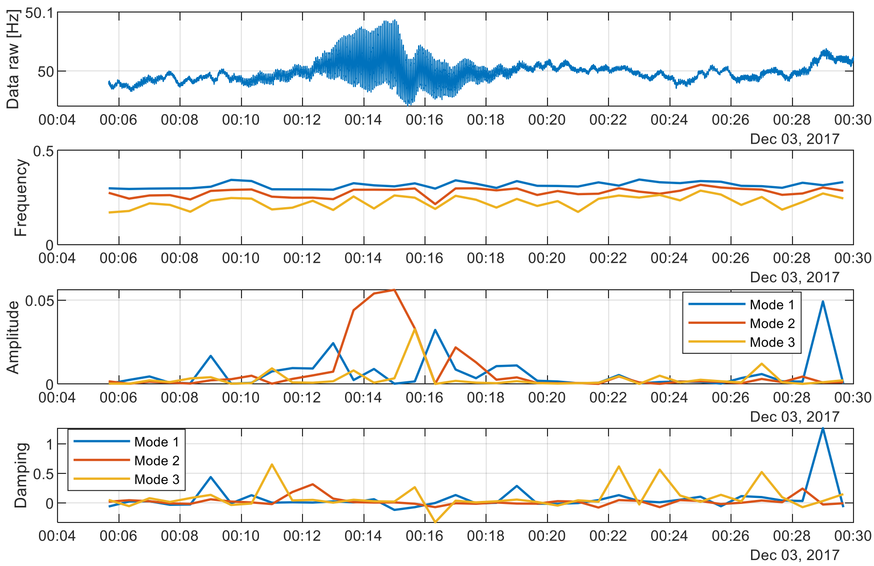

Figure 4-77 Simulation with: K = 1, Tw = 40 and filter

The results for K = 5 are shown in Figure 4.78.

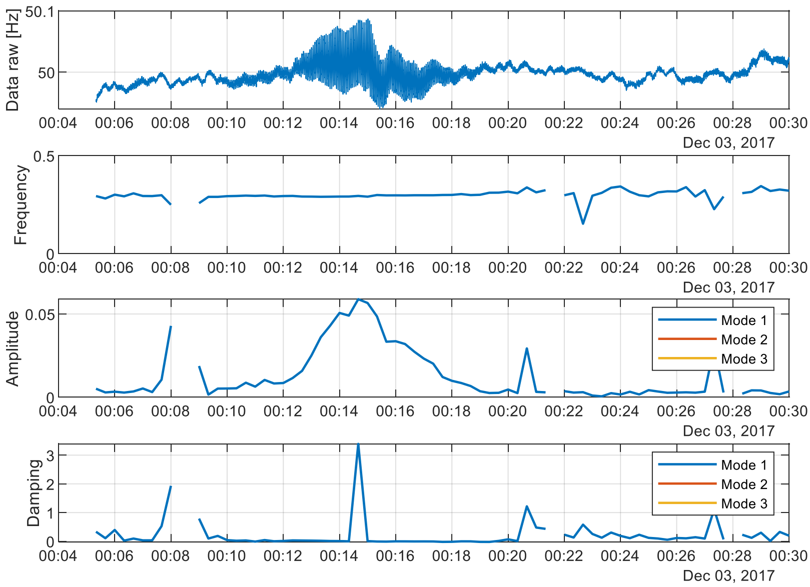

Figure 4-78 Simulation with Tw = 20, K = 5 and without filter.

As can be seen from the Figure 4.78 without the action of the filter and with K placed equal to 5, a mode is identified that has an amplitude profile very similar to the real signal.
To better understand the difference between the implementation of the filtered and unfiltered signal, the following tests are reported for a Tw = 40 s with the filtering action active and not (Figure 4.79).

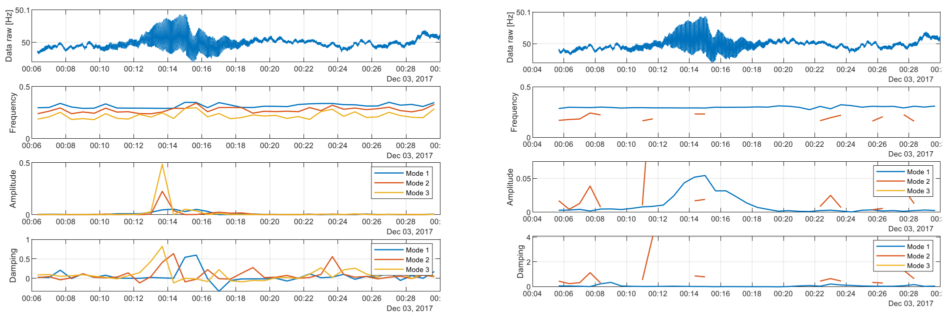

(a) (b)

Figure 4-79 Simulation with: Tw = 40, K = 5 and (a) filter (b) without filter

In the test in which the filter action is active (Figure 4.79a), more modes, and therefore more frequencies, are recorded than in the test in which this same action is absent (Figure 4.79b); this occurs because the filter response is not flat and enhances some frequencies. Since, from what we have learned, the filter could introduce dummy modes

and the algorithm turns out to be robust to noise, we prefer to show the results obtained without the filter action since they are considered satisfactory for the purposes of the paper.
To complete the tests performed with K = 5, in Figure 4.80 the results are shown for a Tw = 90 s and without filter.

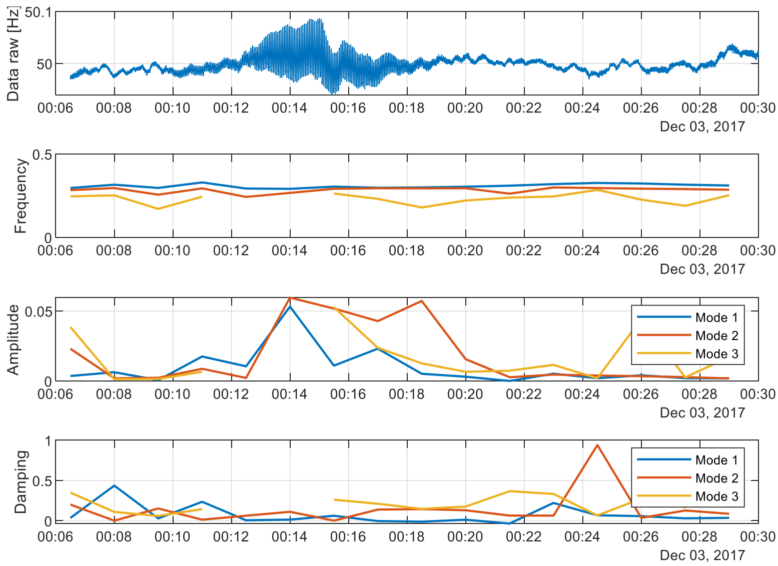

Figure 4-80 Simulation with Tw = 90, K = 5 and without filter

Having increased N and therefore the length of the window which is now equal to 90 s, in the Figure 4.76 there is the presence of more modes because, with K always equal to 5, it is cut in fact on a larger Henkel matrix, which is why the number of ways found is greater.
Finally, the tests developed for K = 7 are reported in the Figure 4.81. In particular, the test performed for a window of 20 s with the action of the filter active is shown because in this case the presence of a high value of K allows to cut the fictitious frequencies introduced by the filter and to reach a satisfactory result.

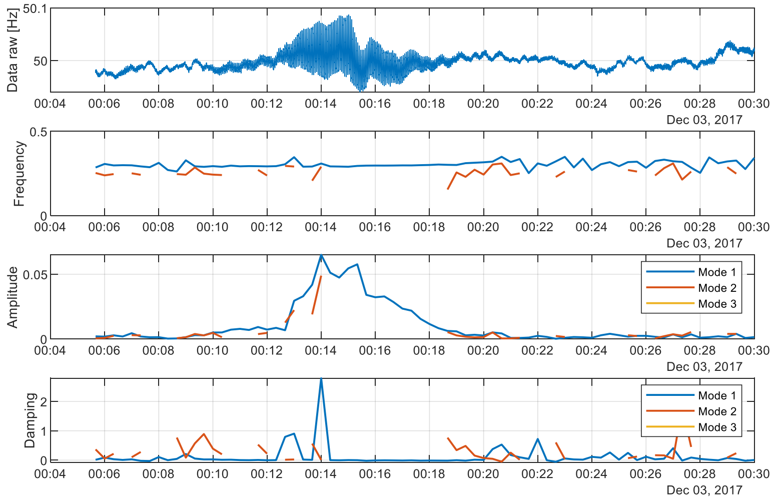

Figure 4-81 Simulation with Tw = 20, K = 7 and with filter

The tests are inserted without the action of the filter, for windows of 20 and 40 s (Figure 4.82).

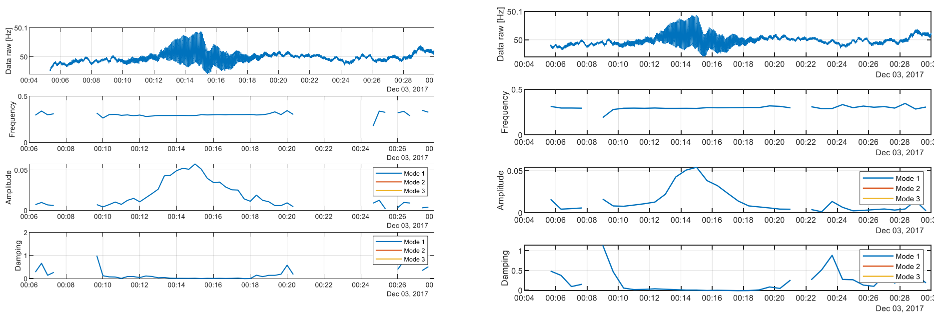

(a) (b)

Figure 4-82 Simulation with Tw = 20, K = 7 and (a) with filter (b) without filter

Finally, the same tests were carried out on the second signal, but only the tests at K = 5 (Figure 4.83). and 7 (Figure 4.84) for the Tw = 20 s are reported as they are the ones that have reported the most significant results.

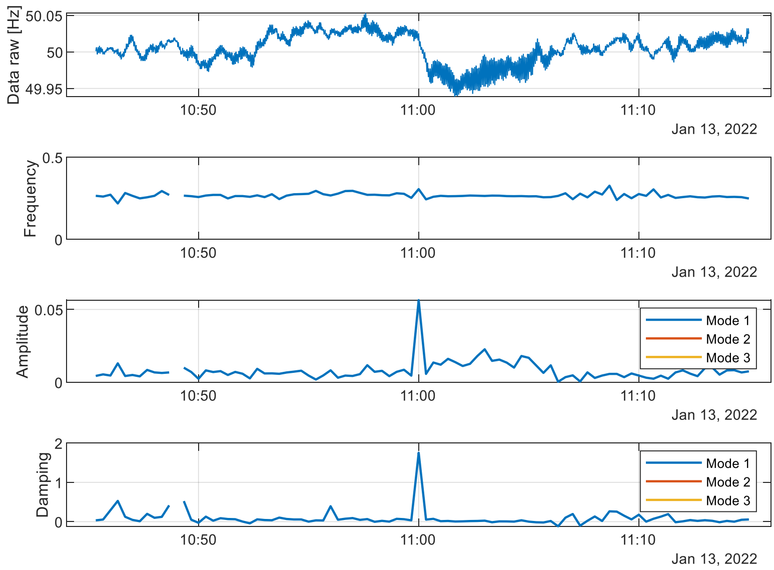

Figure 4-83 Simulation with Tw = 20, K = 5 and without filter

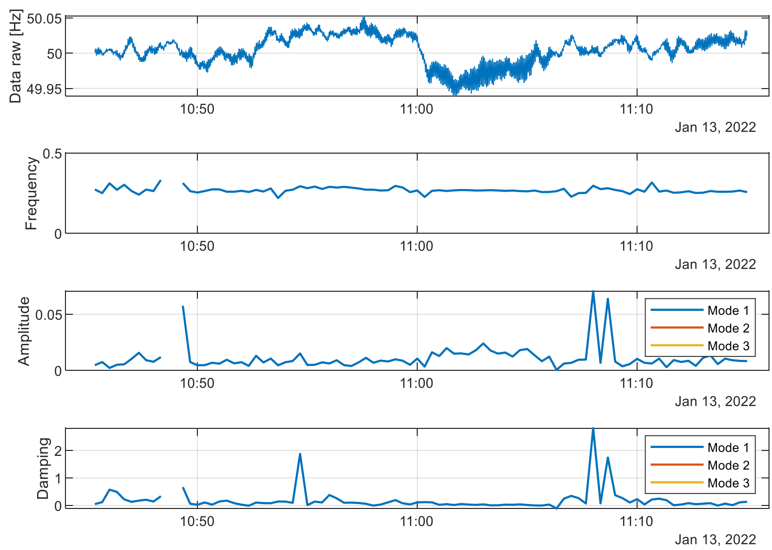

Figure 4-84 Simulation with Tw = 20, K = 7 and without filter

As can be seen in both Figures 4.83 and 4.84 from 11:00 onwards the amplitude trend would faithfully follow that of the signal if it were not for the presence of peaks due to either the lack of data from the PMU

or abrupt frequency variations; however, this figure does not appear to be worrying since the presence of these peaks will be mitigated when the signals from multiple PMUs are considered. The validity of this consideration is confirmed by the absence of the aforementioned peaks when the same signal is processed by the DMD algorithm, which, precisely, considers more PMU.
All the results obtained come from the study of national data of a single PMU, however, in the future, it is planned to use the TK method on data from multiple PMUs in order to improve the estimation of the parameters of our interest.

Chapter 5

5 Conclusions

This thesis addressed the problem of real-time estimation of inter-area oscillations in power systems through the use of enabling technologies such as WAMS and advanced estimation methodologies. The occurrence of inter-area oscillations in modern power systems is quite common, especially at the European level. Therefore, following the recommendations of ENTSOE, the work done attempts to provide valuable support to the TSO in improving the monitoring of these phenomena by counteracting critical conditions while enhancing the possibility of very fast reactions. Such support consisted of defining an estimation algorithm that would be (i) highly accurate to increase the TSO's situational awareness of critical and non-critical inter-area oscillation phenomena, (ii) characterized by a low computational load and flexible enough to be implemented in the TSO's simulation platforms interfaced with WAMS, and (iii) highly robust against all potential situations encountered in routine operation. In the early stages of the research activity, we focused on the most widely used algorithms in the accredited scientific literature, coding them, implementing them in the simulation in the Italian TSO environment interfaced with WAMS, and proposing enhancement from the basic solution that would overcome some of the encountered limitations. In fact, the results obtained with real data made it possible to identify the strengths to be preserved and the downsides to be overcome. Single-channel algorithms (i.e., Huang Hilbert, Tuft Kumaresan), heuristic algorithms (Particle Swarm Optimization) and multi-channel algorithms (Dynamic Mode Decomposition) were studied, implemented and tested to the purpose.

The results showed that among the single-channel algorithms the one that is most accurate, even when the spectral components to be characterized are very close to each other in the frequency domain, is the Tukt Kumaresan (TK). In fact, the latter applied over long-period windows succeeds in describing the characteristics of the modes of

interest with good accuracy. The disadvantage of this type of solution is definitely being single channel and therefore not being able to give a system view to the room operator. For this reason, on this algorithm we will proceed with a multi-channel-like development so as to aggregate, downstream of the estimation of the individual TKs, the different characteristics by clustering the modes and allowing the hall operator to have under control and continuouslt monitori the state of the whole electrical system.
The heuristic algorithm, Particle Swarm Optimitazion (PSO), even proposing an advanced version for overcoming some of the limitations it had in the basic version, continues to have an relevant limitation for this application, namely, the estimation error of signal characteristics increases with the number of unknowns (Amplitude, frequency, damping, phase) and the reduction of spectral resolution. For this reason, this type of algorithm has not been implemented on the TSO environments.
The multi-channel algorithm, Dynamic Mode Decomposition (DMD), was implemented by proposing the dynamic order variant. The results obtained from the tests carried out both on simulated and actual data showed greater accuracy and the elimination of one of the main problems present in the basic version from the algorithm, namely mode mixing. In addition, the proposed solution has, especially during transients, the great advantage of focusing only on the excited mode. This provides greater accuracy for both monitoring and automatic oscillation contrast applications. Given the obtained results, this type of algorithm has been implemented on the TSO platform and still used by the real time room operator in continuous monitoring of the state of the whole Italian power system.
In addition, all algorithms considered in this work were tested against some critical effects of wide-area communication networks, i.e., noise and data packet drop. The response of the developed algorithm, thanks to the characteristics of Mode Decomposition and the proposed damping calculation method, is also successful in these situations.
A general activation criterion of Warning and Alarm has also been defined to ensure that the excitation of the inter-area oscillation is immediately intercepted by the operator to apply counteracting actions such as redispatching the generators, adjusting the link line flows, reducing the load and changing the network topology.

Bibliography

[1] ARERA. (2019). Type of electricity networks (networks with the obligation to connect third parties and Closed Distribution Systems) (in Italian), available at https://www.arera.it/allegati/docs/13/578-13all_ti.pdf. (Last accessed: 18.10.2022).

[2] ENTSO-E. (2020). TYNDP 2020 Projects Sheets, available at https://tyndp2020-project-platform.azurewebsites.net/projectsheets/transmission. (Last accessed: 18.10.2022).

[3] ENTSO-E. (2020). 339 - Italian HVDC tri-terminal link.

[4] European Commission (2015). The interconnection of energy markets ensures security of supply, market integration and the large-scale use of renewable energy, available at https://energy.ec.europa.eu/system/files/2015-07/1_EN_ACT_part1_v11_0.pdf (Last accessed: 18.10.2022).

[5] ENTSO-E. (2019). 29 - Italy-Tunisia, available at https://tyndp.entsoe.eu/tyndp2018/projects/projects/29 (Last accessed: 18.10.2022).

[6] TERNA (2021) Development plan, available at https://www.terna.it/en/media/press-releases/detail/2021-development-plan-national-electricity-grid-presented (Last accessed: 18.10.2022).

[7] Terna. IN THE ENERGY TRANSITION, available at https://www.terna.it/en/about-us/inside-energy-transition (Last accessed 18.10.2022).

[8] Rogers, Graham. Power system oscillations. Springer Science & Business Media, 2012.

[9] Messina, Arturo Roman, ed. Inter-area oscillations in power systems: a nonlinear and nonstationary perspective. Springer Science & Business Media, 2009.

[10] Kundur, Prabha S., and Om P. Malik. Power system stability and control. McGraw-Hill Education, 2022.

[11] Michi, Luigi, et al. "Improving dynamic stability in presence of static generation: Issues and potential countermeasures." 2019 AEIT International Annual Conference (AEIT). IEEE, 2019.

[12] ENTSO-E. Analysis Of Ce Inter-Area Oscillations Of 1st December 2016, available https://eepublicdownloads.entsoe.eu/clean-documents/SOC%20documents/Regional_Groups_Continental_Europe/2017/CE_inter-area_oscillations_Dec_1st_2016_PUBLIC_V7.pdf (Last accessed 18.10.2022).

[13] ENTSO-E. (2018). Oscillation Event 03.12.2017 available https://eepublicdownloads.entsoe.eu/clean-documents/SOC%20documents/Regional_Groups_Continental_Europe/OSCILLATION_REPORT_SPD.pdf (Last accessed 18.10.2022).
[14] Zhang, S., Xie, X., & Wu, J. (2008). WAMS-based detection and early-warning of low-frequency oscillations in large-scale power systems. Electric Power Systems Research, 78(5), 897-906.
[15] Giannuzzi, G., Lauria, D., Pisani, C., & Villacci, D. (2015). Real-time tracking of electromechanical oscillations in ENTSO-e Continental European Synchronous Area. International Journal of Electrical Power & Energy Systems, 64, 1147-1158.
[16] Ma, J., Han, D. O. N. G., Sheng, W. J., He, R. M., Yue, C. Y., & Zhang, J. (2008). Wide area measurements-based model validation and its application. IET generation, transmission & distribution, 2(6), 906-916.
[17] Phadke, A. G., & Bi, T. (2018). Phasor measurement units, WAMS, and their applications in protection and control of power systems. Journal of Modern Power Systems and Clean Energy, 6(4), 619-629.
[18] Cirio, D., Lucarella, D., Giannuzzi, G., & Tuosto, F. (2011). Wide area monitoring in the Italian power system: architecture, functions and experiences. European Transactions on Electrical Power, 21(4), 1541-1556.
[19] "IEEE/IEC International Standard - Measuring relays and protection equipment - Part 118-1: Synchrophasor for power systems - Measurements," in IEC/IEEE 60255-118-1:2018 , vol., no., pp.1-78, 19 Dec. 2018
[20] "IEEE Standard for Synchrophasor Data Transfer for Power Systems," in IEEE Std C37.118.2-2018 (Revision of IEEE Std C37.118-2011) , vol., no., pp.1-53, 2011
[21] Barbosh, M., Singh, P., & Sadhu, A. (2020). Empirical mode decomposition and its variants: A review with applications in structural health monitoring. Smart Materials and Structures, 29(9), 093001.
[22] Bedrosian, E. A product theorem for Hilbert transforms 1962.
[23] Lauria, D.; Pisani, C. On Hilbert transform methods for low frequency oscillations detection. IET Generation, 424 Transmission & Distribution 2014, 8, 1061–1074.
[24] H. Li, L. Li, T. Qian, ―Discrete-time analytic signals and Bedrosian product theorems, Digital Signal Processing, vol. 20, no. 4, pp. 982–990, July 2010.
[25] Baccigalupi, A.; Liccardo, A. The Huang Hilbert Transform for evaluating the instantaneous frequency 411 evolution of transient signals in non-linear systems. Measurement 2016, 86, 1–13.
[26] Peng, J. H., & Kirtley, J. L. (2014, February). An improved empirical mode decomposition method for monitoring electromechanical oscillations. In ISGT 2014 (pp. 1-5).
[27] Boche, H.; Protzmann, M. A new algorithm for the reconstruction of bandlimited functions and their Hilbert transform. IEEE transactions on instrumentation and measurement 1997, 46, 442–444.
[28] Bonavolontà, F., Di Noia, L. P., Lauria, D., Liccardo, A., & Tessitore, S. (2019). An optimized HT-based method for the analysis of inter-area oscillations on electrical systems. Energies, 12(15), 2935.

[29] Lauria, D., Pisani, C. (2015). Improved non-linear least squares method for estimating the damping levels of electromechanical oscillations. IET Generation, Transmission & Distribution, 9(1), 1-11.
[30] Grewal, M. S., & Andrews, A. P. (2014). Kalman filtering: Theory and Practice with MATLAB. John Wiley & Sons.
[31] Peng, J. C. H., & Nair, N. K. C. (2011). Enhancing Kalman filter for tracking ringdown electromechanical oscillations. IEEE Transactions on Power Systems, 27(2), 1042-1050.
[32] Yazdanian, M., Mehrizi-Sani, A., & Mojiri, M. (2015). Estimation of electromechanical oscillation parameters using an extended Kalman filter. IEEE Transactions on Power Systems, 30(6), 2994-3002.
[33] Yu, Z., Shi, D., Wang, Z., Zhang, Q., Huang, J., & Pan, S. (2019). Distributed estimation of oscillations in power systems: An extended Kalman filtering approach. CSEE Journal of Power and Energy Systems, 5(2), 181-189.
[34] Wan, E. A., & Van Der Merwe, R. (2001). The unscented Kalman filter. Kalman filtering and neural networks, 221-280.
[35] Reddy, J. B. V., Dash, P. K., Samantaray, R., & Moharana, A. K. (2009). Fast tracking of power quality disturbance signals using an optimized unscented filter. IEEE Transactions on Instrumentation and Measurement, 58(12), 3943-3952.
[36] Mezura-Montes, E., & Coello, C. A. C. (2011). Constraint-handling in nature-inspired numerical optimization: past, present and future. Swarm and Evolutionary Computation, 1(4), 173-194.
[37] Eberhart R, and Kennedy J., "Particle swarm optimization," in Proceedings of the IEEE international conference on neural networks, vol. 4, 1995, pp. 1942–1948.
[38] Bonavolontà, F., Di Noia, L. P., Liccardo, A., Tessitore, S., & Lauria, D. (2020). A PSO-MMA method for the parameters estimation of interarea oscillations in electrical grids. IEEE Transactions on Instrumentation and Measurement, 69(11), 8853-8865.
[39] N. V. George and G. Panda, "A particle-swarm-optimization-based decentralized nonlinear active noise control system," IEEE Transactions on Instrumentation and Measurement, vol. 61, no. 12, pp. 3378–3386, 2012.
[40] Das, T. K., & Venayagamoorthy, G. K. (2006, June). Optimal design of power system stabilizers using a small population based PSO. In 2006 IEEE Power Engineering Society General Meeting (pp. 7-pp). IEEE.
[41] Pehlivanoglu, Y. V. (2012). A new particle swarm optimization method enhanced with a periodic mutation strategy and neural networks. IEEE Transactions on Evolutionary Computation, 17(3), 436-452.
[42] Nikabadi, A., & Ebadzadeh, M. (2008). Particle swarm optimization algorithms with adaptive Inertia Weight: A survey of the state of the art and a Novel method. IEEE journal of evolutionary computation.
[43] J. Nathan Kutz, U. o. (2016). Dynamic Mode Decomposition: data-driven modeling of complex systems.
[44] Schmid, P. J. (2010). Dynamic mode decomposition of numerical and experimental data. Journal of fluid mechanics, 656, 5-28.
[45] Berizzi, A., Bosisio, A., Simone, R., Vicario, A., Giannuzzi, G., Pisani, C.,

& Zaottini, R. (2020). Real-time identification of electromechanical oscillations through dynamic mode decomposition. IET Generation, Transmission & Distribution, 14(19), 3992-3999.
[46] J. Nathan Kutz, Brunton S. L. (2019). DATA DRIVEN SCIENCE & ENGINEERING.
[47] Liccardo, A., Bonavolontà, F., Pisani, C., Giannuzzi, G., Tessitore, S., & Cristiano, S. (2022, June). DMD Dynamic Order Algorithm for the Estimation of Inter-area Oscillations. In 2022 International Symposium on Power Electronics, Electrical Drives, Automation and Motion (SPEEDAM) (pp. 412-417). IEEE.
[48] Liccardo, A., Tessitore, S., Bonavolontà, F., Cristiano, S., Di Noia, L. P., Giannuzzi, G. M., & Pisani, C. (2022). Detection and Analysis of Inter-Area Oscillations Through a Dynamic-Order DMD Approach. IEEE Transactions on Instrumentation and Measurement, 71, 1-14.
[49] Tufts, D. W., & Kumaresan, R. (1982). Estimation of frequencies of multiple sinusoids: Making linear prediction perform like maximum likelihood. Proceedings of the IEEE, 70(9), 975-989.
[50] Kumaresan, R., & Tufts, D. (1982). Estimating the parameters of exponentially damped sinusoids and pole-zero modeling in noise. IEEE transactions on acoustics, speech, and signal processing, 30(6), 833-840.
[51] Rai, S., Lalani, D., Nayak, S. K., Jacob, T., & Tripathy, P. (2016). Estimation of low-frequency modes in power system using robust modified Prony. IET Generation, Transmission & Distribution, 10(6), 1401-1409.
[52] Xiao, J., Xie, X., Han, Y., & Wu, J. (2004). Dynamic tracking of low-frequency oscillations with improved Prony method in wide-area measurement system. In IEEE Power Engineering Society General Meeting, 2004. (pp. 1104-1109).
[53] Zhao, S., & Loparo, K. A. (2019). Forward and backward extended Prony method for complex exponential signals with/without additive noise. Digital Signal Processing, 86, 42-54.

Author's Publications

International journal papers

- Liccardo, A., Tessitore, S., Bonavolonta, F., Cristiano, S., Di Noia, L.P., Giannuzzi, G.M., Pisani, C., "Detection and Analysis of Inter-Area Oscillations Through a Dynamic-Order DMD Approach" (2022), *IEEE Transactions on Instrumentation and Measurement, 71, art. no. 9004914.* DOI: 10.1109/TIM.2022.3186371
- Bonavolontà, F., Di Noia, L.P., Liccardo, A., Tessitore, S., Lauria, D., "A PSO-MMA Method for the Parameters Estimation of Interarea Oscillations in Electrical Grids" (2020), *IEEE Transactions on Instrumentation and Measurement, 69 (11), art. no. 9107075, pp. 8853-8865.* DOI: 10.1109/TIM.2020.2998909
- Bonavolontà, F., Di Noia, L.P., Lauria, D., Liccardo, A., Tessitore, S., "An optimized HT-based method for the analysis of inter-area oscillations on electrical systems" (2019), *Energies, 12 (15), art. no. 2935.* DOI: 10.3390/en12152935

International conference papers

- Liccardo, A., Bonavolonta, F., Pisani, C., Giannuzzi, G., Tessitore, S., Cristiano, S., "DMD Dynamic Order Algorithm for the Estimation of Inter-area Oscillations" (2022), *2022 International Symposium on Power Electronics, Electrical Drives, Automation and Motion, SPEEDAM 2022, pp. 412-417.* DOI: 10.1109/SPEEDAM53979.2022.9842132
- Giannuzzi, G.M., Lauria, D., Pisani, C., Tessitore, S., "An optimization procedure for power system stabilizer tuning" (2022), *2022 International Symposium on Power Electronics, Electrical Drives, Automation and Motion, SPEEDAM 2022, pp. 112-117.* DOI: 10.1109/SPEEDAM53979.2022.9842034
- Liccardo, A., Tessitore, S., Pisani, C., Bonavolonta, F., Cacciapuoti, S., Giannuzzi, G.M., "A WAMS emulation framework for the characterization of measurement algorithms on electrical transmission networks" (2021), *2021 IEEE International Workshop on Metrology for Industry 4.0 and IoT, MetroInd 4.0 and IoT 2021 - Proceedings, art. no. 9488461, pp. 572-577.* DOI: 10.1109/MetroInd4.0IoT51437.2021.9488461
- Carlini, E.M., Giannuzzi, G.M., Zaottini, R., Pisani, C., Tessitore, S., Liccardo, A., Angrisani, L., "Parameter Identification of Interarea Oscillations in Electrical Power Systems via an Improved Hilbert Transform Method" (2020), *UPEC 2020 - 2020 55th International*

Universities Power Engineering Conference, Proceedings, art. no. 9209805. DOI: 10.1109/UPEC49904.2020.9209805

- Angrisani, L., Bonavolonta, F., Di Noia, L.P., Lauria, D., Liccardo, A., Tessitore, S., Ruggiero, D., A novel PSO-CWA algorithm for the estimation of inter-area oscillation parameters" (2020) *I2MTC 2020 - International Instrumentation and Measurement Technology Conference, Proceedings, art. no. 9128935.* DOI: 10.1109/I2MTC43012.2020.9128935

National conference papers

- Liccardo, A., Bonavolonta, F., Pisani, C., Giannuzzi, G., Tessitore, S., "Analisi delle oscillazioni inter-area tramite DMD a ordine dinamico" (2022), Atti del VI Forum Nazionale delle Misure.
- Bonavolonta, F., Di Noia, L.P., Lauria, D., Liccardo, A., Tessitore, S., "Un metodo PSO-MMA per la stima dei parametri delle oscillazioni inter-area nelle reti di trasmissione dell'energia elettrica (2020), Atti del IV Forum Nazionale delle Misure.